

Evidence for shock heating and constraints on Martian surface temperatures revealed by $^{40}\text{Ar}/^{39}\text{Ar}$ thermochronometry of Martian meteorites

William S. Cassata^{a,b,*}, David L. Shuster^a, Paul R. Renne^{a,b}, Benjamin P. Weiss^c

^a Berkeley Geochronology Center, 2455 Ridge Road, Berkeley, CA 94709, USA

^b Department of Earth and Planetary Science, University of California-Berkeley, 307 McCone Hall #4767, Berkeley, CA 94720-4767, USA

^c Department of Earth, Atmospheric, and Planetary Sciences, Massachusetts Institute of Technology, 77 Massachusetts Avenue, Cambridge, MA 02139, USA

Received 29 March 2010; accepted in revised form 17 August 2010; available online 27 August 2010

Abstract

The thermal histories of Martian meteorite are important for the interpretation of petrologic, geochemical, geochronological, and paleomagnetic constraints that they provide on the evolution of Mars. In this paper, we quantify $^{40}\text{Ar}/^{39}\text{Ar}$ ages and Ar diffusion kinetics of Martian meteorites Allan Hills (ALH) 84001, Nakhla, and Miller Range (MIL) 03346. We constrain the thermal history of each meteorite and discuss the resulting implications for their petrology, paleomagnetism, and geochronology. Maskelynite in ALH 84001 yields a $^{40}\text{Ar}/^{39}\text{Ar}$ isochron age of 4163 ± 35 Ma, which is indistinguishable from recent Pb–Pb (Bouvier et al., 2009a) and Lu–Hf ages (Lapen et al., 2010). The high precision of this result arises from clear resolution of a reproducible trapped $^{40}\text{Ar}/^{36}\text{Ar}$ component in maskelynite in ALH 84001 ($^{40}\text{Ar}/^{36}\text{Ar} = 632 \pm 90$). The maskelynite $^{40}\text{Ar}/^{39}\text{Ar}$ age predates the Late Heavy Bombardment and likely represents the time at which the original natural remanent magnetization (NRM) component observed in ALH 84001 was acquired. Nakhla and MIL 03346 yield $^{40}\text{Ar}/^{39}\text{Ar}$ isochron ages of 1332 ± 24 and 1339 ± 8 Ma, respectively, which we interpret to date crystallization. Multi-phase, multi-domain diffusion models constrained by the observed Ar diffusion kinetics and $^{40}\text{Ar}/^{39}\text{Ar}$ age spectra suggest that localized regions within both ALH 84001 and Nakhla were intensely heated for brief durations during shock events at 1158 ± 110 and 913 ± 9 Ma, respectively. These ages may date the marginal melting of pyroxene in each rock, mobilization of carbonates and maskelynite in ALH 84001, and NRM overprints observed in ALH 84001. The inferred peak temperatures of the shock heating events (>1400 °C) are sufficient to mobilize Ar, Sr, and Pb in constituent minerals, which may explain some of the dispersion observed in $^{40}\text{Ar}/^{39}\text{Ar}$, Rb–Sr, and U–Th–Pb data toward ages younger than ~ 4.1 Ga. The data also place conservative upper bounds on the long-duration residence temperatures of the ALH 84001 and Nakhla protolith to be $22^{+8}_{-\infty}$ °C and $81^{+9}_{-\infty}$ °C over the last ~ 4.16 Ga and ~ 1.35 Ga, respectively. MIL 03346 has apparently not experienced significant shock-heating since it crystallized, consistent with the fact that various chronometers yield concordant ages.

© 2010 Elsevier Ltd. All rights reserved.

1. INTRODUCTION

Martian meteorites have provided a diversity of petrologic, geochemical, geochronological, and geomagnetic constraints on the evolution of Mars. However, some of our understanding and interpretations of these findings depend on the inferred thermal and shock histories of each meteorite. Specifically, the physical significance of

* Corresponding author at: Department of Earth and Planetary Science, University of California-Berkeley, 307 McCone Hall #4767, Berkeley, CA 94720-4767, USA Tel. +1 773 802 8146.

E-mail addresses: cassata@berkeley.edu (W.S. Cassata), dshuster@bgc.org (D.L. Shuster), prrenne@bgc.org (P.R. Renne), bpweiss@mit.edu (B.P. Weiss).

radioisotopic ages, timing of natural remanent magnetization (NRM) acquisition, and conditions for secondary mineral deposition are sensitive to the thermal histories of each meteorite and its protolith during residence near the Martian surface and subsequent transport to Earth.

Several studies have reported $^{40}\text{Ar}/^{39}\text{Ar}$ age determinations for Allan Hills (ALH) 84001, the results of which are dependant upon corrections for trapped, terrestrial, cosmogenic, and reactor-produced Ar isotopes. The range in observed $^{40}\text{Ar}/^{39}\text{Ar}$ ages (~ 3.8 – 4.2 Ga; Table S1) is well beyond analytical uncertainties, which likely reflects real age variations as well as different correction procedures (Ash et al., 1996; Knott et al., 1996; Ilg et al., 1997; Turner et al., 1997; Bogard and Garrison, 1999). Small discrepancies also arise from inconsistent values of decay constants used in the various studies, but these are small compared to the apparent age variations. Sm–Nd and Rb–Sr ages initially converged upon an apparent igneous crystallization age of 4.50–4.56 Ga (Jagoutz et al., 1994; Nyquist et al., 1995; Nyquist et al., 2001), although Wadhwa and Lugmair (1996) reported a bulk rock and pyroxene Rb–Sr isochron age of 3.84 ± 0.05 Ga¹. More recent Pb-based geochronometry strongly indicates that the crystallization age of ALH 84001 is ~ 4.1 Ga (Bouvier et al., 2009a; Jagoutz et al., 2009), similar to U–Pb and Th–Pb ages for apatite of 4.02 ± 0.01 and 3.97 ± 0.43 Ga, respectively, which were originally interpreted as impact-reset ages (Terada et al., 2003). Lapen et al. (2010) report new Sm–Nd and Lu–Hf ages of 4.41 ± 0.03 and 4.09 ± 0.03 Ga, respectively. The older (and presumably erroneous) Sm–Nd age has been attributed to isochron “rotation” by altered (younger) phosphate minerals or open system behavior (Lapen et al., 2010). This hypothesis appears to be corroborated by more recent phosphate Th–Pb ages, which are younger than the age of crystallization (2.93 ± 0.41 Ga; Jagoutz et al., 2009). Rb–Sr and U–Th–Pb ages for carbonates range from 1.4 to 4.05 Ga (Wadhwa and Lugmair, 1996; Borg et al., 1999), although the 1.4 Ga age has been challenged on geochemical grounds (Borg et al., 1999). U–Th–He ages on phosphates generally range from 0.1 to 1.5 Ga (Min and Reiners, 2007). In summary, although the crystallization age appears to be ~ 4.1 Ga, considerable uncertainty exists regarding the age of carbonate formation and the timing of shock events.

Several studies have also reported $^{40}\text{Ar}/^{39}\text{Ar}$ age determinations for Nakhla (Table S1). The results have generally converged upon an age of 1.3–1.4 Ga (Podosek, 1973; Bogard and Husain, 1977; Swindle and Olson, 2004; Park et al., 2009). Rb–Sr, Sm–Nd, and U–Pb studies yield younger or equivalent ages, ranging from 1.24 to 1.36 Ga (Table S1; Gale et al., 1975; Papanastassiou and Wasserburg, 1974; Nakamura et al., 1982; Bouvier et al., 2007). Ganapathy and Anders (1969) determined a U–Th–He age of ~ 0.77 Ga. Again, these age variations are greater than analytical uncertainties, although they are considerably smaller than those observed in ALH 84001. Unlike Nakhla, the $^{40}\text{Ar}/^{39}\text{Ar}$, Sm–Nd, Rb–Sr, Lu–Hf, and Pb–Pb

chronometers all yield indistinguishable ages of ~ 1.3 – 1.4 Ga for Miller Range (MIL) 03346 (Table S1; Shih et al., 2006; Bouvier et al., 2009b; Park et al., 2009).

Observed $^{40}\text{Ar}/^{39}\text{Ar}$ age spectra of extraterrestrial samples commonly show incomplete radiogenic ^{40}Ar (hereafter $^{40}\text{Ar}^*$) retention manifested as partially reset (i.e., sub-plateau) $^{40}\text{Ar}/^{39}\text{Ar}$ ages in initial heating steps. These features have commonly been attributed to $^{40}\text{Ar}^*$ loss due to elevated surface temperatures (e.g., Turner, 1971; Weiss et al., 2002b; Shuster and Weiss, 2005) and impact events (e.g., Turner et al., 1966; Bogard, 1995; Shuster et al., 2010). Accurately quantified diffusion kinetics are necessary to relate laboratory observations of late-stage $^{40}\text{Ar}^*$ loss to geological thermal histories. To better understand the thermal histories of ALH 84001, Nakhla, and MIL 03346 and to reconcile some of the observed age variations, we have undertaken detailed $^{40}\text{Ar}/^{39}\text{Ar}$ studies of these meteorites. In this work, we quantify Ar diffusion kinetics of each sample and examine the permissible physical conditions that could have resulted in the apparent $^{40}\text{Ar}^*$ distributions. Because appreciable quantities of $^{40}\text{Ar}^*$ exist in glasses, plagioclase, and pyroxene, and because the kinetics of Ar diffusion in these phases are distinct, $^{40}\text{Ar}/^{39}\text{Ar}$ thermochronometry of whole-rock meteorites can constrain a range of time-temperature (t – T) conditions for each sample. Using the apparent diffusion parameters and age spectra, we investigate the shock and thermal histories of ALH 84001, Nakhla, and MIL 03346.

2. SAMPLES

2.1. ALH 84001

ALH 84001 is a coarse-grained, cataclastic orthopyroxene that is composed of 97% orthopyroxene (OPX; average composition $\text{En}_{70}\text{Fs}_{27}\text{Wo}_3$), 2% chromite, <1% maskelynite (typically $\text{An}_{34}\text{Ab}_{62}\text{Or}_4$), 0.15% phosphates (merrillite and apatite), and trace quantities of clinopyroxene (CPX), carbonate, pyrite, and olivine (Mason et al., 1992; Mittlefehldt, 1994, 1997; Greenwood and McSween, 2001). Maskelynite is the primary potassium (K)-bearing phase, with lesser quantities of K in OPX. ALH 84001 has been subjected to several shock events throughout its history (Treiman, 1995, 1998, 2003). It contains mm-wide bands of crushed orthopyroxene with 10–30 μm OPX grain fragments (Treiman, 1995), as well as highly-localized OPX glass (Bell et al., 1999; Barber and Scott, 2006). Plagioclase has been completely converted to maskelynite and carbonate spheroids have been fractured and microfaulted by at least one shock event (Treiman, 1998).

2.2. Nakhla

Nakhla is a coarse-grained clinopyroxenite that comprises $\sim 80\%$ CPX ($\text{Wo}_{40}\text{En}_{40}\text{Fs}_{20}$), $\sim 10\%$ olivine, $\sim 10\%$ mesostasis with plagioclase ($\text{An}_{34}\text{Ab}_{62}\text{Or}_4$), and trace quantities of OPX, Fe–Ti oxides, alteration phases, and other minerals (Bunch and Reid, 1975; Friedman-Lentz et al., 1999). Mesostasis feldspars are the primary K-bearing phases, with lower K concentrations in olivine and CPX.

¹ All ages and other quantities throughout this paper are reported at 1 σ uncertainty.

Nakhla has been shocked at least once, as evidenced by reduced refractive indices for plagioclase, planar fractures in CPX and olivine and localized brecciation (Fritz et al., 2005), as well as localized pyroxene impact melts (Lambert, 1987; Malavergne et al., 2001).

2.3. MIL 03346

MIL 03346 is a coarse-grained clinopyroxenite that comprises 79% CPX (zoned, core composition is $\text{Wo}_{41}\text{En}_{38}\text{Fs}_{21}$), ~1–2% olivine, ~20% mesostasis containing feldspar-composition intercumulus glass ($\text{Ab}_{71-62}\text{Or}_{7-14}$), and trace quantities of OPX, Fe–Ti oxides, alteration phases, and other minerals (Stopar et al., 2005; Anand et al., 2005; Day et al., 2006). Feldspar-composition intercumulus glass is the primary K-bearing phase, with lesser concentrations of K in olivine and CPX (Sautter et al., 2006). Although MIL 03346 appears less altered by shock effects than most other Martian meteorites (Murty et al., 2005), extensive fractures and shock induced twinning are evident in some pyroxenes (Anand et al., 2005).

3. METHODS

3.1. Analytical Details

Whole-rock fragments were loaded into aluminum discs alongside Hb3gr neutron fluence monitors (Jourdan and Renne, 2007). The samples and fluence monitors were co-irradiated for 100 h at the Oregon State University TRIGA reactor in the Cadmium-Lined In-Core Irradiation Tube (CLICIT). Following irradiation we gently broke the friable whole-rock fragments using tweezers and selected (i) ~5 mg whole-rock chips (1–2 mm diameter) and (ii) ~5 mg pyroxene concentrates (5–10 small grains with minor adhering impurities). Due to the small mass of the whole-rock chips, mineralogical proportions likely varied from one aliquot to another. Whole-rock fragments and mineral separates were then loaded into small metal packets made from high-purity Pt–Ir tubes and incrementally degassed using feedback-controlled laser heating with an externally calibrated optical pyrometer (methods detailed in Cassata et al., 2009; Shuster et al., 2010).

During experimental heating, the sample was held at a controlled temperature for a specified duration (600 s). The released argon was purified using two SAES getters (one hot and one cold), analyzed using a Mass Analyzer Products 215 mass spectrometer, and measured statically on a Balzers SEV-217 electron multiplier using procedures similar to those described by Renne et al. (1998). Corrections were made for interfering nuclear reaction products (Renne et al., 2005), ^{37}Ar and ^{39}Ar decay, spectrometer discrimination, and extraction line blanks. Based on a power law relationship (Renne et al., 2009), the mass discrimination (1.008 ± 0.002 per atomic mass unit) was determined from analysis of 90 aliquots from an automated air pipette system, interspersed with the unknowns. Apparent ages were calculated relative to the Hb3gr standard (1080.4 Ma) using the decay constants and standard

calibration of Renne et al. (2010) and isotope abundances of Steiger and Jäger (1977) (full datasets appear in the Supplementary Files).

3.2. Regression Criteria for Arrhenius plots

Using the fractions of ^{37}Ar or ^{39}Ar and the duration of each step, we calculated the Ar diffusion coefficient (D) normalized to the characteristic length scale (D/a^2) following Feghtig and Kalbitzer (1966) and Crank (1975) and assuming plane slab geometry. To quantify diffusion kinetics from calculated values of D/a^2 following Feghtig and Kalbitzer (1966) assumes that gas is derived from a single diffusion domain containing a uniform concentration distribution. However, whole-rock meteorites clearly violate this assumption. We therefore constrain Ar diffusion kinetics using a multi-domain, multi-phase model. With this model, we were able to constrain the Ar diffusion kinetics of different phases within each meteorite by simultaneously predicting the observed ^{37}Ar and ^{39}Ar release fractions.

We used both Ca-derived ^{37}Ar and K-derived ^{39}Ar data because these isotopes are synthetically produced during neutron irradiation in the reactor and have essentially zero contribution from atmospheric blank. Additionally, as most ^{37}Ar resides within pyroxenes and most ^{39}Ar resides within maskelynite and/or plagioclase, examining both isotopes helps to distinguish and quantify diffusion kinetics in multi-phase, whole-rock samples (see discussions below). We then quantified the temperature dependence of the diffusion coefficients from weighted linear regression models of $\ln(D/a^2)$ against $1/T$ and numerical simulations (discussed in detail below).

3.3. Additional corrections

In addition to corrections for interfering nuclear reaction products on Ca and K, ^{37}Ar and ^{39}Ar decay, spectrometer discrimination, and extraction line blanks, corrections were made for reactor-produced ^{38}Ar from chlorine, cosmogenic ^{38}Ar and ^{36}Ar , and trapped ^{40}Ar prior to calculating $^{40}\text{Ar}/^{39}\text{Ar}$ ages. By isolating these components we are also able to derive a cosmic ray exposure age. We corrected Ar isotope data as follows.

3.3.1. Correcting for reactor-produced ^{38}Ar from chlorine

Contributions from chlorine-derived ^{38}Ar ($^{38}\text{Ar}_{\text{Cl}}$) can be quantified from a plot of $^{37}\text{Ar}/^{36}\text{Ar}$ vs. $^{38}\text{Ar}/^{36}\text{Ar}$ (a “cosmochron diagram”; Levine et al., 2007), provided that at least one mineral phase or several contiguous extractions are free of $^{38}\text{Ar}_{\text{Cl}}$; these steps contain a binary mixture of trapped (e.g., atmospheric) and cosmogenic Ar, where the slope (the “cosmochron”; Levine et al., 2007) defines the ratio of cosmogenic ^{38}Ar ($^{38}\text{Ar}_{\text{cos}}$) to reactor-produced ^{37}Ar ($^{37}\text{Ar}_{\text{Ca}}$). Thus, with knowledge of the production rates of $^{38}\text{Ar}_{\text{cos}}$ and $^{37}\text{Ar}_{\text{Ca}}$, the cosmic ray exposure (CRE) age can be calculated using the following equation:

$$\text{CRE}_{\text{Age}} = \left(\frac{{}^{38}\text{Ar}_{\text{cos}}}{{}^{37}\text{Ar}_{\text{Ca}}} \right) \left(\frac{\gamma}{P38_{\text{Ca}}} \right) \quad (1)$$

where $P38_{\text{Ca}}$ is the production rate of $^{38}\text{Ar}_{\text{cos}}$ relative to the Ca concentration (Turner et al., 1997) and γ , the irradiation parameter relating $^{37}\text{Ar}_{\text{Ca}}$ to Ca content, is dependant upon the duration of the irradiation, the neutron flux, and the neutron capture cross section. γ is determined by co-irradiating a natural K-bearing standard of known Ca concentration and age (in this case the Hb3gr standard, whose Ca concentration was reported by Jourdan and Renne, 2007) and measuring the $^{37}\text{Ar}_{\text{Ca}}$ and Ca contents calibrated by the $^{37}\text{Ar}_{\text{Ca}}/^{40}\text{Ar}^*$ and the $^{40}\text{Ar}^*$ concentration determined by the age. $P38_{\text{Ca}}$, adapted from Eugster and Michel (1995), is given by

$$P38_{\text{Ca}} = 8.08 + 0.44 \left(\frac{[\text{Fe} + \text{Ni}]}{[\text{Ca}]} \right) + 1.70 \left(\frac{[\text{Ti} + \text{Cr} + \text{Mn}]}{[\text{Ca}]} \right) + 1.29 \left(\frac{[\text{K}]}{[\text{Ca}]} \right) \quad (2)$$

where $P38_{\text{Ca}}$ is in units of 10^{-13} moles/Ma. CRE ages are listed in Table 1.

Steps containing measurable excesses of $^{38}\text{Ar}_{\text{Cl}}$ will plot above the cosmochron. Therefore, with knowledge of the exposure age (from the extractions that are free of $^{38}\text{Ar}_{\text{Cl}}$) and the appropriate $P38_{\text{Ca}}$ for a given step, the quantity of $^{38}\text{Ar}_{\text{Cl}}$ can be calculated using the following equation:

$$^{38}\text{Ar}_{\text{Cl}} = ^{38}\text{Ar}_T - ^{36}\text{Ar}_T \left[\left(\frac{\text{CRE}_{\text{age}} \times P38_{\text{Ca}}}{\gamma} \right) \left(\frac{^{37}\text{Ar}}{^{36}\text{Ar}} \right) + \left(\frac{^{38}\text{Ar}}{^{36}\text{Ar}} \right)_{\text{atm}} \right] \quad (3)$$

where $(^{38}\text{Ar}/^{36}\text{Ar})_{\text{atm}}$ is 0.244 for the Martian atmosphere (Bogard and Garrison, 1999) and $^X\text{Ar}_T$ indicates the total amount of a given Ar isotope of mass X . A list of production rates for various mineral phases in ALH 84001, Nakhla, and MIL 03346 can be found in the footnotes of Table 1. We work through an example of this correction procedure in Figure S1.

3.3.2. Correcting for cosmogenic ^{38}Ar and ^{36}Ar

Prior to plotting isotope ratios involving ^{36}Ar or ^{38}Ar on conventional isochron diagrams, we apply corrections for cosmogenic contributions. By simple mass balance, the chlorine-corrected $^{38}\text{Ar}/^{36}\text{Ar}$ ratio defines the proportion of cosmogenic and trapped Ar isotopes (assuming these are the only two sources) according to the following equation:

$$^{36}\text{Ar}_{\text{cos}} = ^{36}\text{Ar}_T \left(1 - \frac{1.54 - (^{38}\text{Ar}/^{36}\text{Ar})_{\text{meas}}}{1.54 - 0.244} \right) \quad (4)$$

where 1.54 is the cosmogenic $^{38}\text{Ar}/^{36}\text{Ar}$ ratio (Wieler, 2002) and 0.244 is the Martian $^{38}\text{Ar}/^{36}\text{Ar}$ ratio (Bogard and Garrison, 1999). We assume a 1% uncertainty on both of these numbers.

3.3.3. Correcting for trapped/atmospheric ^{40}Ar

We applied corrections for trapped (e.g., atmospheric) Martian ^{40}Ar using the measured abundances of $^{36}\text{Ar}_{\text{trap}}$ and the trapped $^{40}\text{Ar}/^{36}\text{Ar}$ ratios, which are constrained by the y-intercepts on traditional isochron diagrams that have been corrected for $^{36}\text{Ar}_{\text{cos}}$. Isochron diagrams from Martian meteorites are complicated by $^{40}\text{Ar}^*$ loss and

Table 1
Summary of cosmic ray exposure ages.

Aliquot phase	Cosmochron Analysis		
	Steps used	$^{38}\text{Ar}_{\text{cos}}/^{37}\text{Ar}_{\text{Ca}} \pm 1\sigma$	CRE age (Ma) $\pm 1\sigma$
ALH-1			
CPX	13–28	0.0023 ± 0.0002	11.0 ± 1.1
ALH-2			
OPX	30–42	0.0036 ± 0.0002	10.0 ± 0.6
ALH-3			
OPX	24–25	0.0044 ± 0.0004	12.3 ± 1.1
ALH-4			
OPX	34–38	0.0023 ± 0.0000	10.0 ± 0.1
NAK-1			
CPX	27–35	0.0018 ± 0.0001	8.6 ± 0.5
NAK-2			
CPX	31–34	0.0020 ± 0.0001	9.5 ± 0.5
NAK-3			
Olivine	30–33	0.0147 ± 0.0009	9.2 ± 0.5
NAK-4			
CPX	30–36	0.0019 ± 0.0001	9.1 ± 0.5
NAK-5			
CPX	30–34	0.0012 ± 0.0001	8.7 ± 0.4
MIL-1			
CPX	27–35	0.0018 ± 0.0002	8.6 ± 1.0

CRE Ages calculated using the following parameters: ^{38}Ar Prod. Rates (10^{-13} moles/gCa/Ma): ALH: OPX = 14.2; CPX = 8.30; Mask. = 8.66 Nakhla: CPX = 8.35; Oliv. = 63.6; Plag. = 9.42 MIL: CPX = 8.30 γ , which relates ^{37}Ar produced during the neutron irradiation to the mass of Ca, is 1.06×10^{11} mol/gCa (and 1.64×10^{11} mol/gCa for ALH-4 and NAK-5).

extractions that comprise contributions of trapped and radiogenic Ar derived from dissimilar mineral phases. Because an $^{40}\text{Ar}/^{39}\text{Ar}$ isochron is by definition a mixing line between a trapped ^{40}Ar component and a radiogenic ^{40}Ar component, only (i) phases that equilibrated with the same non-radiogenic ^{40}Ar component and (ii) data that are unaffected by differential $^{40}\text{Ar}^*$ loss (i.e., define a plateau after correction for an isotopically uniform trapped ^{40}Ar component) should be included in isochron regressions. Therefore, we attempt to regress each phase independently, restricting our isochrons to extraction steps in which ^{36}Ar , ^{39}Ar , ^{40}Ar can reasonably be attributed to a single mineral phase and $^{40}\text{Ar}^*$ loss is not significant. By treating the isochron data in this manner, we clearly resolve reproducible trapped $^{40}\text{Ar}/^{36}\text{Ar}$ components in ALH 84001 and Nakhla (see results section). In both meteorites it appears that pyroxenes equilibrated with a different $^{40}\text{Ar}/^{36}\text{Ar}$ ratio than maskelynite and plagioclase. If the different phases within each meteorite had equilibrated with the same non-radiogenic ^{40}Ar component, then composite and separate regressions would yield statistically indistinguishable y-intercepts (i.e., trapped $^{40}\text{Ar}/^{36}\text{Ar}$ ratios). By clearly resolving phase-specific trapped non-radiogenic ^{40}Ar components in ALH 84001, the data constrain the $^{40}\text{Ar}/^{39}\text{Ar}$ age with significantly higher precision than if these components were not resolved. We did not find any evidence of a trapped terrestrial atmospheric Ar component in these meteorites.

4. RESULTS

Ten incremental heating experiments were conducted on whole-rock and mineral concentrates of ALH 84001, Nakhla, and MIL 03346. Each sample appears to comprise two phases: a phase which releases Ar at relatively low extraction temperatures (the “low- T phase”) with low Ca/K and a phase which releases Ar at relatively high temperatures (the “high- T phase”) with high Ca/K, where the Ca/K ratio is derived from the $^{37}\text{Ar}_{\text{Ca}}/^{39}\text{Ar}_{\text{K}}$ ratio weighted by the relevant neutron capture cross sections and isotopic abundances. For the remainder of this paper we assume the low- T , low-Ca/K phase is maskelynite, plagioclase, or mesostasis glass (in the case of ALH 84001, Nakhla, or MIL 03346, respectively) and the high- T , high-Ca/K phase is pyroxene. The observed Ca/K ratios for these phases are consistent with those inferred from microprobe studies on their compositions when available (see sources in Section 2 for details). The Arrhenius plots and $^{40}\text{Ar}/^{39}\text{Ar}$ age spectra are complex and we discuss our observations separately in the following sections. Analytical results and complete stepwise degassing data appear in Table S2.

4.1. Arrhenius plots and diffusion kinetics

Whole rock fragments and mineral concentrates were subjected to one of two different types of heating schedules: monotonically increasing temperatures with duplicate isothermal steps or cycled heating (i.e., sequentially increasing, then decreasing, then increasing temperatures) with duplicate isothermal steps. In calculating D/a^2 values, cycled and isothermal heating analyses test the assumed initial

condition that ^{37}Ar and ^{39}Ar were produced uniformly throughout (and diffused from) a single diffusion domain. All three meteorites yield qualitatively similar Arrhenius plots because they have similar mineralogies and grain size distributions (Fig. 1). Therefore, we only discuss in detail the Arrhenius plot of ALH-2 (Fig. 1b), which extends to the highest temperatures and includes retrograde extractions. Although we refer to the low- T phase as maskelynite when discussing ALH-2, in Nakhla and MIL 03346 the low- T phases are plagioclase and mesostasis glass, respectively.

The ALH-2 Arrhenius plot can be explained by diffusion from a range of domain sizes (grain fragments or grains) of maskelynite and pyroxene. Simple linear regressions of the data to determine E_a and $\ln(D_0/a^2)$ would yield erroneous diffusion parameters because calculated values of D/a^2 are not solely defined by diffusion kinetics and domain size, but also reflect the relative abundance of a given isotope in maskelynite and pyroxene (discussed below). The most conspicuous aspects of the Arrhenius plot are the differences between values of D/a^2 calculated from ^{39}Ar and ^{37}Ar , particularly at low temperatures (Fig. 1b). These differences arise because whole-rock fragments of ALH 84001 contain mineral phases with considerably different Ca/K ratios and apparently different diffusion kinetics. At low temperatures (<800 °C), maskelynite is effectively the only Ar-bearing phase that is degassed while pyroxene remains largely closed with respect to Ar diffusion. Linear regressions to ^{39}Ar and ^{37}Ar values below 800 °C yield equivalent activation energies. This is because the relative isotopic abundances in those extractions, which define E_a , are nearly equivalent, reflecting a spatially uniform Ca/K ratio throughout the maskelynite fragments. The relative vertical positions of ^{39}Ar and ^{37}Ar Arrhenius arrays are controlled by the proportions of *total* ^{39}Ar or ^{37}Ar extracted. In ALH 84001 more than ~90% of the ^{39}Ar resides within maskelynite whereas only ~10% of the ^{37}Ar does (~90% of the ^{37}Ar appears to reside in pyroxene). Thus, while sequential low- T extractions yield similar relative abundances of ^{39}Ar and ^{37}Ar (i.e., because Ca/K is fairly uniform in ALH 84001 maskelynite), the fraction of the total ^{39}Ar is far greater than that of ^{37}Ar . Because calculated D/a^2 values for a given isotope are a function of the relative concentration and Ar diffusion kinetics in each phase, it follows that the diffusive frequency factor (i.e., D_0/a^2) cannot be accurately determined by simply regressing D/a^2 values against $1/T$ for polyphase materials, but instead requires a more complex model (see discussion below).

^{36}Ar and ^{38}Ar Arrhenius arrays are not parallel to the apparent ^{39}Ar and ^{37}Ar slopes (E_a), but are subtly divergent at low temperature (Fig. 1). This pattern likely indicates that trapped Martian ^{36}Ar and ^{38}Ar are concentrated near diffusion domain boundaries. Such Ar isotope enrichments toward grain margins result in (i) both inward and outward diffusion toward areas of lower concentration upon heating, and (ii) apparently low E_a 's for all steps extracted prior to homogenization or exhaustion of the grain-margin enrichment. The latter simply reflects inaccuracy in the assumed initial condition (i.e., that ^{36}Ar and ^{38}Ar concentrations are not spatially uniform). ^{36}Ar zonation is also

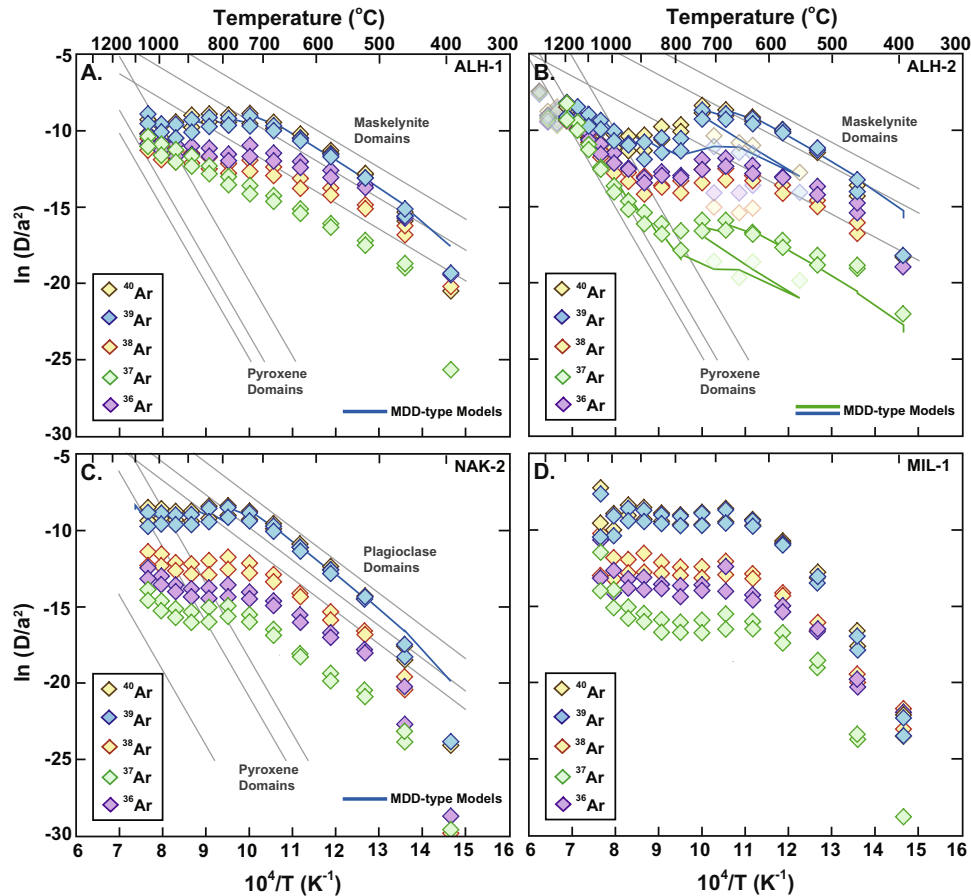


Fig. 1. Arrhenius plots for (A) ALH-1, (B) ALH-2, (C) NAK-2, and (D) MIL-1 calculated for plane slab geometry following Fechtig and Kalbitzer (1966) and Crank (1975). Uncertainties in calculated D/a^2 values and in $1/T$ are generally smaller than the symbols, and are not shown. Model Arrhenius arrays for the ^{37}Ar and ^{39}Ar diffusion parameters and domain distributions are shown as solid lines behind the data. Lighter data represent retrograde heating steps.

responsible for the spread observed on isochron diagrams, which portray variations in the relative proportions of trapped and radiogenic Ar isotopes. Like ^{37}Ar and ^{39}Ar , the relative positions of ^{36}Ar and ^{38}Ar Arrhenius arrays are determined by their abundances in the low- and high- T phases. Because cosmogenic ^{38}Ar and ^{36}Ar (for which $^{38}\text{Ar}/^{36}\text{Ar} = 1.54$; Wieler, 2002) are each more abundant in OPX, whereas maskelynite contains more trapped Martian ^{38}Ar and ^{36}Ar (for which $^{38}\text{Ar}/^{36}\text{Ar} = 0.244$; Bogard and Garrison, 1999), the proportion of total ^{36}Ar diffused in low temperature extractions is greater, resulting in higher ^{36}Ar D/a^2 values.

4.2. Quantifying Ar diffusion kinetics

We determined the E_a of Ar diffusion in maskelynite by linear regression of low-temperature ^{39}Ar data ($<650^\circ\text{C}$), while ignoring initial steps that form curvilinear arrays with diminished D/a^2 values (see discussion below). In order to be included in E_a calculations, steps were required to yield reproducible D/a^2 values for duplicate isothermal extractions and not depart from linear arrays on Arrhenius plots. These selection criteria ensure that a single domain of the

least retentive phase dominates the release fractions and therefore that our E_a calculation is valid and applicable to that phase (e.g., Lovera et al., 1991). Extractions in this temperature range are characterized by uniform Ca/K ratios and yield activation energies of 120–175 kJ/mol (Table 2).

The lowest- T , curvilinear steps that were excluded from E_a calculations reveal information that bears on the geochronology of these samples. Several experimental or mineralogical artifacts can yield lower than expected D/a^2 values in initial extractions, including recoil loss of Ar, diffusive loss of Ar prior to analysis due to heating during irradiation and/or extraction line bake-out, zonation with lower Ar concentration at the diffusion boundary, or some combination of these. While ^{39}Ar recoil loss from maskelynite undoubtedly exists at some level, the curvilinear arrays with diminished D/a^2 values cannot be explained by recoil alone. ^{36}Ar and ^{38}Ar , which are not subject to reactor-induced recoil, and ^{37}Ar , which may be enriched near some maskelynite grain boundaries (e.g., due to recoil ^{37}Ar implantation from neighboring high-Ca phases), also form downward curving low- T Arrhenius arrays. The observation that all Ar isotopes form curvilinear Arrhenius arrays

Table 2

Summary of $^{40}\text{Ar}/^{39}\text{Ar}$ diffusion parameters.

Sample	Plagioclase/Maskelynite							Pyroxene						
	E_a (kJ/mol)	$\ln(D_0/a^2)_1$ ($\ln(\text{s}^{-1})$)	Φ_1	$\ln(D_0/a^2)_2$ ($\ln(\text{s}^{-1})$)	Φ_2	$\ln(D_0/a^2)_3$ ($\ln(\text{s}^{-1})$)	Φ_3	E_a (kJ/mol)	$\ln(D_0/a^2)_1$ ($\ln(\text{s}^{-1})$)	Φ_1	$\ln(D_0/a^2)_2$ ($\ln(\text{s}^{-1})$)	Φ_2	$\ln(D_0/a^2)_3$ ($\ln(\text{s}^{-1})$)	Φ_3
ALH-1	140	5.5	0.15	7.5	0.25	9.5	0.45	406	24.0	0.05	25.5	0.05	29.0	0.05
ALH-2	126	4.1	0.05	7.2	0.42	8.8	0.40	406	24.0	0.02	25.5	0.05	29.0	0.06
NAK-2	177	10.3	0.17	11.5	0.18	13.6	0.50	406	20.0	0.02	28.0	0.04	30.5	0.04

Each sample is fit with a six domain model.

 Φ is the fraction of ^{39}Ar contained within a given domain.

with initially low D/a^2 values is consistent with minor amounts of diffusive loss prior to analysis. It is likely that all Ar isotopes within maskelynite were partially degassed during both irradiation [100 hours at $\sim 270^\circ\text{C}$ (Shuster and Farley, 2009)] and extraction line bake-out (10 hours also at $\sim 270^\circ\text{C}$), which, based on Ar diffusion kinetics as quantified above, are sufficient to partially diffuse Ar from the smallest maskelynite domains. Therefore, $^{40}\text{Ar}/^{39}\text{Ar}$ ages calculated from initial, low- T maskelynite extractions may not directly quantify the timing of the most recent episodes of Ar loss. This may explain some of the initial age discrepancies observed between different aliquots of ALH 84001. To more accurately model these experimental conditions we simulated 110 hours of heating at 270°C prior to generating model Arrhenius plots and excluded the gas released in this step from the total quantity of a given isotope, which is used to calculate diffusion coefficients.

Above $\sim 650^\circ\text{C}$, the linear Arrhenius arrays used to quantify the E_a break down and D/a^2 values are lower than expected from upward extrapolation of the low- T linear Arrhenius relationships described above. These deviations from linearity probably result from the sequential exhaustion of small domains (grain fragments) and/or grains of maskelynite. Given that these are stepped-heating analyses of fragmented and multi-phase whole-rock samples, we expect a distribution of diffusive length scales. We further expect the distribution to be relatively discrete, since a limited number of maskelynite fragments are contained within a given ~ 5 mg aliquot. Therefore, we constructed a model in which each mineral has multiple diffusion domains with invariant E_a and D_0 , but a range of diffusive length scales [i.e., variation in a ; hereafter termed “MDD-type models”, conceptually similar to those of Lovera et al. (1991)]. However, we do not have independent knowledge of the actual domain size distribution within each sample and cannot confirm that one E_a should characterize all domains of a given phase. Cassata et al. (2009) recently demonstrated that individual plagioclase grains from a single terrestrial hand sample have subtly different E_a . Nonetheless, we assume (i) all domains of a given phase share a common E_a , (ii) pyroxene and maskelynite are the only Ar-bearing phases, and (iii) the relative phase proportions are constrained by the Arrhenius plots. We describe our method for fitting Arrhenius plots with MDD-type models at the end of this section.

Between 900 and 1000°C , the apparent Ca/K ratio increases sharply (Fig. 2b) suggesting that pyroxene begins to degas significantly. Due to the strong contrast in diffusion kinetics, increasing the number of low-temperature labora-

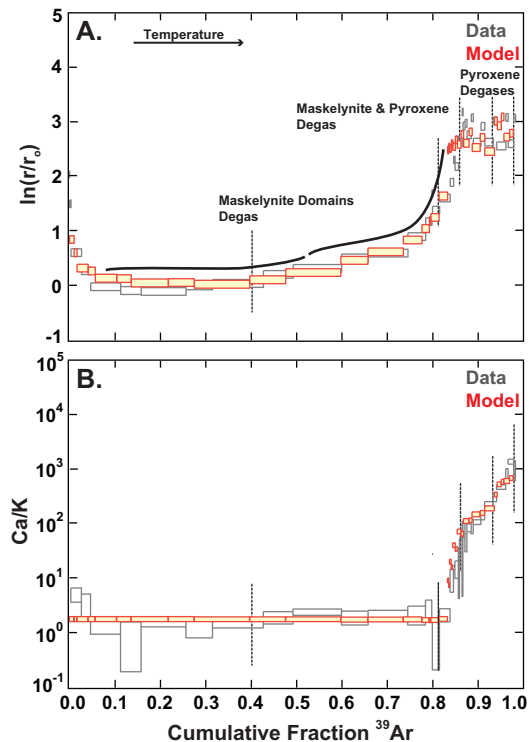


Fig. 2. Plot of the cumulative fraction of ^{39}Ar vs. (A) Ca/K and (B) $\ln(r/r_0)$ (the difference between the natural logarithm of a given D/a^2 value and that expected from the low-temperature Arrhenius relationship) for ALH-2. Data are shown in grey and models are shown in red. Dashed lines indicate the fraction of ^{39}Ar contained within a given maskelynite or pyroxene domain (see text for discussion). The multi-domain, multi-phase diffusion models were optimized to reproduce both the Ca/K and $\ln(r/r_0)$ spectra.

tory steps (i.e., more completely exhausting the lower E_a phase before tapping the higher E_a phase) permits better resolution of Ar diffusion kinetics in maskelynite from that in pyroxene. The rapid transition between the relative proportions of gas released from these phases appears as a steep segment of positive slope on a $\ln(r/r_0)$ plot (the difference between the natural logarithm of a given D_0/a^2 value and that expected from extrapolation of the low-temperature Arrhenius relationship; Lovera et al., 1991) (Fig. 2a). We estimated the E_a of the more retentive phase (which we assume to be pyroxene) by linear regression of ^{37}Ar data acquired above $\sim 1000^\circ\text{C}$. Any E_a determined in this manner represents a minimum constraint because (i) calculated values of D/a^2

typically do not replicate between isothermal steps (i.e., indicating that multiple pyroxene domains may be present), and (ii) the initial pyroxene extractions included in E_a calculations may contain minor contributions of ^{37}Ar from the incompletely depleted, less retentive phase and may therefore result in artificially high values of $\ln(D/a^2)$.

For each analysis, we used three low- T and three high- T domain sizes to predict the Ar release patterns. To constrain the $\ln(D_o/a^2)$ for each domain (and the E_a of pyroxene for samples in which temperature was not monitored above $\sim 1100^\circ\text{C}$) we minimized the error-weighted least-squares differences between the observed and predicted values of $\ln(D/a^2)$ using numerical simulations. We roughly assigned the fraction of ^{39}Ar within each maskelynite domain (Φ_i) by assuming that minor segments of positive slope that separate sub-horizontal, low- T arrays on plots of the cumulative fraction of ^{39}Ar vs. $\ln(r/r_o)$ represent the sequential exhaustion of maskelynite domains (Fig. 2a). Thus the proportion of total ^{39}Ar between two segments of positive slope on a $\ln(r/r_o)$ plot defines the quantity of ^{39}Ar in a given domain (Fig. 2a). The quantity of ^{37}Ar in a given maskelynite domain is determined relative to ^{39}Ar using the observed Ca/K ratio (Fig. 2b). The remaining ^{37}Ar and ^{39}Ar are partitioned into pyroxene domains such that the observed Ca/K and $\ln(r/r_o)$ plots are reproduced. This procedure is somewhat subjective and solutions are not unique. Various combinations of E_a and domain $\ln(D_o/a^2)$ values can predict the Ar release patterns. For example, in Figure S2 we show three MDD-type models that predict the observations: one using the E_a determined by linear regression of the pyroxene data, one with a higher pyroxene E_a , and one with a lower pyroxene E_a . Although the MDD-type models are not unique, linear regressions of the pyroxene data should constrain the minimum pyroxene E_a (see discussion above). Diffusion kinetics and domain distributions for each modeled dataset are given in Table 2.

To summarize, ALH 84001, Nakhla, and MIL 03346² Arrhenius plots (Fig. 1) can be explained by diffusion from a range of domain (grain) sizes of either maskelynite or plagioclase and pyroxene. Simple linear regressions of the data to determine E_a and $\ln(D_o/a^2)$ would yield erroneous diffusion parameters for these multi-phase, multi-domain meteorites. Due to relatively high diffusivity of Ar in fine-grained maskelynite and plagioclase fragments, it appears that small but significant quantities of Ar may have been degassed during irradiation and extraction line bake-out. Initial extractions that define curvilinear Arrhenius arrays with anomalously low values of D/a^2 for all Ar isotopes can be explained by diffusive loss associated with this pre-analysis heating. Because small fractions of Ar may have been lost under laboratory conditions prior to incremental heating analyses, ages calculated from the first extraction may not directly have geochronological significance (particularly in the case of maskelynite, as discussed above).

Finally, by simultaneously examining Arrhenius plots, $\ln(r/r_o)$ plots, and Ca/K spectra, we are able to identify steps derived primarily from maskelynite, pyroxene, or two-phase mixtures, which guides quantitative regression of isochron data obtained from polyphase extraterrestrial materials that have been subjected to episodic Ar loss events.

4.3. Geochronological results

4.3.1. ALH 84001

ALH 84001 age spectra appear to reflect two diffusive loss profiles: a low- T segment derived from maskelynite (low Ca/K; best illustrated on a plot of age against cumulative fraction of ^{39}Ar ; Fig. 3b, e, h, k) and a high- T segment derived from pyroxene (high Ca/K; best illustrated on a plot of age against cumulative fraction of ^{37}Ar ; Fig. 3c, f, i, l). Both phases preserve geochronological information and individual aliquots yield a range of ages and degree of age discordance (Table 3).

Maskelynite in ALH-1 (the low- T portion of the age spectrum) yields an isochron age of $4163 \pm 35 \text{ Ma}^3$ with a trapped $^{40}\text{Ar}/^{36}\text{Ar}$ ratio of 626 ± 100 (Fig. 4a) and defines a plateau at $4146 \pm 15 \text{ Ma}$ (Fig. 3b; Table 3), which is indistinguishable from several previous results (Ash et al., 1996; Turner et al., 1997; Bogard and Garrison, 1999). Maskelynite in ALH-2 (Fig. 3e) and ALH-4 (Fig. 3k) do not form plateaus, but rather monotonically increase to “apparent plateaus”⁴ at 4000 ± 16 and $4086 \pm 11 \text{ Ma}$, respectively. These apparent plateaus comprise $<60\%$ of the total ^{39}Ar and represent minimum crystallization ages. An isochron regression of ALH-4 data unaffected by differential radiogenic Ar loss (i.e., the apparent plateau segments) yields a trapped $^{40}\text{Ar}/^{36}\text{Ar}$ ratio of 514 ± 450 (Table 3; Fig. 4d). Maskelynite ages from ALH-3 are less precisely determined as this aliquot was gently crushed and selected for its high pyroxene concentration. It yields an isochron age of $3844 \pm 148 \text{ Ma}$ with a trapped $^{40}\text{Ar}/^{36}\text{Ar}$ ratio of 694 ± 230 (Table 3; Fig. 4c), which represents a minimum crystallization age as maskelynite has likely been fragmented in the crushing process and extractions cannot be interpreted to reflect the original $^{40}\text{Ar}^*$ gradient across intact grains.

The pyroxene-derived segments of the age spectra also contain variably discordant results. Aliquots that yielded the most discordant maskelynite age spectra also yielded the most discordant pyroxene spectra, although pyroxene portions of the age spectra are always more discordant than the maskelynite portions. Pyroxene in ALH-3 yields a plateau age at $1158 \pm 110 \text{ Ma}$ (Fig. 3i). Pyroxene ages in ALH-

² The low- T phase in MIL-1 (mesostasis glass) has a highly variable Ca/K ratio, which indicates that ^{37}Ar and ^{39}Ar may be zoned. Duplicate isothermal extractions do not yield reproducible $\ln(D/a^2)$ values and therefore the E_a is unconstrained. This sample was not used for thermal modeling.

³ Uncertainties on all isochron, plateau, crystallization, and shock ages reported in this paper include the decay constant uncertainty and are directly comparable to other geochronologic data.

⁴ We use the term “apparent plateau” to refer to series of consecutive steps that have indistinguishable ages and no resolvable slope but comprise less than 80% of the total ^{39}Ar contained within a given phase (e.g., the first 20% of the maskelynite portion of the spectrum is discordant). Apparent plateaus observed within age spectra exhibiting diffusive loss profiles may significantly underestimate the true age of a rock.

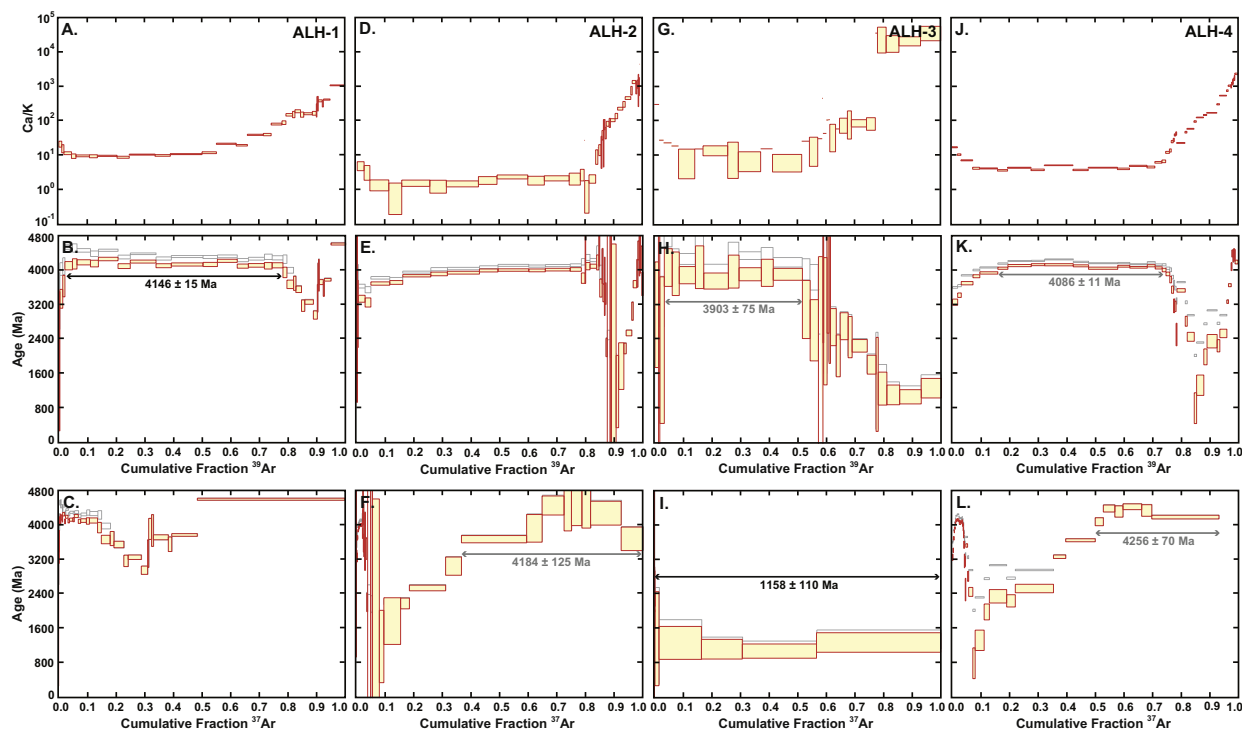


Fig. 3. Apparent age and Ca/K spectra for ALH 84001. Age spectra are plotted against the cumulative fraction of ^{39}Ar and ^{37}Ar . Uncorrected ages are shown in grey behind the data corrected for trapped, cosmogenic, and Cl-derived Ar isotopes, which are shown in red.

2 (Fig. 3f) and ALH-4 (Fig. 3l) increase from minima at 1187 ± 837 and 1328 ± 236 Ma to apparent plateaus at 4184 ± 125 and 4256 ± 70 Ma, respectively. These age minima are indistinguishable from the 1158 ± 110 Ma pyroxene plateau age observed in ALH-3. The apparent plateaus observed in ALH-2 and ALH-4 are indistinguishable from Pb–Pb crystallization ages (e.g. Bouvier et al., 2009a) and the 4163 ± 35 Ma maskelynite $^{40}\text{Ar}/^{39}\text{Ar}$ age. Isochron data from pyroxene in ALH-3 can be used to constrain a trapped $^{40}\text{Ar}/^{36}\text{Ar}$ ratio because pyroxene in this aliquot is unaffected by differential Ar loss (i.e., it forms a plateau after corrections for trapped ^{40}Ar), whereas pyroxenes in other aliquots of ALH 84001 are discordant and therefore do not define isochrons. Although imprecise, the trapped $^{40}\text{Ar}/^{36}\text{Ar}$ ratio in ALH-3 pyroxene is 6 ± 13 .

In summary, maskelynite within ALH 84001 yields a range of ages, the maximum of which (4163 ± 35 Ma) is indistinguishable from Pb–Pb and Lu–Hf crystallization ages, indicating that (i) maskelynite formed shortly following crystallization or (ii) maskelynite preserves the original crystallization age (i.e., it formed without significant $^{40}\text{Ar}^*$ loss). Both pyroxene and, to a lesser extent, maskelynite age spectra are variably discordant (i.e., pyroxene portions of the age spectra are most discordant). The spread in $^{40}\text{Ar}/^{39}\text{Ar}$ data toward ages younger than 4.16 Ga suggests that a post-crystallization thermal event differentially degassed ^{40}Ar from individual aliquots, either as a result of differing diffusion kinetics, differing grains size distributions, or small-scale temperature variations during the thermal event. Maskelynite fragments in aliquots of ALH 84001 yield concordant trapped $^{40}\text{Ar}/^{36}\text{Ar}$ ratios, the

weighted average of which is 632 ± 90 (maskelynite portions of the age spectra were corrected for non-radiogenic ^{40}Ar using this value).

4.3.2. Nakhla

Like those in ALH 84001, Nakhla Ar isotopes appear to be derived from multiple mineral phases, including plagioclase, CPX, and minor olivine. Compared to maskelynite in ALH 84001, the plagioclase in Nakhla is more retentive of Ar at low temperatures, with Ar diffusion kinetics more similar to pyroxene (Table 2). Due to the smaller apparent contrast in E_a between plagioclase and pyroxene in Nakhla, these phases are less well resolved in the stepped heating analysis and more extensive portions of the age spectra contain Ar isotopes derived from both phases (e.g., Fig. 5b, e, h). Because most of the ^{40}Ar and ^{39}Ar are contained within plagioclase, the uncorrected $^{40}\text{Ar}/^{39}\text{Ar}$ ratio in mixed-phase extractions is negligibly affected by minor contributions from pyroxene. However, much of the ^{36}Ar in these extractions is derived from pyroxene, wherein cosmogenic ^{36}Ar is abundant, rendering accurate corrections for non-radiogenic ^{40}Ar in multiphase extractions impossible. Simply using the trapped $^{40}\text{Ar}/^{36}\text{Ar}$ ratio determined for plagioclase to correct extractions that are contaminated by pyroxene-derived ^{36}Ar will result in a spurious reduction in $^{40}\text{Ar}^*$. These steps (indicated on Fig. 5b, e, h), despite comprising considerable portions of Nakhla age spectra, are indeterminate and were not included in age calculations.

The lowest- T steps (which presumably sample plagioclase grain margins) contain significant abundances of trapped Ar ($^{40}\text{Ar}_t$), which gradually decreases in concentration

Table 3
Summary of $^{40}\text{Ar}/^{39}\text{Ar}$ incremental heating results.

Aliquot (material)	Age Spectrum Analysis ^{a,b,c}				Isochron Analysis ^{a,b}			
	Phase	Feat. ^d	MSWD	Age ^e (Ma) $\pm 1\sigma$	Steps used	$^{40}\text{Ar}/^{36}\text{Ar}_i \pm 1\sigma$	MSWD	Age ^e (Ma) $\pm 1\sigma$
ALH-1 (wr fragment)	Mask	P	1.30	4146 \pm 15	4–14	626 \pm 100	2.90	4163 \pm 35
	OPX	–	–	– \pm –	–	– \pm –	–	– \pm –
ALH-2 (wr fragment)	Mask	AP	0.09	4000 \pm 16	–	\pm	–	– \pm –
	OPX	AP	1.14	4184 \pm 125	–	– \pm –	–	– \pm –
ALH-3 (opx concentrate)	Mask	AP	0.12	3903 \pm 75	2–12	694 \pm 230	0.18	3844 \pm 148
	OPX	P	0.16	1158 \pm 110	26–30	6 \pm 13	0.31	1147 \pm 283
ALH-4 (wr fragment)	Mask	AP	1.50	4086 \pm 11	6–16	514 \pm 450	6.10	4088 \pm 86
	OPX	P	3.30	4256 \pm 70	–	\pm	–	– \pm –
					<i>Preferred Age of Maskelynite</i>			
					<i>Preferred Age of Shock Event</i>			
								4163 \pm 35
								1158 \pm 110
NAK-1 (wr fragment)	Plag	P	0.77	1345 \pm 9	6–16	676 \pm 4900	7.50	1389 \pm 247
	CPX	WA	0.79	1042 \pm 15	29–35	42 \pm 10	0.30	1008 \pm 255
NAK-2 (wr fragment)	Plag	P	8.70	1378 \pm 9	6–16	676 \pm 4900	7.50	1389 \pm 247
	CPX	P	3.60	913 \pm 9	28–33	58 \pm 30	0.23	642 \pm 128
NAK-3 (Ol. concentrate)	Olivine	P	0.24	1215 \pm 160	23–33	213 \pm 120	0.05	1005 \pm 194
NAK-4 (Ol. concentrate)	CPX	P	0.62	906 \pm 50	29–37	–4 \pm 17	0.34	1070 \pm 135
NAK-5 (wr fragment)	Plag	P	1.70	1329 \pm 9	1–18	2430 \pm 570	13.00	1303 \pm 31
	CPX	WA	0.64	1105 \pm 46	–	– \pm –	–	– \pm –
					<i>Preferred Crystallization Age</i>			
					<i>Preferred Age of Shock Event</i>			
								1332 \pm 24
								913 \pm 9
MIL-1 (wr fragment)	Glass	P	0.64	1373 \pm 11	5–10	1425 \pm 230	1.70	1367 \pm 19
	CPX	WA	14.00	1369 \pm 22	22–33	28 \pm 8	4.30	1333 \pm 9
					<i>Preferred Crystallization Age</i>			
								1339 \pm 8

Preferred ages are derived from the most concordant age spectra or isochrons. Age uncertainties include the decay constant uncertainty and are directly comparable to other geochronologic data

^a Ages calculated using the decay constants of Renne et al. (2010) and isotope abundances of Steiger and Jäger (1977).

^b Ages calculated relative to Hb3gr fluence monitor (1080.4 Ma; standard calibration of Renne et al., 2010).

^c Apparent age data corrected using the following trapped $^{40}\text{Ar}/^{36}\text{Ar}$ ratios [ALH: OPX/CPX = 5 \pm 5; Maskelynite = 632 \pm 90], [Nakhla: CPX/OPX = 32 \pm 9; Olivine = 213 \pm 120; Plag. = 2287 \pm 430], [MIL: CPX = 28 \pm 8; Mesostasis Glass = 1425 \pm 230].

^d Ages listed corresponds to the following features P = plateau age; AP = apparent plateau age; WA = weighted average age.

^e Ages listed in bold were used to calculate preferred crystallization and shock ages.

with increasing extraction temperature (5b, e, h). This zoned $^{40}\text{Ar}_i$ distribution yields monotonically decreasing age spectra if Ar isotope data are not adequately corrected for atmospheric contributions (Park et al., 2009). Plagioclases in NAK-1, NAK-2, and NAK-5 yield isochron ages of 1389 \pm 247 (Fig. 4e), 1373 \pm 37 (Fig. 4f), and 1303 \pm 31 Ma (Fig. 4g), with trapped $^{40}\text{Ar}/^{36}\text{Ar}$ ratios of 676 \pm 4900, 2119 \pm 670, and 2430 \pm 570, respectively (Table 3). All 3 aliquots yield concordant trapped $^{40}\text{Ar}/^{36}\text{Ar}$ ratios, the weighted average of which is 2287 \pm 430; extractions included in plateau age calculations have been corrected using this value.

The Nakhla pyroxene and olivine age spectra are variably discordant. Spatial $^{40}\text{Ar}^*$ distributions in clinopyroxene grains in NAK-2 (Fig. 5f) and NAK-4 (Fig. S3b) appear most significantly reset; the age spectra define plateaus at 913 \pm 9 and 906 \pm 50 Ma, respectively. An olivine

concentrate (NAK-3; Fig. S3a) forms an apparent plateau at 1215 \pm 160 Ma, which is indistinguishable from the crystallization age.

To summarize, plagioclase fragments within Nakhla yield concordant isochron ages, the weighted average of which is 1332 \pm 24 Ma. Initial plagioclase extractions and nearly all pyroxene extractions are discordant. The spread in $^{40}\text{Ar}/^{39}\text{Ar}$ data toward ages younger than 1332 Ma indicates that a subsequent thermal event partially and heterogeneously degassed $^{40}\text{Ar}^*$ from Nakhla. Pyroxene appears to have been more significantly reset by this thermal event.

4.3.3. MIL 03346

The release pattern of MIL 03346 is qualitatively similar to Nakhla, presumably in part because they are both clinopyroxenites (Fig. 5j, k, l). Steps that unambiguously comprise only mesostasis glass-derived Ar isotopes without

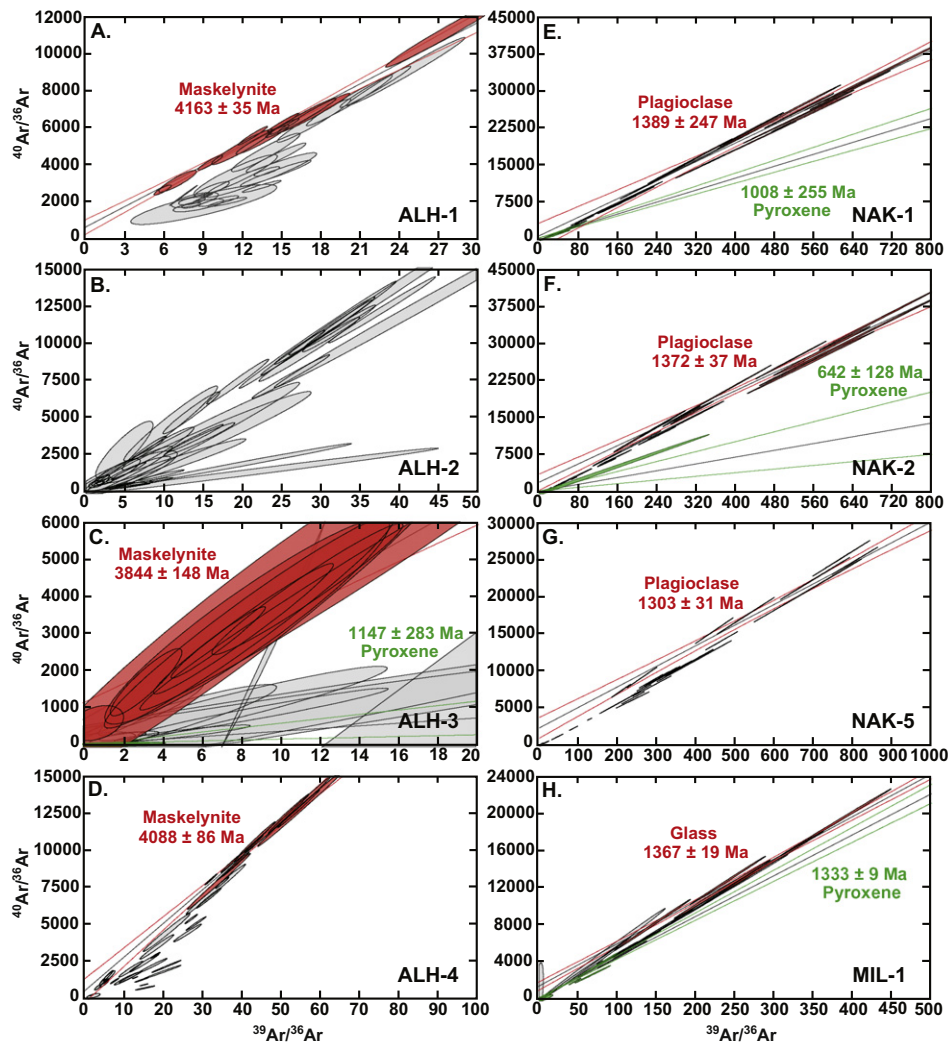


Fig. 4. Normal isochron diagrams for ALH 84001, Nakhla, and MIL 03346. Data included in maskelynite (ALH 84001), plagioclase (Nakhla), or mesostasis glass (MIL 03346) age calculations are shown in red (see text for discussion of data selection). Data included in pyroxene age calculations are shown in green. Error ellipses reflect the correlated, 1σ uncertainty. The error envelopes on the isochron regressions represents the 95% confidence interval (2σ uncertainty expanded by the square-root of the MSWD and the Student's T multiplier on $n-1$ degrees of freedom).

evidence for differential radiogenic Ar loss yield an isochron age of 1367 ± 19 Ma with a trapped $^{40}\text{Ar}/^{36}\text{Ar}$ ratio of 1425 ± 230 (Table 3; Fig. 4h). Pyroxene extractions in MIL 03346 yield an isochron age of 1333 ± 9 Ma (Table 3; Fig. 4h), which is statistically indistinguishable from that of the mesostasis glass. Similarly, Park et al. (2009) obtained an age of 1334 ± 54 Ma for a pyroxene concentrate. Thus, it appears that pyroxene in MIL 03346, unlike that in Nakhla and ALH 84001, has not been significantly disturbed by a thermal event. Although pyroxene and mesostasis glass isochron ages in MIL 03346 agree, pyroxene has a lower trapped $^{40}\text{Ar}/^{36}\text{Ar}$ ratio (28 ± 8). Pyroxenes in both Nakhla and MIL 03346 have similar, unusually low trapped $^{40}\text{Ar}/^{36}\text{Ar}$ ratios (~ 30), which might be consistent with formation in a mantle source region that is enriched in primordial ^{36}Ar and geochemically depleted (i.e., low K).

5. DISCUSSION

5.1. High-temperature age discordance and shock events

ALH 84001 age spectra contain a feature that is commonly observed in extraterrestrial rocks: a decrease in the ages of high temperature extractions relative to lower temperature steps and a correlated increase in Ca/K, often succeeded by a monotonic increase in ages. This feature has previously been attributed to recoil-implanted ^{39}Ar from a potassium (K)-rich donor phase into a K-poor receptor phase, and has generally not been ascribed to diffusive ^{40}Ar distributions within pyroxene (e.g., Turner and Cadogan, 1974; Huneke and Smith, 1976). While ^{39}Ar recoil redistribution is undoubtedly manifested in many terrestrial and extraterrestrial $^{40}\text{Ar}/^{39}\text{Ar}$ whole-rock age

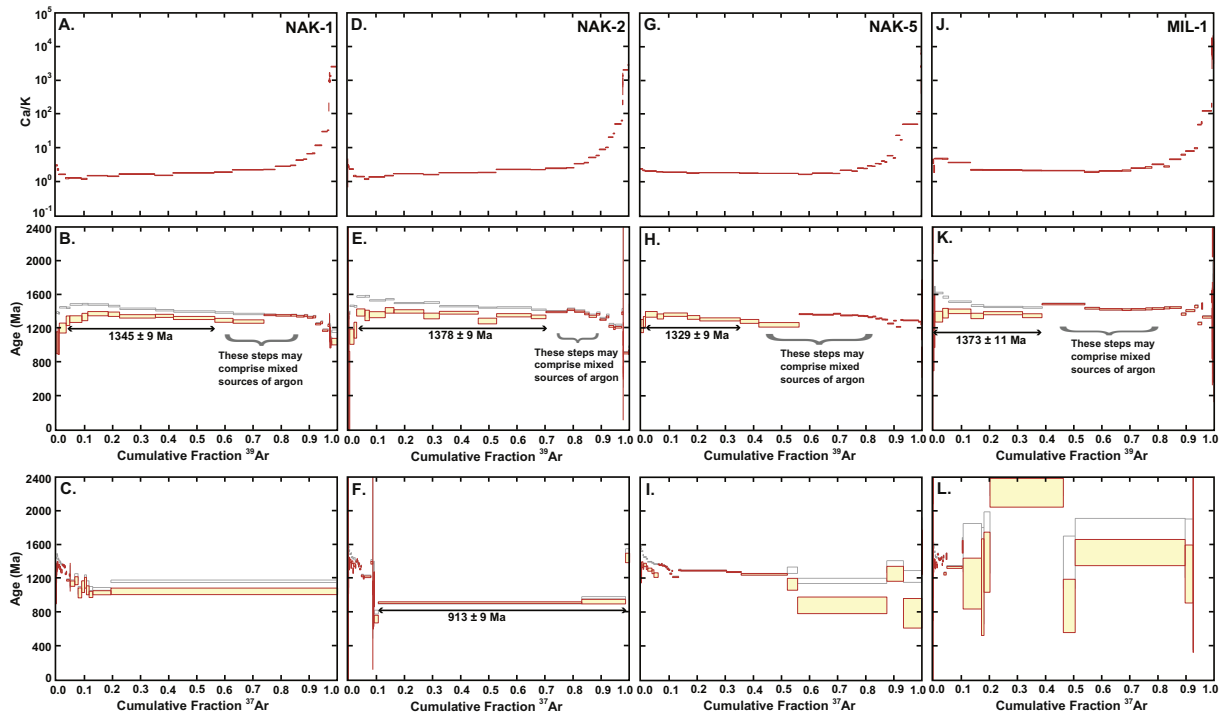


Fig. 5. Apparent age and Ca/K spectra for Nakhla and MIL 03346. Age spectra are plotted against the cumulative fraction of ^{39}Ar and ^{37}Ar . Uncorrected ages are shown in grey behind the data corrected for trapped, cosmogenic, and Cl-derived Ar isotopes, which are shown in red.

spectra, it cannot easily explain the magnitude of $^{40}\text{Ar}/^{39}\text{Ar}_K$ anomalies observed in high- T extractions from Martian meteorites ALH 84001 and Nakhla. In the following sections we discuss the shortcomings of the recoil hypothesis and propose an alternative mechanism based on strongly contrasting E_a of the different K-bearing phases to explain this feature.

5.1.1. Constraints imposed by mass balance

We can estimate the abundance of recoil-implanted ^{39}Ar that is required to explain the observed decrease in ages of high- T steps by assuming that all ages younger than the crystallization age are due to excess ^{39}Ar . For example, if we assume that the true age of pyroxene in ALH 84001 is 4.16 Ga, then the $^{40}\text{Ar}/^{39}\text{Ar}_K$ ratios observed in pyroxene from ALH-3, which yields a plateau age of 1158 ± 110 Ma, reflect the recoil implantation of 26% of the total ^{39}Ar generated in maskelynite. This simple calculation represents a minimum constraint, because we assume no ^{39}Ar is recoiled out of the system or implanted into non-pyroxene phases, which is geometrically and physically impossible. As the mean recoil distance of ^{39}Ar is $\sim 0.1 \mu\text{m}$ (Huneke and Smith, 1976), this suggests that the average maskelynite fragment is less than 1 μm in width. In fact, in a detailed study of ^{39}Ar recoil, Jourdan et al. (2007) found that only 3% of the total ^{39}Ar was lost from a $< 5 \mu\text{m}$ size fraction of sanidine crystals. This suggests that the amount of recoil occurring in ALH 84001 would be extraordinarily high. If the young high- T step ages of ALH 84001 are indeed an artifact of extraordinary ^{39}Ar recoil, we should observe anomalously old ages over significant portions of the mask-

elynite age spectra (i.e., from which the recoiled ^{39}Ar would have been ejected) (e.g., Trieloff et al., 1998). However, maskelynite in ALH-1 yields a plateau over $> 90\%$ of the total ^{39}Ar (Fig. 3a), which is necessarily unaffected by recoil (except when ^{39}Ar recoil loss serendipitously balances diffusive ^{40}Ar loss perfectly). Furthermore, the first $\sim 10\%$ of the total ^{39}Ar is associated with sub-plateau ages, rather than older ages as predicted by the recoil hypothesis.

5.1.2. Constraints imposed by mineralogy and texture

Depending on the aliquot, 25–100% of the pyroxene-dominated portions of release spectra in ALH 84001 (and Nakhla) appear strongly perturbed to lower ages (Figs. 3 and 5). Because the mean recoil distance of ^{39}Ar is $\sim 0.1 \mu\text{m}$ (Huneke and Smith, 1976), the recoil hypothesis demands that a high-K phase be ubiquitously distributed amongst sub-micron to micron sized pyroxene crystals to account for the observed pyroxene age spectra. However, in both Nakhla and ALH 84001, pyroxene is often completely isolated from high-K phases (adjacent to other grains of pyroxene, olivine, carbonate, etc.) and individual grains commonly exceed 100 μm in diameter. $^{40}\text{Ar}/^{39}\text{Ar}$ analyses of pyroxene-bearing terrestrial basalts, wherein fine-grained pyroxene and plagioclase are intimately adjoined, show that recoil-implanted ^{39}Ar into pyroxene produces much less precipitous, and often imperceptible, anomalies in $^{40}\text{Ar}/^{39}\text{Ar}_K$, as predicted by the recoil length scale. This apparent inconsistency in the recoil hypothesis was recognized in the recent study of Nakhla $^{40}\text{Ar}/^{39}\text{Ar}$ age spectra by Park et al. (2009), who noted that grain size does not correlate with the magnitude of the observed anomaly.

5.1.3. Effects of Alteration

It has been suggested that aqueous alteration may cause some of the observed high- T age discordance in Martian meteorites (e.g., Turner et al., 1997). While some localized aqueous deposits are present in ALH 84001 (as well as Nakhla and MIL 03346), extensive alteration that has pervasively modified pyroxene and maskelynite is not observed. In a recent TEM investigation, Barber and Scott (2006) found no evidence for aqueous alteration in ALH 84001 pyroxene crystals. Furthermore, alteration products are more abundant in MIL 03346 than ALH 84001 and Nakhla, but we do not observe anomalously young ages in high temperature extractions. Thus aqueous alteration is not an adequate explanation for high- T age discordance in these rocks.

5.1.4. The shock degassing hypothesis

An alternative hypothesis is that the anomalously low ages commonly observed at high release temperatures of whole-rock, extraterrestrial age spectra reflect diffusive $^{40}\text{Ar}^*$ distributions within degassed pyroxene grains. Several investigators (e.g., Wang et al., 1980; Kunz et al., 1997) have proposed that high- T portions of extraterrestrial age spectra reflect diffusive $^{40}\text{Ar}^*$ distributions in pyroxene, but this hypothesis has only been considered qualitatively for ALH 84001 (Turner et al., 1997).

As previously noted, pyroxene in ALH-3 yields a plateau age at 1158 ± 110 Ma (Fig. 3i). Pyroxenes in ALH-2 (Fig. 3f) and ALH-4 (Fig. 3l) do not yield age plateaus, but yield minimum step ages of 1187 ± 837 and 1328 ± 236 Ma, respectively. Collectively, these data sug-

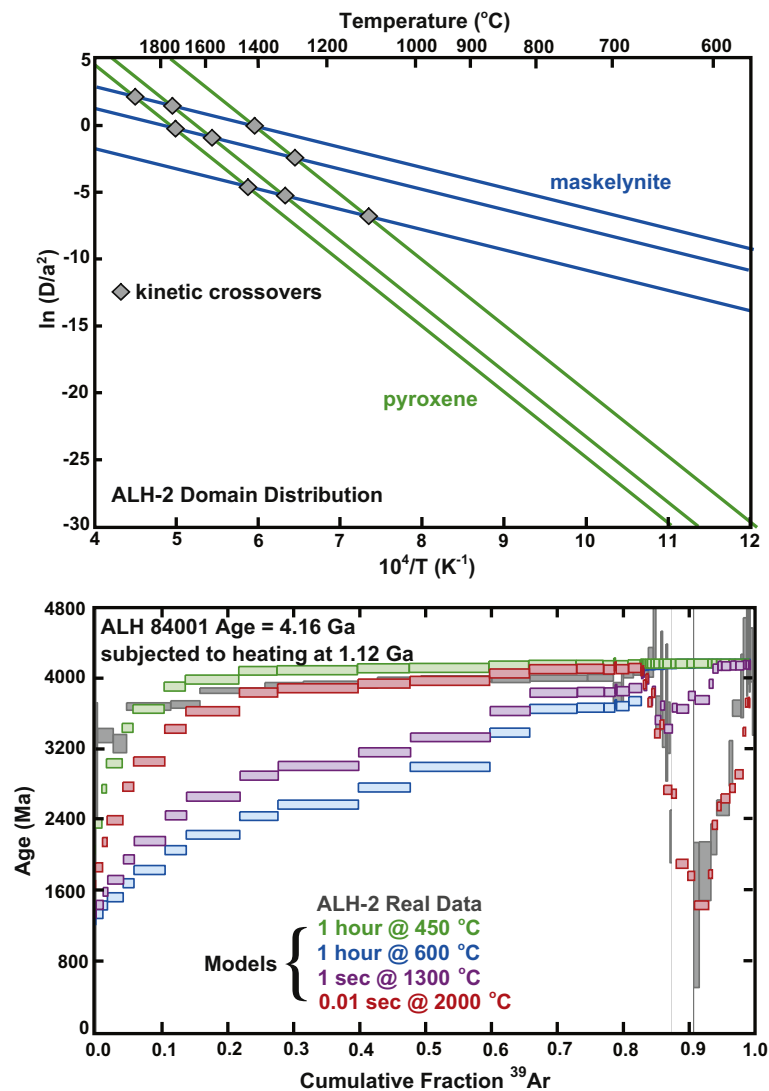


Fig. 6. (A) Maskelynite (blue) and pyroxene (green) diffusion domains modeled for ALH-2 (see Fig. 1b for calculated $\ln(D/a^2)$ values and Table 2 for the diffusion parameters and domain distribution). Grey diamonds indicate kinetic crossovers. At temperatures above the kinetic crossovers, Ar diffusivity is higher in a given pyroxene domain than in a given maskelynite domain. (B) Modeled ALH 84001 age spectra that would result from several hypothetical heating events ~ 1.15 Ga ago. The models were calculated using the domain distribution parameters and irradiation and laboratory heating schedule for ALH-2, whose corrected age spectrum is shown in grey behind the models.

gest that ALH 84001 was subjected to shock reheating ~ 1.15 Ga ago. Initial maskelynite extractions in aliquots analyzed by Turner et al. (1997) yield ages (as originally reported) of 1494 ± 555 , 1723 ± 490 , and 1898 ± 427 Ma and an aliquot analyzed by Ash et al. (1996) yields an initial age of $\sim 1000 \pm 250$ Ma. These maskelynite age minima further constrain the maximum age of significant $^{40}\text{Ar}^*$ loss. Although one might at first expect that shock heating would preferentially degas maskelynite relative to pyroxene because they degas in that order during monotonically increasing laboratory heating schedules, the opposite might be true in cases of rapid heating to high temperature if the E_a of the two phases were sufficiently different such that their individual Arrhenius arrays intersect at moderately high temperatures. In the following sections, we discuss circumstances under which Ar is capable of diffusing more rapidly from pyroxene than from maskelynite.

5.1.4.1. Brief heating above the diffusive “kinetic crossover” observed on Arrhenius plots. As a result of apparent differences in diffusion kinetics between glass (or plagioclase) and pyroxene (i.e., strongly contrasting E_a), $^{40}\text{Ar}^*$ may diffuse more rapidly from pyroxene under certain high-temperature conditions (i.e., above the temperature at which the extrapolated Ar Arrhenius relationships intersect; the “kinetic crossover”, as recently discussed by Reiners, 2009). In Fig. 6a, we schematically depict the modeled Arrhenius relationships for the domain distribution of ALH-2 that also appears in Fig. 1b. The intersections of lines (denoted with diamonds in Fig. 6a), indicate the temperatures above which Ar diffusivity is higher in a given pyroxene domain (shown in green) relative to a given maskelynite domain (shown in blue). For example, a 1 s heating event at 1400°C will degas 5.8% of maskelynite with $E_a = 138$ kJ/mol and $\ln(D_0/a^2) = 4$, 3.3% of plagioclase with $E_a = 175$ kJ/mol and $\ln(D_0/a^2) = 5.5$, and 100% of OPX with $E_a = 392$ kJ/mol and $\ln(D_0/a^2) = 28.5$. To further illustrate the kinetic crossover concept, we have modeled ALH 84001 age spectra (Fig. 6b) that would result from several hypothetical heating events at 1.15 Ga using the domain distribution parameters (Table 2; Fig. 1b) and laboratory degassing⁵ schedule for ALH-2. Prolonged low temperature heating predicts extensive Ar loss from maskelynite without significant loss from pyroxene (Fig. 6b). Conversely, brief (<1 s) heating at high- T ($>1800^\circ\text{C}$) predicts the observed age spectrum (Fig. 6b). A major constraint on this model is that heating and cooling are required to occur on the timescale of less than a second, which is too brief to encompass thermal equilibration if the entire rock was heated in bulk. Therefore, localized or focused heating is most likely required and may also explain the range of discordance observed between different aliquots.

5.1.4.2. Highly localized shock heating (and pressure). Selective degassing of pyroxene may be enhanced by highly localized shock-heating focused along (sub)grain boundaries, as has been inferred in other cases (e.g., Weiss et al., 2000, 2002a, 2008; Min et al., 2003). Because shock-heating increases with the compressibility of the target material, more energy is deposited in regions where irreversible work is performed (Artemieva and Ivanov, 2004; Fritz et al., 2005). Thus, the closure or reduction of voids, pores, fractures, and grain boundaries within pyroxene may facilitate heating of highly localized regions of pyroxene. Numerical simulations of shock heating in polyphase, porous materials indicate that submicron temperature differentials greater than 800°C can be attained following a 1000 m/s impact (Baer, 2002). These regions should cool rapidly during isentropic pressure release (<0.1 s) and thermal equilibration with surrounding cooler regions (ms to s; Fritz and Greshake, 2009). As maskelynite in ALH 84001 is relatively un-degassed, much of the protolith is required to remain at low temperatures during any post-crystallization shock heating such that following thermal equilibration the temperature of the bulk rock is $<600^\circ\text{C}$. Localized heating must be sufficiently hot to significantly degas pyroxene in less than a second, which requires temperatures above 1400°C (Fig. 6a). Maskelynite was likely subjected to these localized temperature excursions as well, but Ar diffusion in maskelynite is slower than in pyroxene above the kinetic crossover temperatures (Fig. 6a). For this reason, brief, high- T excursions would much more strongly perturb $^{40}\text{Ar}^*$ gradients in pyroxene. The localized nature of these high- T excursions is consistent with the inter-aliquot variations in age discordance.

Because we infer peak shock temperatures of 1400°C or greater, localized areas of plagioclase and pyroxene melt may be generated. In ALH 84001, Bell et al. (1999) identified small regions (~ 0.5 – $2.0\ \mu\text{m}$) of pyroxene glass along pyroxene fractures, between crystalline OPX and CPX, and between crystalline OPX and carbonates. Some of this OPX glass contains inclusions of carbonate rim material with fine-grained (<200 nm) magnetite crystals, which indicates that it formed during or after carbonate formation. In a more recent TEM investigation of OPX glass in ALH 84001, Barber and Scott (2006) state that “the unusual abundance of both OPX glass and fracture zones in ALH 84001 are all consistent with the effects of shear stresses and frictional heating generated by an intense shock. The complete lack of recrystallization and recovery of the deformed OPX in the TEM suggests that heating was localized and rapid, and not global and prolonged.” It appears that sometime after carbonate and maskelynite formation, a shock event very briefly and locally heated pyroxene resulting in substantial $^{40}\text{Ar}^*$ diffusion. This event was probably also responsible for degassing, mobilizing, and intruding small amounts maskelynite in and around pre-existing maskelynite grains (Treiman, 1998; Greenwood and McSween, 2001). Based on the plateau observed in the pyroxene age spectrum of ALH-3 (Fig. 3i), the OPX glass-forming event appears to have occurred 1158 ± 110 Ma ago.

⁵ For all model age spectra we simulated 110 hours of heating at 270°C prior to degassing using the laboratory heating schedule to account for heating associated with irradiation and extraction line bake-out.

Likewise, we propose that Nakhla was subjected to a highly localized heating event at 913 ± 9 Ma, which is the weighted average of pyroxene plateau ages (Fig. 5). Initial plagioclase extractions in NAK-1 and NAK-2 yield minimum ages of 1035 ± 129 and 1110 ± 90 Ma, respectively, and an initial olivine extraction in NAK-3 yields an age of 995 ± 222 Ma, all of which probably reflect Ar loss during this event. Pyroxenes in Nakhla appear to be more significantly degassed than plagioclase and olivine, which likely reflects shock degassing above kinetic crossover temperatures and requires brief, localized heating.

Several petrologic studies provide support for this hypothesis for Nakhla. Lambert (1987) noted that while pyroxene in Nakhla is extensively fractured and contains shock melt veins suggestive of shock pressures between 20 and 40 GPa, plagioclase is not converted to maskelynite and laths of this phase show undulose extinction, typical of shock pressure less than 15–20 GPa. He concludes that, “The polycrystalline character of the interstitial phases, the detail of the mineral grain boundaries, injected intragranular fractures, sulfide droplets. . . may indicate localized melting.” Fritz et al. (2005) note that, “Localized increases in pressure and temperature are a common phenomenon produced when a shock wave propagates through an inhomogeneous medium. . . very localized brecciated areas with a high fracture density are present in the slightly stronger shocked (14–20 GPa) nakhlites, Nakhla and Governador Valadares.” Finally, Malavergne et al. (2001) identified amorphous zones of sulfur-bearing CPX glass. They conclude that, “the apparent differences between calculated shock pressures and temperatures may come from very localized heat dissipation or localized injection of hot shock melts, which would cause, in some areas, strong heating at moderate pressures whereas nearby, a few microns away, would be compressed without much heating. This could also help to understand the presence of melt in very localized areas in Shergotty, Zagami, Nakhla, and Chassigny, whereas no melting is evidenced at the scale of the petrographic thin sections.” In summary, it is probable that Nakhla has experienced post-crystallization, localized pyroxene heating that significantly degassed Ar isotopes.

5.1.5. Other considerations

A few questions regarding our model of localized heating remain to be answered. Depending on the aliquot, 25–100% of the pyroxene-dominated portions of release spectra in ALH 84001 (and Nakhla) appear strongly perturbed to lower ages (Figs. 3,5), which suggests that roughly equivalent sub-volumes of our splits of ALH 84001 and Nakhla were subjected to high temperatures, as pyroxenes comprise >90% of these meteorites by volume. If similar proportions of the Nakhla and ALH 84001 protoliths were heated, subsequent thermal equilibration to temperatures at which Ar does not diffuse from maskelynite (<600 °C) on the timescale of less than a second may be difficult to achieve. However, Xie et al. (2006) found that a 0.588 mm thick melt vein in the Tenham chondrite was heated to >2000 °C for <0.1 s, whereas the surrounding rock only 4 mm away was never heated above the ambient temperature. It is not clear how this model scales to

fractured, mm-sized local environments within ALH 84001 and Nakhla. Experimental studies and numerical models of heat dissipation within maskelynite-bearing pyroxenites during and following shock events would be useful to evaluate our hypothesis of localized heating. Furthermore, numerical models of Ar diffusion in minerals subject to strong temperature gradients may provide insights into the mechanisms of Ar loss during shock events.

Given these uncertainties, localized heating alone may not fully explain the discordance observed in the pyroxene portions of the age spectra. It is possible that our diffusion parameters, determined *in-vacuo* between 400 and 1400 °C, do not accurately quantify Ar diffusivity at temperatures, pressures, and ultra-brief durations relevant to impact events. At high-*T* and high pressure, Ar diffusion may be enhanced in localized regions of pyroxene relative to glass as a result of mineralogical differences, such as the location and prevalence of cleavage and stress planes or the lattice siting of K, and hence $^{40}\text{Ar}^*$. We note in addition that our analysis fails to consider the effects of activation volume (V_a) on the total activation energy for Ar diffusion. Assuming a positive value of V_a , which seems likely for large atoms such as Ar (e.g., Watson and Baxter, 2007) pressure *P* would increase the activation energy E_a by a factor of PV_a . We are unaware of any experimental determinations of V_a for Ar diffusion in the phases of interest here, let alone their variations over the fleeting time frame of impact shock. Experimental studies of Ar diffusion under shock heating conditions and/or at higher temperatures would be useful to further evaluate this mechanism.

It is also feasible that maskelynite was fractured after the last major reheating event, possibly during ejection from Mars or impact on Earth, or during sample preparation. Fracturing may reduce the diffusion length-scale and therefore lead to calculated diffusion coefficients (i.e., D/a^2) that do not directly apply to earlier time. Therefore, age spectra obtained from fragments of once larger grains or heavily fractured grains may not reflect the original $^{40}\text{Ar}^*$ gradient across intact grains. If the diffusive length scale of maskelynite at the time of shock was larger than that sampled in our experiments, then the kinetic crossover temperature would be lower than that observed today (assuming the pyroxene domain distribution is unchanged).

5.2. Low-Temperature Thermochronometry

5.2.1. Post-shock Thermochronometry of ALH 84001

The oldest maskelynite fragments within ALH 84001 yield an age of 4163 ± 35 Ma, which is indistinguishable from Pb–Pb crystallization ages and suggests that (i) maskelynite formed shortly following crystallization or (ii) maskelynite preserves the original crystallization age (i.e., it formed without significant $^{40}\text{Ar}^*$ loss). At 1158 ± 110 Ma, we propose that ALH 84001 was subjected to another shock event. Our data cannot be used to constrain whether or not ALH 84001 was shocked in the intervening time. The younger shock event likely resulted in brief, highly localized, and intense heating (>1400 °C) of pyroxene and maskelynite, resulting in $^{40}\text{Ar}^*$ loss by diffusion. Some pyroxene grains were probably heated in excess of their melting

temperature resulting in the formation of OPX-composition glass. This shock event likely decomposed pre-existing carbonates and degassed and mobilized minor amounts of maskelynite. Much of the observed spread in maskelynite ⁴⁰Ar/³⁹Ar data toward ages younger than 4163 ± 35 Ma is probably due to heterogeneous heating and cooling during this event (Table S1). Localized temperature excursions at 1.16 Ga also offer an explanation for some of the highly scattered U–Th–He ages, which generally range from ~0.1–1.5 Ga (Min and Reiners, 2007), and may be partly responsible for some of the observed spread in Rb–Sr and U–Th–Pb ages (Table S1), as Pb and Sr are mobile at the inferred temperatures (>1400 °C).

ALH-1 forms a plateau over ~95% of the maskelynite portion of the age spectrum (i.e., the first 80% of the total ³⁹Ar released) (Fig. 3a), which indicates that a minimal quantity of ⁴⁰Ar* was lost from maskelynite in this aliquot at all points in time after 4.16 Ga ago. The minor age discordance observed in the first ~5% of the maskelynite portion of the age spectrum may reflect ⁴⁰Ar* loss associated with (i) localized heating during the 1.16 Ga shock event discussed above, (ii) post-shock elevated temperatures following thermal equilibration of the 1.16 Ga shock event (as opposed to brief, localized heating), (iii) elevated temperatures during or following the ~12 Ma ejection event from Mars⁶, or (iv) long duration residence on Mars at elevated ambient temperatures. If we assume all the age discordance observed in the first ~5% of the maskelynite portion of the age spectrum results from ⁴⁰Ar* loss associated with bulk-rock heating (not localized heating), we can constrain the maximum allowable *t*–*T* conditions that the bulk-rock experienced following the 1.16 Ga shock event, following the ~12 Ma ejection event, or as a result of long duration residence at elevated ambient temperatures.

Considering the two shock events (1158 Ma and ~12 Ma), the fractional loss of Ar (*F*) from maskelynite in ALH-1 is related to the integrated maskelynite age (*I*A; 4127 Ma), the true age (*T*A; 4163 Ma), and the shock age (*S*A; 1158 and 12 Ma) according to the following equation.

$$F = \frac{e^{\lambda_*(TA-SA)} - e^{\lambda_*(IA-SA)}}{e^{\lambda_*(TA-SA)} - 1} \quad (5)$$

Assuming plane slab geometry, *F* is related to the dimensionless parameter *Dt/a*² by the following equation⁷:

$$F \equiv \frac{2}{\sqrt{\pi}} \left(\frac{Dt}{a^2} \right)^{\frac{1}{2}} \quad \text{for } F < 0.6 \quad (6)$$

According to the Arrhenius relationship,

$$\frac{D}{a^2} = \frac{D_0}{a^2} e^{\left(\frac{-E_a}{RT}\right)} \quad (7)$$

⁶ Ejection age based on ³⁸Ar_{cos} (Table 1; Turner et al., 1997; Eugster, 1994; Miura et al., 1995).

⁷ In calculating *F*, we conservatively account for ⁴⁰Ar* loss during irradiation and extraction line bake-out heating (i.e., discordance we may not observe in the age spectrum) by adding to *F* the quantity predicted by Eq. 8 for 110 hours of heating at 270 °C (calculated using the diffusion parameters of the smallest domain; see Table 2).

Substituting Eq. 7 into Eq. 6 yields

$$F \equiv \frac{2}{\sqrt{\pi}} \left(t \times \frac{D_0}{a^2} e^{\left(\frac{-E_a}{RT}\right)} \right)^{\frac{1}{2}} \quad (8)$$

Therefore, after substituting *D*₀/*a*² and *E*_a for the smallest (least retentive) maskelynite domain into Eq. 8, we have an expression for *F* as a function of *T* and *t*, which represent maximum possible bulk-rock *t*–*T* conditions following the shock event of interest. Because we assume that no Ar was lost as a result of localized temperature excursions during the shock event and we neglect argon loss associated with other shock events or elevated ambient temperatures, this analysis represents a conservative upper bound on the post-shock *t*–*T* conditions for a given event and the true conditions were likely shorter and colder. The results of our modeling (Fig. 7a) suggest that the maximum permissible, mean thermal conditions for ALH 84001 following the 1.16 Ga shock event were between (i) ~80 °C for a duration of 10 Ma (e.g., prolonged cooling at depth beneath an ejecta blanket) and (ii) ~330 °C for several days (e.g., brief heating near the surface or within a polymict breccia). The maximum permissible, mean thermal conditions for ALH 84001 following the ~12 Ma ejection event were between (i) ~75 °C for a duration of 10 Ma and (ii) ~320 °C for several days. Again, since these calculations do not consider any other sources of heat, they represent strong upper bounds on mean temperatures over a given time period. Because other heat sources are likely, the bulk-rock *t*–*T* conditions were probably cooler than these maximum permissible constraints. We will return to constraints on long duration residence at elevated surface temperatures in the following section.

5.2.2. Nakhla Thermochronometry

⁴⁰Ar/³⁹Ar isochron ages from Nakhla plagioclase define a crystallization age of 1332 ± 24 Ma (Table 3), which is statistically indistinguishable from previous ⁴⁰Ar/³⁹Ar results obtained by other investigators (Table S1). At 913 ± 9 Ma, we suggest that Nakhla was subjected to a shock event that resulted in brief, highly localized, and intense heating of pyroxene. This shock event likely fractured pyroxene and, in isolated locations, caused heating in excess of its melting temperature, resulting in the formation of pyroxene glass. Localized pyroxene heating may explain some of the observed spread toward post-crystallization Rb–Sr and U–Th–Pb ages (Table S1). As discussed above, if we assume all the age discordance observed in the first 10% of the NAK-2 age spectrum results from ⁴⁰Ar* loss associated with post-shock elevated temperatures following thermal equilibration (as opposed to brief, localized heating), we can constrain the maximum permissible bulk-rock *t*–*T* conditions Nakhla experienced following the 913 Ma shock event or the ~9 Ma ejection event. The results of our modeling (Fig. 7b) suggest that the maximum permissible, mean thermal conditions for Nakhla following the 913 Ma shock event were between (i) ~120 °C for a duration of 10 Ma (e.g., prolonged cooling at depth beneath an ejecta blanket) and (ii) ~355 °C for several days (e.g., brief heating near the surface or within a polymict breccia). The maximum permissible, mean thermal conditions for

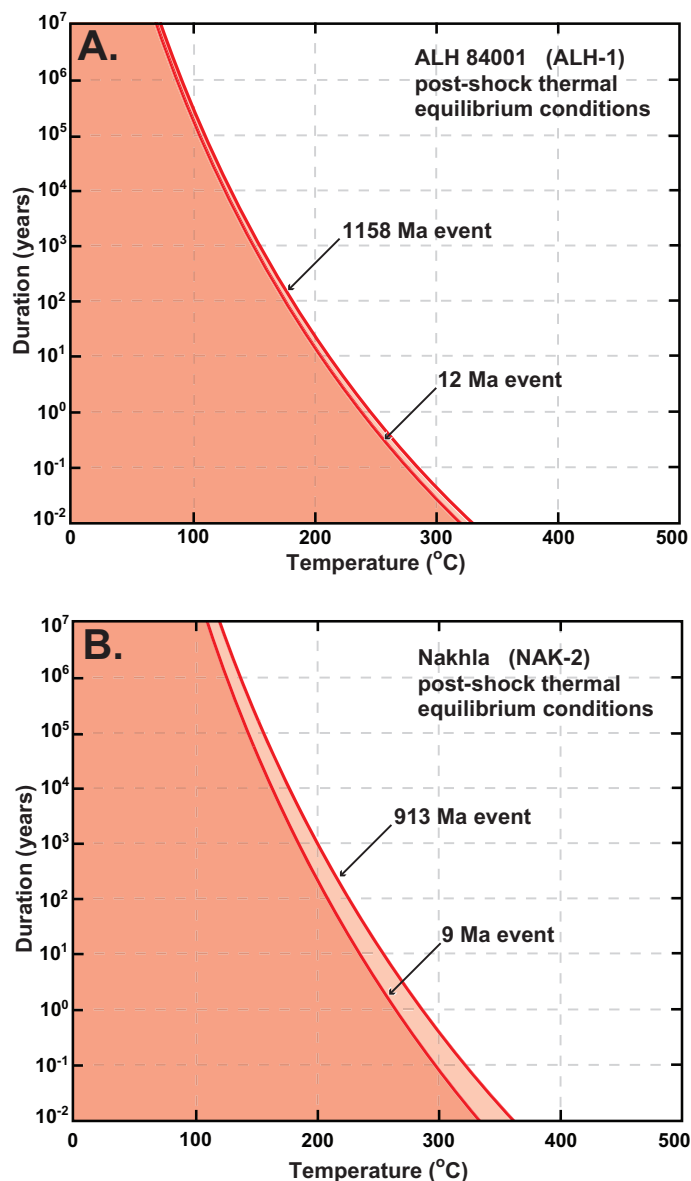


Fig. 7. $^{40}\text{Ar}/^{39}\text{Ar}$ constraints on post-shock t – T conditions immediately following thermal equilibration for events 1158 Ma and 12 Ma ago (ALH 84001) and 913 and 9 Ma ago (Nakhla) (see text for calculations and discussion). Red areas represent permissible solutions.

Nakhla following the ~ 9 Ma ejection event were between (i) $\sim 110^\circ\text{C}$ for a duration of 10 Ma and (ii) $\sim 330^\circ\text{C}$ for several days.

5.2.3. MIL 03346 Thermochronometry

Plagioclase and pyroxene in MIL 03346 yield $^{40}\text{Ar}/^{39}\text{Ar}$ isochron ages of 1367 ± 19 Ma and 1333 ± 9 Ma, respectively, and a weighted average age of 1339 ± 9 Ma. Park et al. (2009) obtained similar ages of 1370 ± 80 Ma and 1330 ± 50 Ma for plagioclase and pyroxene, respectively. We suggest that pyroxenes in MIL 03346, unlike those in Nakhla and ALH 84001, have not been subjected to intense, localized shock-heating, consistent with the observation that Sm–Nd, Rb–Sr, Pb–Pb, and Lu–Hf chronometers yield indistinguishable ages (Table S1).

5.3. Constraints on long-duration thermal state

As shown previously, $^{40}\text{Ar}/^{39}\text{Ar}$ thermochronometry of low retentivity phases within Martian meteorites can also constrain the long-duration thermal conditions of precursor rocks prior to ejection and transport to Earth (Weiss et al., 2002b; Shuster and Weiss, 2005). For this purpose, the least Ar-retentive phases exhibiting the least diffusive loss of $^{40}\text{Ar}^*$ are most useful for constraining the upper bound. To calculate this bound, we therefore assume that all apparent diffusive loss of $^{40}\text{Ar}^*$ occurred during simultaneous radiogenic production at a constant temperature over a duration defined by each sample's plateau age, and that no loss occurred during: (i) the late-stage impact events discussed above, (ii) the impact events which ejected the rocks

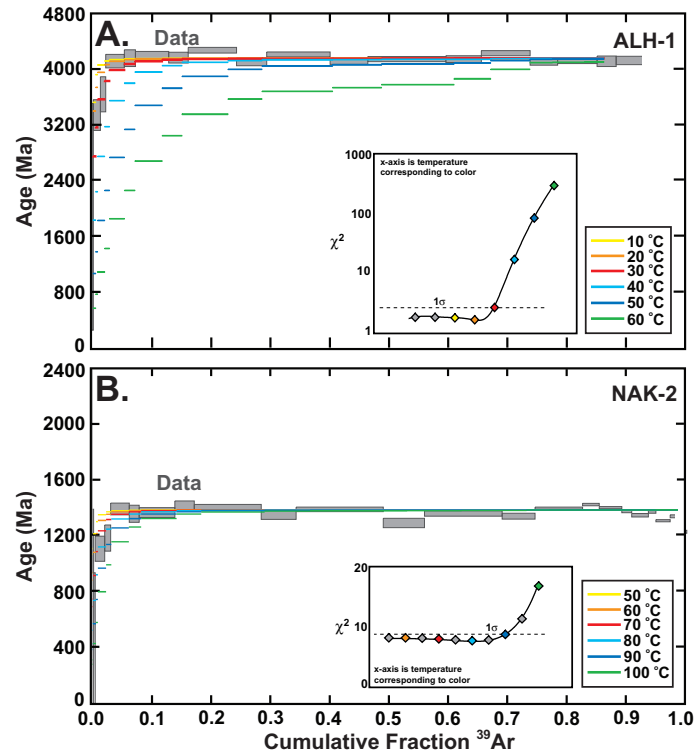


Fig. 8. Upper bounds on long-duration residence temperatures prior to ejection from Mars for ALH-1 and NAK-2 using Ar diffusion parameters shown in Table 2. Models of simultaneous $^{40}\text{Ar}^*$ accumulation and diffusion are shown for different constant temperatures held for all time since 4.16 Ga ago (ALH-1) and 1.35 Ga ago (NAK-2); the observed $^{40}\text{Ar}/^{39}\text{Ar}$ age spectra are shown in grey. Pyroxene extractions have been removed from the whole-rock age spectra (i.e., the data have been normalized such that maskelynite or plagioclase comprises 100% of the total ^{39}Ar). Also shown are the reduced chi squared (χ^2_v) fit statistics for various model residence temperatures. The best-fit upper bound for each sample is identified at the minimum χ^2_v . The asymmetric errors in T (dashed line) are estimated from the values calculated at fixed distances (typically +1.2 in χ^2_v) above the best-fit solution. Curves are polynomial fits to the χ^2_v values used to identify the minimum. Data colors in the χ^2_v inset correspond to temperatures shown in models.

from the Martian surface ~ 10 – 13 and ~ 8 – 10 Ma ago [for ALH 84001 (based on $^{38}\text{Ar}_{\text{cos}}$; Table 1; Turner et al., 1997; Eugster, 1994; Miura et al., 1995) and Nakhla (based on $^{38}\text{Ar}_{\text{cos}}$; Table 1), respectively], (iii) transit through Earth's atmosphere, and (iv) any subsequent heating while on Earth. Although the pre-ejection depths of ALH 84001 and Nakhla are not well known, long-duration thermal modeling constrains maximum average near-surface temperatures because ambient temperatures usually increase with depth.

Using the apparent Ar diffusion kinetics of maskelynite in ALH-1 and plagioclase in NAK-2 (Table 2), we find that the source rock of ALH84001 resided at a maximum mean temperature of $22^{+8}_{-\infty}$ °C over the ~ 4.16 Ga, while the source rock of Nakhla resided at a maximum of $81^{+9}_{-\infty}$ °C since ~ 1.35 Ga ago (Fig. 8). Our results are consistent with, but less restrictive than, those previously inferred by Shuster and Weiss (2005) using the $^{40}\text{Ar}/^{39}\text{Ar}$ datasets of Bogard and Garrison (1999) and Swindle and Olson (2004), and require that the samples experienced relatively low temperatures for most of their residence on Mars. If any $^{40}\text{Ar}^*$ diffused from maskelynite and plagioclase during the shock heating events at ~ 1.15 and ~ 0.9 Ga ago (discussed above in Section 5.1.4) for ALH 84001 and Nakhla, respectively,

or during ejection or transit to Earth, the long-duration thermal state is required to be colder.

5.4. Implications for NRM acquisition and overprints

Observations of intense magnetic anomalies in the Martian crust by the Mars Global Surveyor (MGS) indicate that Mars had a core dynamo in the Noachian epoch. Paleomagnetic studies of ALH 84001 (Kirschvink et al., 1997; Collinson, 1997; Weiss et al., 2000, 2002a, 2002b, 2008; Antretter et al., 2003; Gattacceca and Rochette, 2004) have found that the meteorite contains an unusual, heterogeneously oriented remanent magnetization that varies in direction at sub-centimeter scales. $^{40}\text{Ar}/^{39}\text{Ar}$ data in this and previous studies suggest that much of the characteristic NRM in ALH 84001 was likely acquired as a thermoremanence on Mars during a shock event that strongly heated the meteorite at ~ 4 Ga. Weiss et al. (2000, 2002a, 2002b, 2008) speculated that the heterogeneous pattern of magnetization originated as a result of one or more post-4 Ga shock events that heterogeneously heated the rock [see Auxiliary Text Section 3.0 of Weiss et al. (2008) for details]. However, a weakness of this explanation was that beyond the

heterogeneous magnetization pattern, there was little other quantitative evidence in support of localized high-temperature events. The discovery in the present study of localized, short-lived, high-temperature excursions in ALH 84001 (whose temperatures well exceed the 320 °C and 580 °C Curie point of pyrrhotite and magnetite, the ferromagnetic minerals in the meteorite) now provides strong support for this hypothesis. It further dates the NRM partial overprinting event to ~ 1.15 Ga. This is well after the lifetime of the Martian dynamo, which is thought to have disappeared by the early Hesperian epoch (before 3.9 Ga). The latter conclusion was based on MGS maps of crustal magnetization and the age of the associated terranes (Lillis et al., 2008; Hood et al., 2010). Either the latter conclusion is incorrect (potentially due to small-scale magnetization not resolved by MGS) or else ALH 84001 was overprinted by a crustal remanent magnetization field. As discussed by Weiss et al. (2002a), crustal fields observed today are certainly strong enough to have remagnetized the meteorite.

6. CONCLUSIONS

$^{40}\text{Ar}/^{39}\text{Ar}$ isochrons from Martian meteorites Nakhla and MIL 03346 yield ages of 1332 ± 24 and 1339 ± 8 Ma, respectively, which we interpret to date crystallization. The oldest maskelynite fragments within ALH 84001 yield an age of 4163 ± 35 Ma, which is indistinguishable from Pb–Pb crystallization ages (Bouvier et al., 2009a) and indicates that (i) maskelynite formed shortly following crystallization or (ii) maskelynite preserves the original crystallization age (i.e., it formed without significant Ar loss). The high precision of this result arises from clear resolution of a reproducible trapped $^{40}\text{Ar}/^{36}\text{Ar}$ component in maskelynite in ALH 84001 ($^{40}\text{Ar}/^{36}\text{Ar} = 632 \pm 90$). The maskelynite age (4163 ± 35 Ma) predates the Late Heavy Bombardment (e.g., Tera et al., 1974) and likely represents the time at which the original NRM component observed in ALH 84001 was acquired.

We suggest that the high- T release patterns observed in ALH 84001 and Nakhla $^{40}\text{Ar}/^{39}\text{Ar}$ age spectra reflect diffusive $^{40}\text{Ar}^*$ distributions within considerably degassed pyroxene grains, rather than recoil redistribution of ^{39}Ar . Discordance observed in ALH 84001 and Nakhla $^{40}\text{Ar}/^{39}\text{Ar}$ age spectra can be explained by highly localized, intense heating for brief durations during shock events at 1158 ± 110 and 913 ± 9 Ma, respectively. A shock and impact origin of high- T age discordance observed in whole-rock $^{40}\text{Ar}/^{39}\text{Ar}$ age spectra may explain its frequent appearance in extraterrestrial samples, as well as the paucity of similar observations in terrestrial samples. MIL 03346 appears not have experienced significant shock heating since it crystallized.

For ALH 84001, the late shock event is probably responsible for fracturing and decomposing areas within carbonates, mobilizing minor amounts of maskelynite, and generating pyroxene melts. Much of the observed spread in maskelynite $^{40}\text{Ar}/^{39}\text{Ar}$ data toward apparent plateau ages younger than 4163 ± 35 Ma (Table 2; Turner et al., 1997; Bogard and Garrison, 1999) is likely due

to heterogeneous heating during this event. Inferred peak temperatures (>1400 °C) are sufficient to mobilize Sr and Pb and may explain some of the observed spread toward post-crystallization ages obtained from these chronometers. Localized shock heating in ALH 84001 provides strong support for the proposal that the heterogeneous pattern of magnetization observed in this meteorite was derived by localized thermal remagnetization immediately following a shock event. Given that heterogeneously oriented NRM is commonly observed in many shocked meteorites, this may in fact have broad implications for the interpretation of extraterrestrial magnetism in general.

ACKNOWLEDGEMENTS

We are grateful to Tim Becker for his expertise and laboratory assistance and to Photon Machines for collaborative development of laser heating hardware. The authors acknowledge financial support from the NASA Mars Fundamental Research program (grant MFRP05-0108 to B.P.W. and D.L.S.), The NSF Petrology and Geochemistry program (grant EAR-0838572 to P.R.R. and D.L.S.), The NSF Major Research Instrumentation program (grant EAR-0618219 to D.L.S. and P.R.R.), and the Ann and Gordon Getty Foundation. W.S. Cassata was supported by a National Science Foundation Graduate Research Fellowship. Rich Ketcham, Peter Reiners, and two anonymous reviewers are thanked for their constructive reviews of the manuscript.

APPENDIX A. SUPPLEMENTARY DATA

Supplementary data associated with this article can be found, in the online version, at [doi:10.1016/j.gca.2010.08.027](https://doi.org/10.1016/j.gca.2010.08.027).

REFERENCES

- Anand, M., Williams, C.T., Russell, S.S., Jones, G., James, S., Grady, M.M., 2005 Petrology and geochemistry of Nakhla MIL 03346: a new Martian meteorite from Antarctica, Proc. 36th. Lunar Planet. Sci. Conf., #1639 (abstr.).
- Antretter M., Fuller M., Scott E., Jackson M., Moskowitz B. and Solheid P. (2003) Paleomagnetic record of Martian meteorite ALH 84001. *J. Geophys. Res.* **108**, 5049, doi:10.1029/2002JE001979.
- Artemieva N. and Ivanov B. A. (2004) Launch of Martian meteorites in oblique impacts. *Icarus* **171**, 84–101.
- Ash R. D., Knott S. F. and Turner G. (1996) A 4-Gyr shock age for a Martian meteorite and implications for the cratering history of Mars. *Nature* **380**, 57–59.
- Baer M. R. (2002) Modeling heterogeneous energetic materials at the mesoscale. *Thermochim. Acta* **384**, 351–367.
- Barber D. J. and Scott E. R. D. (2006) Shock and thermal history of Martian meteorite Allan Hills 84001 from transmission electron microscopy. *Meteorit. Planet. Sci.* **41**, 643–662.
- Bell, M.S., Thomas-Krepta, K.L., Wentworth, S.J., McKay, D.S., 1999, Microanalysis of pyroxene, feldspar, and silica glass in Allan Hills 84001. *Meteoritics and Planetary Science* **34**, A10–A11 (abstr.).
- Bogard D. D. (1995) Impact ages of meteorites – a synthesis. *Meteoritics* **30**(3), 244–268.

- Bogard D. D. and Garrison D. H. (1999) Argon-39-argon-40 "Ages" and trapped Argon in Martian Shergottites, Chassigny, and Allan Hills 84001. *Meteorit. Planet. Sci.* **34**, 451–473.
- Bogard D. D. and Husain L. (1977) A new 1.3 Aeon-Young Achondrite. *Geophys. Res. Lett.* **4**, 69–71.
- Borg L. E., Connelly J. N., Nyquist L. E., Shih C.-Y., Wiesmann H. and Reese Y. (1999) The age of the carbonates in Martian Meteorite ALH84001. *Science* **286**, 90–94.
- Bouvier, A., Blichert-Toft, J., Vervoort, J.D., Albarède, F., 2007, The Conundrum of the Age of Shergottites, *Proc. 38th Lunar Planet. Sci. Conf.*, #1338 (abstr.).
- Bouvier A., Blichert-Toft J. and Albarède F. (2009a) Martian meteorite chronology and the evolution of the interior of Mars. *Earth Planet Sci. Lett.* **280**, 285–295.
- Bouvier, A., Blichert-Toft, J., and Albarède, F., 2009b, Martian Meteorite Chronology and Effects of Impact Metamorphism, *Eos*, Vol. 90, Number 52, Fall Meet. Suppl. MR12A-04 (abstr.).
- Bunch T. E. and Reid A. M. (1975) The nakhlites Part I. petrography and mineral chemistry. *Meteoritics* **10**, 303–315.
- Cassata W. S., Renne P. R. and Shuster D. L. (2009) Argon diffusion in plagioclase and implications for thermochronometry: a case study from the bushveld complex, South Africa. *Geochim. Cosmochim. Acta* **73**, 6600–6612.
- Collinson D. W. (1997) Magnetic properties of Martian meteorites - Implications for an ancient Martian magnetic field. *Meteorit. Planet. Sci.* **32**, 803–811.
- Crank J. (1975) *The mathematics of diffusion*, 2d ed. Oxford, Clarendon Press.
- Day J. M. D., Taylor L. A., Floss C. and McSween H. Y. (2006) Petrology and chemistry of MIL 03346 and its significance in understanding the petrogenesis of nakhlites on Mars. *Meteorit. Planet. Sci.* **41**, 581–606.
- Eugster O. (1994) Orthopyroxenite ALH84001: Ejection from Mars (?) 15 Ma. *Meteoritics* **29**, 464.
- Eugster O. and Michel T. (1995) Common asteroid break-up events of eucrites, diogenites, and howardites and cosmic-ray production rates for noble gases in achondrites. *Geochim. Cosmochim. Acta* **59**, 177–199.
- Fechtig H. and Kalbitzer S. (1966) The diffusion of argon in potassium bearing solids. In *Potassium-Argon Dating* (eds. O. A. Schaeffer and J. Zahringer). Springer, pp. 68–106.
- Friedman-Lentz R. C., Taylor G. J. and Treiman A. H. (1999) Formation of a martian pyroxenite: a comparative study of the nakhlite meteorites and Theo's flow. *Meteorit. Planet. Sci.* **34**, 919–932.
- Fritz J., Artemieva N. and Greshake A. (2005) Ejection of Martian meteorites. *Meteorit. Planet. Sci.* **40**, 1393–1411.
- Fritz, J., and Greshake, A., 2009, Petrographic constraints on shock induced P/T conditions in Shergottites. *Proc. 40th Lunar Planet. Sci. Conf.*, #1581 (abstr.).
- Gale N. H., Arden J. W. and Hutchison R. (1975) The Chronology of the nakhla achondritic meteorite. *Earth Planet Sci. Lett.* **26**, 195–206.
- Ganapathy R. and Anders E. (1969) Ages of calcium-rich achondrites – ii howardites, nakhlites, and the angra dos reis angrite. *Geochim. Cosmochim. Acta* **33**, 775–787.
- Gattacceca J. and Rochette P. (2004) Toward a robust normalized magnetic paleointensity method applied to meteorites. *Earth Planet Sci. Lett.* **227**, 377–393.
- Greenwood J. P. and McSween H. Y. (2001) Petrogenesis of Allan Hills 84001: Constraints from impact-melted feldspathic and silica glasses. *Meteorit. Planet. Sci.* **36**, 43–61.
- Hood L. L., Harrison K. P., Langlais B., Lillis R. J., Poulet F. and Williams D. A. (2010) Magnetic anomalies near Apollinaris Patera and the Medusae Fossae Formation in Lucus Planum, Mars. *Icarus* **208**, 118–131.
- Huneke, J. C., and Smith, S. P., 1976, The realities of recoil out of small grains and anomalous age patterns in ^{39}Ar - ^{40}Ar dating, *Proc. 7th Lunar Planet. Sci. Conf.*, 1987–2008 (abstr.).
- Ilg S., Jessberger E. K. and El Goresy A. (1997) Argon-40/argon-39 laser extraction dating of individual maskelynites in snc pyroxenite Allan Hills 84001. *Meteorit. Planet. Sci.* **32**, A65 (abstr.).
- Jagoutz E., Sorowka A., Vogel J. D. and Wanke H. (1994) ALH 84001: alien or progenitor of the SNC family? *Meteoritics* **29**, 478–479.
- Jagoutz, E., Bowring, S., Jotter, R., Dreibus, G., 2009, New U-Th-Pb Data On SNC Meteorite ALH 84001, *Proc. 40th Lunar Planet. Sci. Conf.*, #1662 (abstr.).
- Jourdan F. and Renne P. R. (2007) Age calibration of the fish canyon sanidine $^{40}\text{Ar}/^{39}\text{Ar}$ dating standard using primary K-Ar standards. *Geochim. Cosmochim. Acta* **71**, 387–402.
- Jourdan F., Matzel J. P. and Renne P. R. (2007) ^{39}Ar and ^{37}Ar recoil ejection during neutron irradiation of sanidine and plagioclase. *Geochim. Cosmochim. Acta* **71**, 2791–2808. doi:10.1016/j.gca.2006.06.606.
- Kirschvink J. L., Maine A. T. and Vali H. (1997) Paleomagnetic evidence of a low-temperature origin of carbonate in the Martian meteorite ALH84001. *Science* **275**, 1629–1633.
- Knott, S.F., Ash, R.D., Turner, G., 1996, 40Ar-39Ar Dating of ALH84001: Evidence for the Early Bombardment of Mars, *Proc. 26th Lunar Planet. Sci. Conf.*, 765–766 (abstr.).
- Kunz J., Falter M. and Jessberger E. K. (1997) Shocked meteorites: Argon-40-argon-39 evidence for multiple impacts. *Meteorit. Planet. Sci.* **32**, 647–670.
- Lambert, P., 1987, SNC Meteorites: The metamorphic record, *Proc. 18th Lunar Planet. Sci. Conf.*, p. 529 (abstr.).
- Lapen T. J., Richter M., Brandon A. D., Debaille V., Beard B. L., Shafer J. T. and Peslier A. H. (2010) A younger age for ALH 84001 and its geochemical link to Shergottite sources in Mars. *Science* **328**, 347–351.
- Levine J., Renne P. R. and Muller R. A. (2007) Solar and Cosmogenic Argon in Dated Lunar Impact Spherules. *Geochim. Cosmochim. Acta* **71**, 1624–1635.
- Lillis R. J., Frey H. V. and Manga M. (2008) Rapid decrease in Martian crustal magnetization in the Noachian era: Implications for the dynamo and climate of early Mars. *Geophys. Res. Lett.* **35**, L14203, doi:10.1029/2008GL034338.
- Lovera O. M., Richter F. M. and Harrison T. M. (1991) Diffusion domains determined by ^{39}Ar release during step heating. *J. Geophys. Res.* **96**, 2057–2069.
- Malaverge V., Guyot F., Benzerara K. and Martinez I. (2001) Description of new shock-induced phases in the Shergotty, Zagami, Nakhla and Chassigny meteorites. *Meteorit. Planet. Sci.* **36**, 1297–1305.
- Mason B., MacPherson G. J., Score R., Martinez R., Satterwhite C., Schwarz C. Gooding J. L. (1992) Descriptions of Stony Meteorites. In *Field and laboratory investigations of Antarctic meteorites collected by the United States expeditions 1985–1987* (eds. Marvin and MacPherson, Smithsonian) Contrib. Earth Sci. Washington, DC, 30, pp. 17–35.
- Min K. and Reiners P. W. (2007) High-Temperature Mars-to-Earth Transfer of Meteorite ALH84001. *Earth Planet Sci. Lett.* **260**, 72–85.
- Min K., Farley K. A., Renne P. R. and Marti K. (2003) Single grain (U-Th)/He ages from phosphates in Acapulco meteorite and implications for thermal history. *Earth Planet Sci. Lett.* **209**, 323–336.
- Mittlefehldt D. W. (1994) ALH84001, A Cumulate Orthopyroxenite Member of the Martian Meteorite Clan. *Meteoritics* **29**, 214–221.

- Mittlefehldt D. W. (1997) Macroscopic description of Allan Hills 84001 and the relative timing of events in its history. *Meteorit. Planet. Sci.* **32**, A93 (abstr.).
- Miura Y. N., Nagao K., Sugiura N., Sagawa H. and Matsubara K. (1995) Orthopyroxenite ALH84001 and shergottite ALH77005: Additional evidence for a martian origin from noble gases. *Geochim. Cosmochim. Acta* **59**, 2105–2113.
- Murty, S.V.S., Mahajan, R.R., Goswami, J.N., Sinha, N., 2005, Noble Gases and Nuclear Tracks in the Nakhilite MIL 03346, *Proc. 36th Lunar Planet. Sci. Conf.*, #1280 (abstr.).
- Nakamura N., Unruh D. M., Tatsumoto M. and Hutchison R. (1982) Origin and evolution of the nakhla meteorite inferred from the Sm–Nd and U–Pb systematics and Re, Ba, Sr, Rb abundances. *Geochim. Cosmochim. Acta* **46**, 1555–1573.
- Nyquist, L.E., Bansal, B.M., Wiesmann, H., Shih, C.-Y., 1995, “Martians” young and old: Zagami and ALH84001, *Proc. 26th Lunar Planet. Sci. Conf.*, 1065–1066 (abstr.).
- Nyquist L. E., Bogard D. D., Shih C., Greshake A., Stöfler D. and Eugster O. (2001) Ages and geologic histories of martian meteorites. *Space Sci. Rev.* **96**, 105–164.
- Papanastassiou D. A. and Wasserburg G. J. (1974) Evidence for Late Formation and Young Metamorphism in the Achondrite Nakhla. *Geophys. Res. Lett.* **1**, 23–26.
- Park J., Garrison D. H. and Bogard D. D. (2009) ^{39}Ar – ^{40}Ar ages of martian nakhlites. *Geochim. Cosmochim. Acta* **73**, 2177–2189.
- Podosek F. A. (1973) Thermal history of the nakhlites by the ^{40}Ar – ^{39}Ar method. *Earth Planet Sci. Lett.* **19**, 135–144.
- Reiners P. (2009) Nonmonotonic thermal histories and contrasting kinetics of multiple thermochronometers. *Geochim. Cosmochim. Acta* **73**, 3612–3629.
- Renne P. R., Swisher C. C., Deino A. L., Karner D. B., Owens T. L. and DePaolo D. J. (1998) Inter-calibration of standards, absolute ages and uncertainties in $^{40}\text{Ar}/^{39}\text{Ar}$ dating. *Chem. Geol.* **145**, 117–152.
- Renne P. R., Knight K., Nomade S., Leung K. and Lou T. (2005) Application of deuteron-deuteron (D–D) fusion neutrons to $^{40}\text{Ar}/^{39}\text{Ar}$ geochronology. *Appl. Radiat. Isot.* **62**, 25–32.
- Renne P. R., Cassata W. S. and Morgan L. (2009) The isotopic composition of atmospheric argon and $^{40}\text{Ar}/^{39}\text{Ar}$ geochronology: Time for a change? *Quat. Geochronol.* **4**, 288–298.
- Renne, P.R., Mundil, R., Balco, G., Min, K., and Ludwig, K.R., 2010. Joint determination of ^{40}K decay constants and $^{40}\text{Ar}^*/^{40}\text{K}$ for the Fish Canyon sanidine standard, and improved accuracy for $^{40}\text{Ar}/^{39}\text{Ar}$ geochronology: *Geochim. Cosmochim. Acta*, **74**, 5349–5367.
- Sautter V., Jambon A. and Boudouma O. (2006) Cl-amphibole in the nakhlite MIL 03346: Evidence for sediment contamination in a Martian meteorite. *Earth Planet Sci. Lett.* **252**, 45–55.
- Shih C.-Y., Nyquist, L.E., and Reese, Y., 2006, Rb–Sr and Sm–Nd isotopic studies of Antarctic nakhlite MIL 03346, *Proc. 37th Lunar Planet. Sci. Conf.*, #1701 (abstr.).
- Shuster D. L. and Farley K. A. (2009) The influence of artificial radiation damage and thermal annealing on helium diffusion kinetics in apatite. *Geochim. Cosmochim. Acta* **73**, 183–196.
- Shuster D. L. and Weiss B. P. (2005) Martian surface paleotemperatures from thermochronology of meteorites. *Science* **309**(5734), 594–597.
- Shuster D. L., Balco G., Cassata W. S., Fernandes V. A., Garrick-Bethell I. and Weiss B. P. (2010) A record of impacts preserved in the lunar regolith. *Earth Planet Sci. Lett.* **290**(1–2), 155–165.
- Steiger R. H. and Jäger E. (1977) Subcommission on geochronology: convention on the use of decay constants in geo- and cosmochronology. *Earth Planet. Sci. Lett.* **36**, 359–362.
- Stopar J. D., Lawrence S. J., Lentz R. C. F. and Taylor G. J., 2005, Preliminary analysis of nakhlite MIL 03346, with a focus on secondary alteration, *Proc. 36th Lunar Planet. Sci. Conf.*, #1547 (abstr.).
- Swindle T. D. and Olson E. K. (2004) ^{40}Ar – ^{39}Ar studies of whole rock nakhlites: evidence for the timing of formation and aqueous alteration on Mars. *Meteorit. Planet. Sci.* **39**, 755–766.
- Tera F., Papanastassiou D. A. and Wasserburg G. J. (1974) Isotopic evidence for a terminal lunar cataclysm. *Earth Planet. Sci. Lett.* **22**(1), 1–21.
- Terada K., Monde T. and Sano Y. (2003) Ion microprobe U–Th–Pb dating of phosphates in martian meteorite ALH 84001. *Meteorit. Planet. Sci.* **38**, 1697–1703.
- Treiman A. H. (1995) A petrographic history of martian meteorite ALH84001: two shocks and an ancient age. *Meteoritics* **30**, 294–302.
- Treiman A. H. (1998) The History of ALH84001 Revised: Multiple Shock Events. *Meteorit. Planet. Sci.* **33**, 753–764.
- Treiman A. H. (2003) Submicron magnetite grains and carbon compounds in Martian meteorite ALH 84001: Inorganic, abiotic formation by shock and thermal metamorphism. *Astrobiology* **3**, 369–392.
- Trieloff M., Jessberger E., Herrwerth I., Hopp J., Fieni Ghelis., Bourot-Denise P. M. and Pellas M. (1998) Structure and thermal history of the H-chondrite parent asteroid revealed by thermochronometry. *Nature* **422**, 502–506.
- Turner G. (1971) ^{40}Ar – ^{39}Ar ages from lunar maria. *Earth Planet. Sci. Lett.* **11**(3), 169–191.
- Turner G., Miller J. A. and Grasty R. L. (1966) The thermal history of the Bruderheim meteorite. *Earth Planet. Sci. Lett.* **1**(4), 155–157.
- Turner, G., Cadogan, P.H., 1974, Possible effects of ^{39}Ar recoil in ^{40}Ar – ^{39}Ar dating, *Proc. 5th Lunar Planet. Sci. Conf.*, 1601–1615 (abstr.).
- Turner G., Knott S. F., Ash R. D. and Gilmour J. D. (1997) Ar–Ar Chronology of the Martian Meteorite ALH84001: Evidence for the Timing of the Early Bombardment of Mars. *Geochim. Cosmochim. Acta* **61**, 3835–3850.
- Wadhwa M. and Lugmair G. W. (1996) The formation age of carbonates in ALH84001. *Meteorit. Planet. Sci.* **31**, A145.
- Wang S., McDougall I., Tetley N. and Harrison T. (1980) $^{40}\text{Ar}/^{39}\text{Ar}$ age and thermal history of the Kirin chondrite. *Earth Planet. Sci. Lett.* **49**, 117–131.
- Watson E. B. and Baxter E. F. (2007) Diffusion in solid-earth systems. *Earth Planet. Sci. Lett.* **253**, 307–327.
- Weiss B. P., Kirschvink J. L., Baudenbacher F. J., Vali H., Peters N. T., Macdonald F. A. and Wikswo J. P. (2000) A low temperature transfer of ALH84001 from mars to earth. *Science* **290**, 791–795.
- Weiss B. P., Vali H., Baudenbacher F. J., Kirschvink J. L., Stewart S. T. and Shuster D. L. (2002a) Records of an ancient Martian magnetic field in ALH84001. *Earth Planet. Sci. Lett.* **201**, 449–463.
- Weiss B. P., Shuster D. L. and Stewart S. T. (2002b) Temperatures on Mars from $^{40}\text{Ar}/^{39}\text{Ar}$ thermochronology of ALH84001. *Earth Planet. Sci. Lett.* **201**(3–4), 465–472.
- Weiss B. P., Fong L. E., Vali H., Lima E. A. and Baudenbacher F. J. (2008) Paleointensity of the ancient Martian magnetic field. *Geophys. Res. Lett.* **35**, L23207, doi: 10.1029/2008GL035585.
- Wieler R. (2002) Cosmic-ray produced noble gases in meteorites. *Rev. Min. Geochem.* **47**, 125–170.
- Xie Z., Sharp T. G. and DeCarlie P. S. (2006) High-pressure phases in a shock-induced melt vein of the Tenham L6 chondrite: Constraints on shock pressure and duration, *Geochim. Cosmochim. Acta* **70**, 504–515.

Supplementary Files for:

**Evidence for shock heating and constraints on Martian surface temperatures
revealed by $^{40}\text{Ar}/^{39}\text{Ar}$ thermochronometry of Martian meteorites**

William S. Cassata^{1,2,*}, David L. Shuster², Paul R. Renne^{1,2}, Benjamin P. Weiss³

1. Department of Earth and Planetary Sciences, University of California - Berkeley, 307 McCone Hall #4767, Berkeley, CA 94720-4767, USA (cassata@berkeley.edu)
2. Berkeley Geochronology Center, 2455 Ridge Road, Berkeley, CA 94709, USA (prenne@bgc.org, dshuster@bgc.org)
3. Department of Earth, Atmospheric, and Planetary Sciences, Massachusetts Institute of Technology, 77 Massachusetts Avenue, Cambridge, MA 02139, USA (bpweiss@mit.edu)

* Corresponding author

Contents:

Supplementary Figures

Fig. S1: Illustration of procedure used to identify cosmogenic, trapped, and Cl-derived Ar isotopes

Fig. S2: Alternative MDD-type models fit to the ALH-1 Arrhenius plot.

Fig. S3: Apparent age spectra for NAK-3 and NAK-4.

Supplementary Tables

Table S1: Summary of published geochronometry for ALH 84001, Nakhla, and MIL 03346.

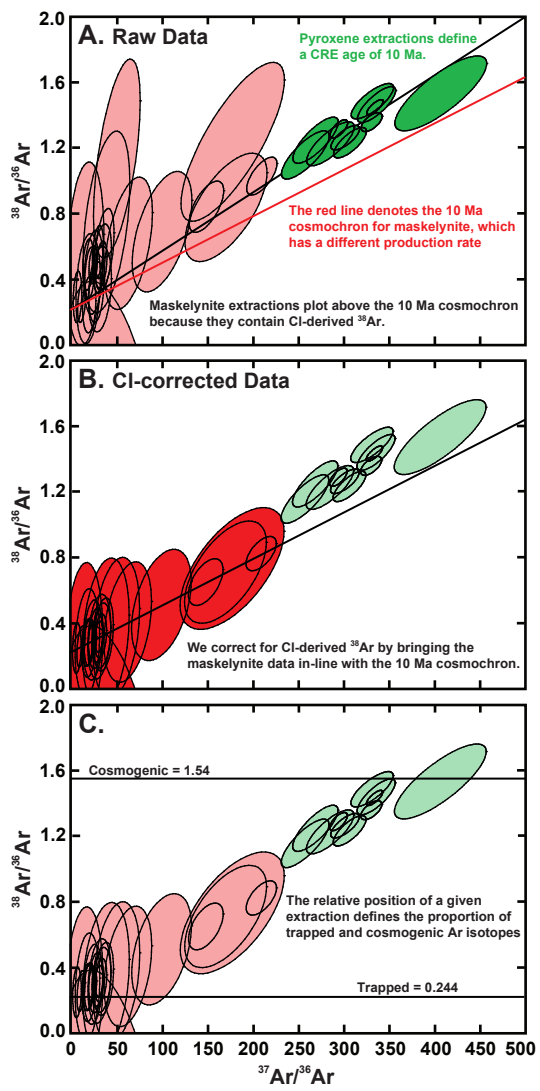
Table S2: Complete $^{40}\text{Ar}/^{39}\text{Ar}$ incremental heating details.

Supplementary Figure Captions

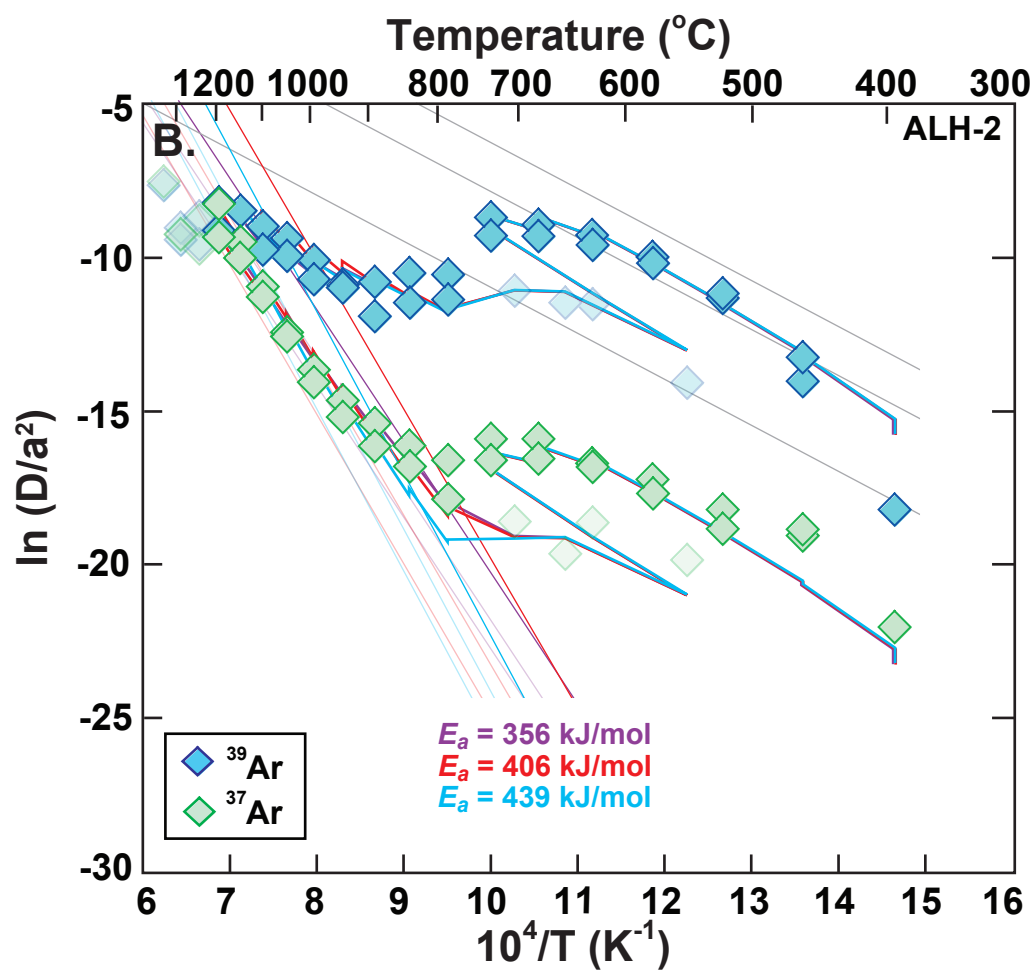
Figure S1: Cosmochron diagrams for ALH-2. **(A)** The raw (not corrected for chlorine-derived ^{38}Ar) pyroxene data (shown in green) define a cosmic ray exposure (CRE) age of 10.0 Ma, assuming a production rate of 14.2×10^{-13} moles/gCa/Ma (see text for discussion of production rates). Maskelynite data (shown in red) lie above the 10.0 Ma maskelynite cosmochron (production rate = 8.66×10^{-13} moles/gCa/Ma) because they contain Cl-derived ^{38}Ar . **(B)** To correct for Cl-derived ^{38}Ar we remove the excess ^{38}Ar such that the data come in-line with the 10.0 Ma maskelynite cosmochron. **(C)** By simple mass balance, the chlorine-corrected $^{38}\text{Ar}/^{36}\text{Ar}$ ratio of a given extraction defines the proportion of cosmogenic ($^{38}\text{Ar}/^{36}\text{Ar} = 1.54$; Weiler, 2002) and trapped Martian ($^{38}\text{Ar}/^{36}\text{Ar} = 0.244$; Bogard and Garrison, 1999) Ar isotopes (assuming these are the only two sources).

Figure S2: Arrhenius plot for ALH-2 calculated for plane slab geometry. Three model Arrhenius arrays are shown as solid lines behind the data. For each model, the E_a of maskelynite and its domain distribution, as well as the fractions of ^{37}Ar and ^{39}Ar within each maskelynite and pyroxene domain, were held constant. The E_a of pyroxene and its domain distribution were allowed to vary. The MDD-type models are not unique and the data can be fit using various combinations of pyroxene E_a and domain $\ln(D_o/a^2)$ values. Linearly regressing the pyroxene data should provide a well-constrained minimum E_a (shown in red), despite our ability to fit the data with a lower E_a (see text for discussion).

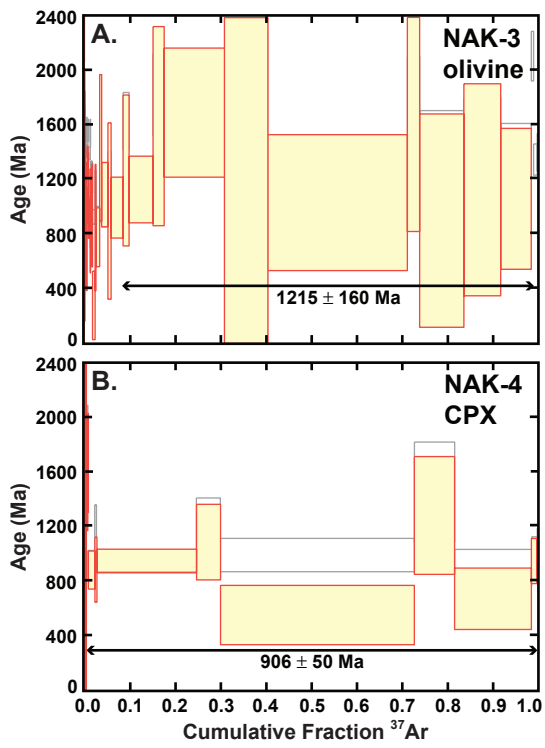
Figure S3: Apparent age spectra for **(A)** NAK-3 (olivine concentrate) and **(B)** NAK-4 (CPX concentrate) plotted against the cumulative fraction of ^{37}Ar . Raw data are shown in grey. Corrected data are shown in red.



Cassata et al. (2010) Figure S1



Cassata et al. (2010) Figure S2



Cassata et al. (2010) Figure S3

Table S1: Summary of published geochronometry

Reference	Method	Age $\pm 1\sigma$	Note
ALH 84001			
Jagoutz et al. (1994)	Sm-Nd	~4.56	wr, pyx, mask
Nyquist et al. (1995; 2001)	Sm-Nd	4.50 \pm 0.13	wr, pyx
Lapen et al. (2010)	Sm-Nd	4.41 \pm 0.03	wr, pyx
Nyquist et al. (1995; 2001)	Rb-Sr	4.55 \pm 0.30	wr, pyx
Borg et al. (1999)	Rb-Sr	3.90 \pm 0.04	carb
Wadhwa & Lugmair (1996)	Rb-Sr	3.84 \pm 0.05	wr, pyx
Wadhwa & Lugmair (1996)	Rb-Sr	1.39 \pm 0.10	carb, mask
Lapen et al. (2010)	Lu-Hf	4.09 \pm 0.03	wr, pyx, chromite
Jagoutz et al. (2009)	Pb-Pb	4.14 \pm 0.01	wr, pyx
Bouvier et al. (2009a)	Pb-Pb	4.08 \pm 0.10	wr, pyx
Borg et al. (1999)	Pb-Pb	4.04 \pm 0.10	carb
Jagoutz et al. (2009)	U-Pb	4.12 \pm 0.002	wr, pyx
Terada et al. (2003)	U-Pb	4.02 \pm 0.01	whitlockite, apatite
Terada et al. (2003)	Th-Pb	3.97 \pm 0.43	whitlockite, apatite
Jagoutz et al. (2009)	Th-Pb	2.93 \pm 0.41	wr, pyx
Ash et al. (1996)	Ar-Ar	4.1-4.2	mask
Knott et al. (1996)	Ar-Ar	~3.6	carb
Ilg et al. (1997)	Ar-Ar	4.07 \pm 0.04	mask with laserprobe
Turner et al. (1997)	Ar-Ar	3.8-4.05	mask
Bogard & Garrison (1999)	Ar-Ar	4.18 \pm 0.12	mask
Min & Reiners (2007)	U-Th-He	0.1-1.5, 1.8, 3.4	merrillite, apatite
Nakhla			
Gale et al. (1975)	Rb-Sr	1.23 \pm 0.01	pyx, wr, plag, ol
Papanastassiou & Wasserburg (1979)	Rb-Sr	1.30 \pm 0.02	pyx, wr, plag
Papanastassiou & Wasserburg (1979)	Rb-Sr	1.36 \pm 0.02	pyx, wr, plag
Nakamura et al. (1982)	Sm-Nd	1.26 \pm 0.07	wr, pyx, ol
Nakamura et al. (1982)	U-Th-Pb	1.28 \pm 0.05	wr, pyx, ol
Nakamura et al. (1982)	U-Th-Pb	1.24 \pm 0.11	wr, pyx, ol
Bouvier et al. (2007)	Pb-Pb	~1.3	wr, pyx
Podeseck (1973)	Ar-Ar	~1.3	plag
Bogard & Husain (1977)	Ar-Ar	1.32 \pm 0.04	plag
Swindle & Olson (2004)	Ar-Ar	1.33 \pm 0.01	plag
Park et al. (2009)	Ar-Ar	1.36 \pm 0.01	plag
Ganapathy & Ander (1969)	U-Th-He	~0.77	wr
MIL 03346			
Shih et al. (2006)	Sm-Nd	1.36 \pm 0.03	wr, pyx, ol, meso
Shih et al. (2006)	Rb-Sr	1.29 \pm 0.12	wr, pyx, ol, meso
Bouvier et al. (2009a)	Pb-Pb	1.33 \pm 0.14	wr, pyx
Bouvier et al. (2009b)	Sm-Nd	~1.335	wr, pyx
Bouvier et al. (2009b)	Lu-Hf	~1.335	wr, pyx
Park et al. (2009)	Ar-Ar	1.37 \pm 0.10	wr (mesostasis)
Park et al. (2009)	Ar-Ar	1.37 \pm 0.08	mesostasis
Park et al. (2009)	Ar-Ar	1.33 \pm 0.05	pyx
Murty et al. (2005)	U-Th-He	1.02 \pm 0.15	wr

All ages are reported at 1σ uncertainty

Table S2: Analytical Details

COMPLETE ⁴⁰Ar/³⁹Ar INCREMENTAL HEATING RESULTS

#	Temp (°C)	⁴⁰ Ar ± 1σ	³⁹ Ar ± 1σ	³⁹ Ar ± 1σ	³⁷ Ar ± 1σ	³⁶ Ar ± 1σ	⁴⁰ Ar* (%)	³⁹ Ar _k (%)	³⁸ Ar _{cos} (%)	³⁸ Ar _{atm} (%)	³⁸ Ar _{Cl} (%)	³⁶ Ar _{cos} (%)	³⁶ Ar _{atm} (%)	Ca/K	Apparent Age ± 1σ (Ma)	
ALH-1 whole-rock fragment																
1	411 °C	0.04159 ± 0.00064	0.00020 ± 0.00009	0.00003 ± 0.00003	0.00045 ± 0.00037	0.00004 ± 0.00002	35.7	99.8	5.2	35.2	51.2	2.3	97.4	4.4	1882 ± 1611	
2	464 °C	0.36736 ± 0.00098	0.00111 ± 0.00010	0.00013 ± 0.00003	0.01209 ± 0.00047	0.00024 ± 0.00002	64.7	99.2	31.1	37.8	20.8	11.4	87.3	21.5	3327 ± 220	
3	464 °C	0.27140 ± 0.00074	0.00078 ± 0.00009	0.00011 ± 0.00003	0.00645 ± 0.00041	0.00012 ± 0.00002	75.2	99.4	20.6	24.4	45.9	11.6	87.0	16.2	3622 ± 250	
4	517 °C	1.29725 ± 0.00155	0.00285 ± 0.00010	0.00023 ± 0.00003	0.01683 ± 0.00046	0.00052 ± 0.00002	76.8	99.6	24.9	50.4	9.5	7.2	92.0	11.6	4092 ± 96	
5	517 °C	0.77899 ± 0.00117	0.00174 ± 0.00010	0.00012 ± 0.00003	0.00847 ± 0.00039	0.00026 ± 0.00002	80.2	99.7	23.4	48.1	11.3	7.1	92.1	9.6	4136 ± 120	
6	570 °C	2.16958 ± 0.00253	0.00501 ± 0.00012	0.00034 ± 0.00003	0.02466 ± 0.00046	0.00058 ± 0.00002	84.9	99.7	25.1	37.8	18.8	9.4	89.5	9.7	4172 ± 60	
7	570 °C	1.24767 ± 0.00145	0.00302 ± 0.00011	0.00016 ± 0.00003	0.01449 ± 0.00047	0.00028 ± 0.00002	87.4	99.7	30.1	36.9	10.5	11.3	87.4	9.4	4144 ± 77	
8	623 °C	3.13274 ± 0.00372	0.00721 ± 0.00009	0.00038 ± 0.00003	0.03556 ± 0.00049	0.00065 ± 0.00002	88.8	99.7	31.9	35.8	9.1	12.2	86.4	9.7	4249 ± 40	
9	623 °C	1.83303 ± 0.00174	0.00465 ± 0.00012	0.00017 ± 0.00003	0.02088 ± 0.00047	0.00036 ± 0.00002	88.3	99.7	15.7	50.0	0.0	4.7	93.8	8.8	4083 ± 57	
10	675 °C	4.00297 ± 0.00352	0.00969 ± 0.00010	0.00055 ± 0.00003	0.05198 ± 0.00062	0.00076 ± 0.00002	90.0	99.6	32.4	28.3	17.5	15.1	83.1	10.6	4190 ± 34	
11	675 °C	2.18337 ± 0.00233	0.00565 ± 0.00012	0.00025 ± 0.00003	0.02861 ± 0.00057	0.00039 ± 0.00002	90.7	99.6	38.4	30.7	3.7	16.2	81.9	10.0	4095 ± 46	
12	727 °C	4.72604 ± 0.00462	0.01189 ± 0.00016	0.00059 ± 0.00003	0.06588 ± 0.00066	0.00094 ± 0.00003	89.7	99.6	37.9	31.8	5.7	15.5	82.6	10.9	4121 ± 37	
13	727 °C	2.08390 ± 0.00204	0.00528 ± 0.00011	0.00025 ± 0.00003	0.03210 ± 0.00066	0.00039 ± 0.00002	90.4	99.6	42.7	31.2	0.0	17.4	80.4	12.0	4123 ± 48	
14	779 °C	2.96100 ± 0.00312	0.00747 ± 0.00014	0.00038 ± 0.00003	0.08234 ± 0.00077	0.00043 ± 0.00002	94.4	99.2	58.5	17.1	0.0	33.4	61.5	21.8	4206 ± 37	
15	779 °C	1.56682 ± 0.00155	0.00416 ± 0.00009	0.00019 ± 0.00003	0.04148 ± 0.00063	0.00026 ± 0.00002	92.2	99.3	47.0	25.5	0.0	23.6	74.2	19.7	4083 ± 48	
16	831 °C	2.31593 ± 0.00332	0.00607 ± 0.00012	0.00048 ± 0.00003	0.12033 ± 0.00106	0.00056 ± 0.00002	91.3	98.6	67.9	16.3	0.0	37.4	56.9	39.4	4100 ± 43	
17	831 °C	1.16903 ± 0.00174	0.00299 ± 0.00011	0.00021 ± 0.00003	0.06057 ± 0.00070	0.00031 ± 0.00002	88.4	98.6	57.1	25.1	0.0	25.1	69.7	40.3	4091 ± 74	
18	882 °C	1.55461 ± 0.00175	0.00408 ± 0.00011	0.00054 ± 0.00003	0.16326 ± 0.00097	0.00056 ± 0.00002	90.3	97.2	79.7	10.8	0.0	49.8	42.5	80.6	4103 ± 59	
19	882 °C	0.60874 ± 0.00104	0.00164 ± 0.00009	0.00026 ± 0.00003	0.07221 ± 0.00072	0.00031 ± 0.00002	83.2	96.9	76.8	15.2	0.0	41.7	52.1	89.2	3938 ± 121	
20	933 °C	0.78197 ± 0.00127	0.00251 ± 0.00010	0.00054 ± 0.00003	0.18293 ± 0.00119	0.00056 ± 0.00002	81.9	94.9	83.7	10.2	0.0	51.6	39.8	150.2	3662 ± 97	
21	933 °C	0.24790 ± 0.00083	0.00096 ± 0.00009	0.00024 ± 0.00003	0.07181 ± 0.00071	0.00025 ± 0.00002	99.8	94.8	85.0	9.8	0.0	53.3	39.1	154.9	3686 ± 164	
22	984 °C	0.52263 ± 0.00108	0.00224 ± 0.00010	0.00062 ± 0.00003	0.20334 ± 0.00191	0.00060 ± 0.00002	99.8	93.7	87.4	7.8	0.0	58.2	32.8	190.2	3546 ± 75	
23	984 °C	0.22175 ± 0.00091	0.00120 ± 0.00010	0.00025 ± 0.00004	0.08881 ± 0.00075	0.00034 ± 0.00002	99.6	94.9	74.8	18.9	0.0	35.8	57.2	153.1	3168 ± 131	
24	1034 °C	0.66438 ± 0.00127	0.00341 ± 0.00011	0.00089 ± 0.00004	0.26577 ± 0.00207	0.00090 ± 0.00003	99.7	94.6	85.6	9.4	0.0	54.4	37.8	161.5	3252 ± 52	
25	1034 °C	0.24736 ± 0.00088	0.00155 ± 0.00009	0.00039 ± 0.00004	0.12421 ± 0.00083	0.00046 ± 0.00002	99.6	94.4	80.8	14.0	0.0	44.3	48.5	165.8	2952 ± 94	
26	CO2	0.04591 ± 0.00103	0.00023 ± 0.00004	0.00008 ± 0.00002	0.02368 ± 0.00109	0.00010 ± 0.00002	99.5	92.7	81.1	15.1	0.0	43.0	50.5	220.6	3336 ± 319	
27	CO2	0.08710 ± 0.00102	0.00032 ± 0.00004	0.00022 ± 0.00002	0.05521 ± 0.00099	0.00022 ± 0.00002	99.6	87.8	90.0	8.0	0.0	59.6	33.7	390.8	3907 ± 244	
28	CO2	0.06710 ± 0.00102	0.00025 ± 0.00005	0.00011 ± 0.00002	0.03923 ± 0.00104	0.00013 ± 0.00003	99.6	88.9	85.2	11.8	0.0	48.9	42.9	352.5	3872 ± 367	
29	CO2	0.43082 ± 0.00128	0.00176 ± 0.00005	0.00105 ± 0.00003	0.30143 ± 0.00275	0.00088 ± 0.00003	99.8	88.1	94.0	3.7	0.0	72.9	17.9	380.9	3714 ± 56	
30	CO2	0.10262 ± 0.00107	0.00045 ± 0.00004	0.00025 ± 0.00002	0.06676 ± 0.00114	0.00027 ± 0.00002	99.5	89.8	86.8	10.7	0.0	52.6	40.9	320.5	3553 ± 168	
31	CO2	0.70644 ± 0.00122	0.00281 ± 0.00004	0.00199 ± 0.00003	0.51633 ± 0.00600	0.00184 ± 0.00003	99.6	87.2	91.5	6.5	0.0	63.9	28.7	412.4	3767 ± 29	
32	CO2	2.62526 ± 0.00339	0.00755 ± 0.00006	0.01305 ± 0.00007	2.98093 ± 0.01475	0.01067 ± 0.00007	99.7	72.6	95.7	3.4	0.0	75.8	16.8	1066.4	4595 ± 24	
ALH-2 whole-rock fragment																
1	410 °C	0.08089 ± 0.00130	0.00026 ± 0.00006	0.00000 ± 0.00002	0.00000 ± 0.00069	0.00000 ± 0.00002	---	---	---	---	---	---	---	---	--- ± ---	
2	411 °C	0.07578 ± 0.00127	0.00026 ± 0.00006	0.00000 ± 0.00002	0.00141 ± 0.00068	0.00003 ± 0.00002	59.0	99.6	---	---	---	---	---	---	352.5	2984 ± 775
3	464 °C	0.49557 ± 0.00198	0.00189 ± 0.00005	0.00010 ± 0.00002	0.00504 ± 0.00073	0.00015 ± 0.00002	82.8	99.8	16.6	32.7	27.7	7.4	91.7	380.9	3335 ± 82	
4	464 °C	0.41174 ± 0.00153	0.00166 ± 0.00007	0.00008 ± 0.00002	0.00302 ± 0.00069	0.00012 ± 0.00002	82.5	99.9	13.4	37.2	22.4	5.4	94.0	320.5	3248 ± 104	
5	517 °C	1.57806 ± 0.00189	0.00532 ± 0.00009	0.00017 ± 0.00002	0.00402 ± 0.00071	0.00021 ± 0.00002	91.9	99.9	7.8	29.0	25.1	4.1	95.4	412.4	3687 ± 38	
6	517 °C	1.07202 ± 0.00197	0.00368 ± 0.00008	0.00008 ± 0.00002	0.00171 ± 0.00068	0.00009 ± 0.00002	94.9	100.0	7.4	27.3	6.7	4.1	95.4	1066.4	3711 ± 45	
7	571 °C	2.57844 ± 0.00330	0.00801 ± 0.00010	0.00023 ± 0.00002	0.00668 ± 0.00069	0.00023 ± 0.00002	94.8	99.8	9.8	22.7	24.6	6.3	92.9	1.6	3868 ± 28	
8	570 °C	1.58531 ± 0.00205	0.00473 ± 0.00010	0.00010 ± 0.00002	0.00335 ± 0.00070	0.00017 ± 0.00002	93.4	100.0	2.9	40.0	0.0	1.1	98.4	1.4	3909 ± 43	
9	624 °C	3.08392 ± 0.00339	0.00911 ± 0.00015	0.00026 ± 0.00002	0.00727 ± 0.00072	0.00030 ± 0.00002	94.2	99.9	9.3	26.5	21.3	5.2	94.1	1.6	3938 ± 33	
10	623 °C	1.82617 ± 0.00230	0.00529 ± 0.00009	0.00015 ± 0.00002	0.00535 ± 0.00068	0.00015 ± 0.00002	95.4	99.9	11.8	21.8	23.5	7.8	91.2	2.0	3990 ± 36	
11	676 °C	3.07916 ± 0.00321	0.00868 ± 0.00011	0.00028 ± 0.00002	0.01084 ± 0.00072	0.00034 ± 0.00002	93.5	99.9	12.8	27.5	21.9	6.8	92.3	2.5	4001 ± 29	
12	676 °C	1.66334 ± 0.00196	0.00474 ± 0.00006	0.00011 ± 0.00002	0.00477 ± 0.00068	0.00017 ± 0.00002	93.9	99.9	13.8	34.1	1.8	6.0	93.3	2.0	3990 ± 33	
13	728 °C	2.49725 ± 0.00256	0.00706 ± 0.00010	0.00021 ± 0.00002	0.00810 ± 0.00070	0.00024 ± 0.00002	94.3	99.9	13.0	26.5	18.8	7.2	92.0	2.2	4009 ± 31	
14	728 °C	1.12231 ± 0.00180	0.00316 ± 0.00006	0.00008 ± 0.00002	0.00365 ± 0.00070	0.00012 ± 0.00002	94.0	99.9	15.4	33.0	2.6	6.8	92.3	2.3	4013 ± 42	
15	623 °C	0.41773 ± 0.00160	0.00112 ± 0.00005	0.00005 ± 0.00001	0.00168 ± 0.00030	0.00014 ± 0.00002	78.9	99.9	9.8	64.3	0.0	2.3	97.4	2.9	3811 ± 121	
16	544 °C	0.07181 ± 0.00072	0.00009 ± 0.00004	0.00000 ± 0.00001	0.00054 ± 0.00029	0.00000 ± 0.00001	93.7	99.6	---	---	---	---	---	11.7	5355 ± 1664	
17	649 °C	0.51221 ± 0.00100	0.00129 ± 0.00005	0.00005 ± 0.00001	0.00070 ± 0.00028	0.00010 ± 0.00002	88.2	100.0	5.1	51.4	8.7	1.6	98.3	1.1	4088 ± 84	
18																

5	517 °C	0.06900 ± 0.00048	0.00019 ± 0.00004	0.00002 ± 0.00002	0.00038 ± 0.00078	0.00001 ± 0.00002	88.0	99.9	5.4	9.9	75.3	6.2	93.1	3.9	3931 ± 504
6	570 °C	0.17500 ± 0.00066	0.00045 ± 0.00003	0.00003 ± 0.00002	0.00208 ± 0.00079	0.00006 ± 0.00002	80.0	99.7	26.4	37.5	16.3	7.8	91.3	9.1	3897 ± 199
7	570 °C	0.09736 ± 0.00063	0.00023 ± 0.00006	0.00000 ± 0.00002	0.00039 ± 0.00075	0.00002 ± 0.00002	82.2	99.9	---	---	0.0	---	---	3.3	4082 ± 495
8	624 °C	0.22829 ± 0.00093	0.00068 ± 0.00005	0.00000 ± 0.00002	0.00522 ± 0.00076	0.00004 ± 0.00002	85.3	99.5	---	---	0.0	---	---	15.0	3762 ± 186
9	623 °C	0.11847 ± 0.00068	0.00029 ± 0.00006	0.00002 ± 0.00002	0.00205 ± 0.00077	0.00004 ± 0.00001	81.2	99.5	38.7	35.5	6.5	11.6	87.1	13.7	3981 ± 382
10	675 °C	0.25226 ± 0.00061	0.00062 ± 0.00003	0.00006 ± 0.00002	0.00265 ± 0.00077	0.00010 ± 0.00002	77.4	99.7	16.6	30.1	39.9	6.2	93.0	8.4	3919 ± 152
11	675 °C	0.13092 ± 0.00077	0.00033 ± 0.00005	0.00000 ± 0.00002	0.00123 ± 0.00074	0.00004 ± 0.00002	81.1	99.7	---	---	0.0	---	---	7.3	3952 ± 314
12	728 °C	0.29867 ± 0.00086	0.00081 ± 0.00005	0.00003 ± 0.00002	0.00301 ± 0.00078	0.00007 ± 0.00001	85.0	99.7	---	50.0	0.0	---	100.0	7.3	3917 ± 138
13	728 °C	0.07221 ± 0.00072	0.00022 ± 0.00003	0.00003 ± 0.00002	0.00144 ± 0.00075	0.00005 ± 0.00002	55.5	99.5	18.2	34.2	38.0	6.0	93.3	13.1	3104 ± 672
14	780 °C	0.06881 ± 0.00063	0.00023 ± 0.00004	0.00001 ± 0.00002	0.00235 ± 0.00079	0.00006 ± 0.00002	44.5	99.3	---	---	0.0	---	---	20.0	2621 ± 709
15	780 °C	0.02168 ± 0.00048	0.00012 ± 0.00004	0.00000 ± 0.00002	0.00054 ± 0.00072	0.00002 ± 0.00001	14.7	99.7	---	---	0.0	---	---	8.6	896 ± 3430
16	831 °C	0.02455 ± 0.00057	0.00002 ± 0.00004	0.00002 ± 0.00002	0.00105 ± 0.00076	0.00001 ± 0.00001	79.1	96.7	17.1	7.1	74.5	22.2	75.2	95.7	5678 ± 3345
17	831 °C	0.00873 ± 0.00054	0.00010 ± 0.00004	0.00002 ± 0.00002	0.00066 ± 0.00075	0.00000 ± 0.00001	---	99.5	11.3	---	91.8	---	---	13.5	2832 ± 1473
18	882 °C	0.02050 ± 0.00047	0.00005 ± 0.00004	0.00002 ± 0.00002	0.00094 ± 0.00078	0.00000 ± 0.00002	---	98.8	17.8	---	83.8	---	---	34.1	4464 ± 1910
19	883 °C	0.00913 ± 0.00042	0.00004 ± 0.00004	0.00000 ± 0.00002	0.00049 ± 0.00080	0.00004 ± 0.00001	97.8	99.2	---	---	0.0	---	---	23.9	3363 ± 1508
20	933 °C	0.02257 ± 0.00054	0.00016 ± 0.00005	0.00004 ± 0.00002	0.00388 ± 0.00081	0.00009 ± 0.00002	98.2	98.3	22.1	39.7	32.9	6.3	92.5	48.0	2695 ± 429
21	933 °C	0.00932 ± 0.00044	0.00011 ± 0.00004	0.00002 ± 0.00002	0.00146 ± 0.00082	0.00001 ± 0.00001	99.5	99.1	12.9	7.7	73.8	16.4	80.5	26.0	2030 ± 486
22	984 °C	0.03084 ± 0.00051	0.00022 ± 0.00005	0.00005 ± 0.00002	0.00940 ± 0.00081	0.00004 ± 0.00002	99.5	97.1	38.7	10.4	45.5	29.3	65.1	85.4	2718 ± 312
23	984 °C	0.01363 ± 0.00041	0.00012 ± 0.00004	0.00000 ± 0.00002	0.00672 ± 0.00082	0.00005 ± 0.00002	98.0	96.0	---	---	---	---	---	116.5	2464 ± 477
24	1034 °C	0.04232 ± 0.00058	0.00043 ± 0.00005	0.00011 ± 0.00002	0.01932 ± 0.00092	0.00008 ± 0.00002	99.5	96.9	37.6	7.7	49.7	34.7	58.6	91.3	2262 ± 147
25	1034 °C	0.01764 ± 0.00047	0.00025 ± 0.00007	0.00006 ± 0.00002	0.01160 ± 0.00088	0.00007 ± 0.00002	98.6	96.8	39.1	14.4	41.4	23.7	71.7	92.7	1825 ± 219
26	CO2	0.00305 ± 0.00039	0.00031 ± 0.00007	0.00076 ± 0.00002	0.35503 ± 0.00336	0.00062 ± 0.00002	93.1	20.0	98.0	1.0	0.0	78.0	6.8	11285.9	1369 ± 1088
27	CO2	0.01188 ± 0.00038	0.00289 ± 0.00007	0.00820 ± 0.00005	3.82003 ± 0.03280	0.00664 ± 0.00006	82.4	8.2	98.1	1.0	0.0	78.5	6.3	31715.2	1271 ± 382
28	CO2	0.01333 ± 0.00034	0.00291 ± 0.00008	0.00807 ± 0.00005	3.67393 ± 0.04352	0.00631 ± 0.00005	93.4	12.2	98.6	0.4	0.0	81.8	2.8	20311.9	1126 ± 226
29	CO2	0.02256 ± 0.00030	0.00524 ± 0.00006	0.01462 ± 0.00006	6.67713 ± 0.02881	0.01161 ± 0.00007	88.3	11.4	98.4	0.7	0.0	80.2	4.6	21910.7	1083 ± 154
30	CO2	0.02539 ± 0.00030	0.00832 ± 0.00006	0.02464 ± 0.00010	11.17647 ± 0.06032	0.01913 ± 0.00010	91.9	6.7	98.8	0.3	0.0	82.4	2.1	39324.6	1281 ± 225

ALH-4 whole-rock fragment

1	464 °C	1.61102 ± 0.00151	0.00971 ± 0.00010	0.00074 ± 0.00002	0.08437 ± 0.00094	0.00067 ± 0.00002	79.8	99.4	23.8	17.7	42.3	16.9	79.7	17.1	3236 ± 78
2	464 °C	1.13915 ± 0.00132	0.00668 ± 0.00010	0.00031 ± 0.00002	0.03564 ± 0.00080	0.00031 ± 0.00002	86.4	99.6	23.6	19.7	30.6	15.4	81.5	11285.9	3367 ± 53
3	517 °C	4.31930 ± 0.00380	0.02174 ± 0.00016	0.00094 ± 0.00002	0.07975 ± 0.00122	0.00093 ± 0.00003	88.7	99.7	17.6	20.7	33.5	11.6	86.1	31715.2	3629 ± 43
4	518 °C	2.64685 ± 0.00245	0.01232 ± 0.00013	0.00045 ± 0.00002	0.02659 ± 0.00081	0.00043 ± 0.00002	91.1	99.9	12.2	20.9	33.6	8.3	90.1	20311.9	3780 ± 35
5	571 °C	7.35751 ± 0.00448	0.03305 ± 0.00021	0.00103 ± 0.00002	0.07037 ± 0.00100	0.00105 ± 0.00003	92.2	99.9	14.1	22.2	24.6	9.0	89.2	21910.7	3856 ± 31
6	570 °C	4.39385 ± 0.00312	0.01865 ± 0.00013	0.00054 ± 0.00002	0.03488 ± 0.00083	0.00054 ± 0.00003	93.3	99.9	13.5	21.9	22.4	8.7	89.6	39324.6	3962 ± 26
7	623 °C	10.52270 ± 0.00512	0.04302 ± 0.00023	0.00135 ± 0.00003	0.09538 ± 0.00153	0.00131 ± 0.00004	93.3	99.8	14.7	20.8	25.6	9.8	88.2	4.4	4024 ± 26
8	623 °C	6.02100 ± 0.00407	0.02456 ± 0.00017	0.00088 ± 0.00003	0.04779 ± 0.00118	0.00063 ± 0.00003	94.4	99.9	14.7	20.1	21.0	10.1	87.9	3.8	4043 ± 23
9	676 °C	13.13432 ± 0.00764	0.05258 ± 0.00021	0.00175 ± 0.00004	0.13821 ± 0.00143	0.00184 ± 0.00004	92.5	99.8	16.4	22.6	24.2	10.1	87.9	5.2	4046 ± 31
10	676 °C	6.82103 ± 0.00482	0.02821 ± 0.00018	0.00076 ± 0.00003	0.05453 ± 0.00118	0.00076 ± 0.00003	94.0	99.9	15.0	21.6	17.9	9.7	88.4	3.8	4015 ± 24
11	728 °C	12.70107 ± 0.00568	0.05366 ± 0.00017	0.00164 ± 0.00003	0.12045 ± 0.00154	0.00170 ± 0.00005	92.8	99.8	15.3	22.4	22.3	9.6	88.6	4.4	3963 ± 29
12	728 °C	5.25582 ± 0.00387	0.02215 ± 0.00016	0.00059 ± 0.00003	0.04595 ± 0.00104	0.00048 ± 0.00003	95.3	99.9	16.3	16.7	20.7	13.0	84.4	4.1	4007 ± 21
13	780 °C	7.50290 ± 0.00501	0.03215 ± 0.00017	0.00096 ± 0.00003	0.08118 ± 0.00133	0.00072 ± 0.00003	95.2	99.8	17.6	14.9	26.6	15.2	81.7	5.0	3981 ± 19
14	780 °C	3.50447 ± 0.00387	0.01462 ± 0.00013	0.00043 ± 0.00003	0.03416 ± 0.00102	0.00035 ± 0.00003	94.8	99.8	16.6	16.9	24.8	13.1	84.3	4.6	4017 ± 24
15	806 °C	2.99142 ± 0.00341	0.01292 ± 0.00013	0.00045 ± 0.00002	0.04139 ± 0.00117	0.00030 ± 0.00003	95.3	99.8	19.0	12.5	33.7	18.7	77.7	6.3	3971 ± 25
16	806 °C	1.62066 ± 0.00230	0.00700 ± 0.00010	0.00024 ± 0.00002	0.02399 ± 0.00101	0.00024 ± 0.00003	92.4	99.8	20.4	20.3	24.3	13.4	84.0	6.7	3925 ± 37
17	831 °C	1.47006 ± 0.00193	0.00668 ± 0.00011	0.00033 ± 0.00002	0.04160 ± 0.00121	0.00027 ± 0.00003	91.8	99.6	26.4	14.8	33.8	21.1	74.8	12.3	3849 ± 40
18	831 °C	0.75279 ± 0.00171	0.00351 ± 0.00009	0.00022 ± 0.00002	0.02481 ± 0.00113	0.00021 ± 0.00003	86.5	99.5	23.6	18.6	38.1	16.2	80.6	13.9	3730 ± 70
19	857 °C	0.66904 ± 0.00180	0.00348 ± 0.00009	0.00030 ± 0.00002	0.04412 ± 0.00128	0.00026 ± 0.00003	82.9	99.1	30.4	15.2	40.1	23.0	72.5	25.1	3531 ± 77
20	857 °C	0.36389 ± 0.00170	0.00207 ± 0.00008	0.00019 ± 0.00002	0.02931 ± 0.00114	0.00022 ± 0.00003	70.8	99.0	32.1	22.5	32.0	17.8	78.7	28.1	3198 ± 144
21	882 °C	0.45798 ± 0.00163	0.00281 ± 0.00008	0.00036 ± 0.00002	0.06555 ± 0.00129	0.00027 ± 0.00003	75.6	98.6	32.5	12.6	45.1	27.4	67.2	39.2	3207 ± 107
22	883 °C	0.23014 ± 0.00167	0.00172 ± 0.00008	0.00018 ± 0.00002	0.03713 ± 0.00117	0.00022 ± 0.00003	58.1	98.5	43.6	21.8	22.6	22.9	72.6	43.0	2646 ± 224
23	933 °C	2.71685 ± 0.00279	0.01519 ± 0.00012	0.00105 ± 0.00003	0.17547 ± 0.00196	0.00081 ± 0.00003	88.1	99.2	34.8	12.3	35.0	29.1	65.2	22.8	3501 ± 42
24	933 °C	0.50178 ± 0.00157	0.00383 ± 0.00008	0.00048 ± 0.00002	0.08993 ± 0.00144	0.00036 ± 0.00003	73.8	98.4	39.0	11.0	40.1	33.6	59.8	48.8	2909 ± 102
25	984 °C	1.39225 ± 0.00214	0.01305 ± 0.00012	0.00173 ± 0.00003	0.38194 ± 0.00383	0.00131 ± 0.00003	69.6	98.0	46.0	9.8	34.7	39.3	53.0	58.6	2632 ± 118
26	984 °C	0.23496 ± 0.00168	0.00447 ± 0.00009	0.00081 ± 0.00002	0.21038 ± 0.00225	0.00062 ± 0.00003	26.9	96.7	54.1	8.5	30.4	45.6	45.4	95.3	1967 ± 324
27	1034 °C	0.89964 ± 0.00186	0.01363 ± 0.00012	0.00281 ± 0.00003	0.82827 ± 0.00629	0.00220 ± 0.00003	41.4	95.8	61.3	7.5	25.0	50.7	39.3	124.4	1593 ± 284
28	1034 °C	0.58629 ± 0.00167	0.00651 ± 0.00009	0.00147 ± 0.00003	0.46527 ± 0.00393	0.00118 ± 0.00003	55.6	95.0	65.7	7.1	21.5	53.3	36.3	147.4	2409 ± 182
29	1084 °C	2.15730 ± 0.00262	0.01943 ± 0.00013	0.00488 ± 0.00004	1.58351 ± 0.01382	0.00398 ± 0.00004	59.7	94.3	67.4	7.1	20.2	53.6	35.8	169.3	2710 ± 220
30	1084 °C	0.49393 ± 0.00174	0.00572 ± 0.00009	0.00225 ± 0.00003	0.79025 ± 0.00646	0.00183 ± 0.00003	67.9	90.4	93.7	2.8	0.0	74.4	14.2	299.4	2209 ± 121
31	1134 °C	1.37686 ± 0.00222	0.01503 ± 0.00013	0.00963 ± 0.00005	3.45573 ± 0.01407	0.00751 ± 0.00004	73.7	84.0	96.2	1.5	0.0	79.9	7.9	536.3	2481 ± 146
32	1133 °C	0.40294 ± 0.00160	0.00378 ± 0.00008	0.00311 ± 0.00003	1.13697 ± 0.00882	0.00249 ± 0.00003	99.7	79.1	96.1	2.0	0.0	77.7	10.2	744.5	3181 ± 40
33	1183 °C	0.87937 ± 0.00214	0.00697 ± 0.00010	0.00724 ± 0.00005	2.68974 ± 0.01861	0.00589 ± 0.00005	99.6	73.2	96.1	2.3	0.0	76.5	11.4	1033.9	3558 ± 34
34	1183 °C	0.32046 ± 0.00171	0.00192 ± 0.00008	0.00209 ± 0.00003	0.72428 ± 0.00784	0.00176 ± 0.00003	99.6	73.8	94.6	3.3	0.6	72.9	16.2	1001.1	3984 ± 93
35	1233 °C	0.47114 ± 0.00174	0.00246 ± 0.00008	0.00303 ± 0.00003	1.05237 ± 0.01024	0.00253 ± 0.00003	99.6	70.2	95.0	3.1	0.5	73.7	15.2	1194.7	4289 ± 82
36	1233 °C	0.28105 ± 0.00186	0.00159 ± 0.00009	0.00208 ± 0.00003	0.73648 ± 0.00945	0.00169 ± 0.00003	99.7	67.8	96.5	2.2	0.0	77.2	11.2	1342.3	4221 ± 132
37	1282 °C	0.58859 ± 0.00193	0.00330 ± 0.00008	0.00482 ± 0.00004	1.71600 ± 0.00955	0.00384 ± 0.00004	99.7	63.9	97.0	1.8	0.0	78.8	9.3	1595.5	4329 ± 66
38	1283 °C	0.27440 ± 0.00166	0.00168 ± 0.00008	0.00262 ± 0.00003	0.92268 ± 0.01291	0.00219 ± 0.00003	99.4	61.7	95.9	2.9	0.0	74.4	14.4	1749.4	4242 ± 134
39	1332 °C	1.26343 ± 0.00193	0.00948 ± 0.00011	0.01664 ± 0.00006	6.10437 ± 0.05747	0.01309 ± 0.00006	99.6	55.3	97.5	1.4	0.0	80.3	7.4	2283.8	4090 ± 42
40	1332 °C	0.29042 ± 0.00186	0.00241 ± 0.00008	0.00457 ± 0.00003	1.67626 ± 0.01224	0.00359 ± 0.00003	---	---	---	---	---	---	---	---	---
41	1381 °C	0.02446 ± 0.00148	0.00025 ± 0.00007	0.00033 ± 0.00002	0.10960 ± 0.00199	0.00026 ± 0.00002	---	---	---	---	---	---	---	---	---
42	1381 °C	0.01442 ± 0.00149	0.00020 ± 0.00006	0.00003 ± 0.00002	0.01693 ± 0.00120	0.00007 ± 0.00002	---	---	---	---	---	---	---	---	---
43	1428 °C	0.00575 ± 0.00146	0.00018 ± 0.00006	0.00001 ± 0.00002	0.00410 ± 0.00113	0.00003 ± 0.00002	---	---	---	---	---	---	---	---	---
44	1429 °C	0.00580 ± 0.00149	0.00009 ± 0.00006	0.00001 ± 0.00002	0.00851 ± 0.00118	0.00002 ± 0.00002	---	---	---	---	---	---	---	---	---
45	1521 °C	0.09616 ± 0.00169	0.00181 ± 0.00008	0.00014 ± 0.00002	0.00658 ± 0.00121	0.00036 ± 0.00003	---	---	---	---	---	---	---	---	---
46	1306 °C	0.05600 ± 0.00166	0.00134 ± 0.00007	0.00006 ± 0.00002	-0.00090 ± 0.00125	0.00021 ± 0.00003	---	---	---	---	---	---	---	---	---

19	883 °C	1.13101 ± 0.00136	0.02495 ± 0.00015	0.00096 ± 0.00002	0.06058 ± 0.00071	0.00026 ± 0.00002	99.6	99.8	13.8	4.0	50.3	33.0	60.8	4.8	1352 ± 10
20	933 °C	1.75512 ± 0.00201	0.03959 ± 0.00021	0.00218 ± 0.00003	0.13935 ± 0.00090	0.00051 ± 0.00002	99.5	99.8	14.0	3.1	60.7	38.8	54.0	6.9	1331 ± 9
21	933 °C	0.87340 ± 0.00164	0.01951 ± 0.00014	0.00106 ± 0.00003	0.07038 ± 0.00090	0.00033 ± 0.00002	99.2	99.7	14.6	4.9	57.9	30.1	64.3	7.1	1338 ± 11
22	984 °C	1.49750 ± 0.00164	0.03668 ± 0.00014	0.00312 ± 0.00004	0.22821 ± 0.00241	0.00081 ± 0.00002	99.1	99.6	16.0	3.3	66.3	39.9	52.6	12.2	1253 ± 9
23	984 °C	0.60130 ± 0.00138	0.01444 ± 0.00011	0.00115 ± 0.00002	0.08983 ± 0.00083	0.00037 ± 0.00003	98.9	99.6	17.1	4.6	63.0	34.7	58.8	12.2	1269 ± 11
24	1034 °C	1.49488 ± 0.00183	0.04002 ± 0.00022	0.00484 ± 0.00004	0.62927 ± 0.00590	0.00170 ± 0.00003	98.6	98.9	28.4	3.3	58.1	52.3	37.9	31.2	1176 ± 9
25	1034 °C	0.48433 ± 0.00130	0.01208 ± 0.00011	0.00136 ± 0.00003	0.20645 ± 0.00187	0.00058 ± 0.00002	98.4	98.8	33.2	4.3	51.5	50.0	40.7	33.9	1238 ± 12
26	CO2	0.00912 ± 0.00043	0.00025 ± 0.00003	0.00002 ± 0.00002	0.02040 ± 0.00051	0.00002 ± 0.00003	99.1	94.2	77.0	3.8	0.0	51.1	16.1	172.1	1213 ± 168
27	CO2	0.07894 ± 0.00050	0.00291 ± 0.00006	0.00246 ± 0.00004	1.06397 ± 0.00860	0.00189 ± 0.00003	97.6	74.6	97.5	0.6	0.0	82.0	3.1	962.6	1137 ± 32
28	CO2	0.05956 ± 0.00054	0.00209 ± 0.00007	0.00185 ± 0.00003	0.80535 ± 0.00980	0.00147 ± 0.00003	95.0	73.2	96.9	1.2	0.0	79.1	6.3	1033.5	1172 ± 47
29	CO2	0.03452 ± 0.00051	0.00163 ± 0.00006	0.00184 ± 0.00003	0.81994 ± 0.01291	0.00143 ± 0.00003	95.8	65.1	97.8	0.6	0.0	81.6	3.2	1512.6	1029 ± 59
30	CO2	0.03034 ± 0.00047	0.00135 ± 0.00006	0.00155 ± 0.00003	0.67697 ± 0.00717	0.00117 ± 0.00003	99.4	65.2	98.4	0.1	0.0	84.2	0.5	1502.0	1102 ± 69
31	CO2	0.02973 ± 0.00060	0.00109 ± 0.00004	0.00103 ± 0.00003	0.45106 ± 0.00670	0.00082 ± 0.00003	94.5	71.3	97.0	1.2	0.0	79.2	6.2	1133.0	1148 ± 63
32	CO2	0.04811 ± 0.00064	0.00182 ± 0.00006	0.00147 ± 0.00003	0.66210 ± 0.00646	0.00122 ± 0.00003	91.6	74.7	95.9	2.1	0.0	75.2	10.4	952.8	1059 ± 52
33	CO2	0.05696 ± 0.00062	0.00229 ± 0.00004	0.00189 ± 0.00003	0.83931 ± 0.01173	0.00155 ± 0.00003	91.1	74.5	96.0	2.0	0.0	75.5	10.2	963.0	1010 ± 37
34	CO2	0.20694 ± 0.00059	0.00926 ± 0.00010	0.00941 ± 0.00008	4.32694 ± 0.03113	0.00745 ± 0.00006	94.3	67.5	97.3	1.0	0.0	79.6	5.0	1357.2	1031 ± 24
35	CO2	1.52491 ± 0.00184	0.07857 ± 0.00035	0.11517 ± 0.00035	53.60083 ± 0.28740	0.09326 ± 0.00018	86.4	52.6	97.3	1.4	0.0	77.8	7.0	2543.0	1047 ± 39

NAK-2

whole-rock fragment															
1	410 °C	0.02248 ± 0.00109	0.00052 ± 0.00012	0.00000 ± 0.00003	0.00074 ± 0.00022	0.00000 ± 0.00003	---	---	---	---	---	---	---	---	---
2	464 °C	0.34221 ± 0.00114	0.00779 ± 0.00013	0.00023 ± 0.00003	0.01220 ± 0.00036	0.00005 ± 0.00003	83.6	99.9	15.1	2.6	40.5	44.5	49.1	1357.2	1166 ± 227
3	464 °C	0.30981 ± 0.00193	0.00685 ± 0.00012	0.00019 ± 0.00003	0.00952 ± 0.00033	0.00012 ± 0.00003	25.3	99.9	14.2	13.0	29.8	14.3	83.6	2543.0	462 ± 475
4	518 °C	2.09569 ± 0.00247	0.04140 ± 0.00015	0.00119 ± 0.00004	0.05093 ± 0.00066	0.00040 ± 0.00003	68.0	99.9	12.0	6.0	39.6	23.2	73.4	2.4	1110 ± 90
5	517 °C	1.26291 ± 0.00165	0.02508 ± 0.00021	0.00051 ± 0.00004	0.01932 ± 0.00041	0.00018 ± 0.00003	74.8	99.9	10.6	6.6	23.2	19.6	77.5	1.5	1186 ± 93
6	570 °C	4.60462 ± 0.00458	0.08167 ± 0.00039	0.00148 ± 0.00004	0.06034 ± 0.00068	0.00045 ± 0.00003	83.8	99.9	11.5	5.4	15.6	24.4	72.1	1.4	1395 ± 43
7	570 °C	2.41290 ± 0.00293	0.04270 ± 0.00033	0.00063 ± 0.00003	0.02699 ± 0.00048	0.00025 ± 0.00003	80.6	100.0	9.1	7.9	0.0	14.9	82.2	1.2	1360 ± 61
8	624 °C	8.36723 ± 0.00656	0.15522 ± 0.00040	0.00254 ± 0.00005	0.11238 ± 0.00098	0.00077 ± 0.00004	85.3	99.9	12.5	5.2	7.8	26.6	69.6	1.4	1369 ± 35
9	623 °C	4.58727 ± 0.00458	0.08400 ± 0.00022	0.00149 ± 0.00004	0.06665 ± 0.00073	0.00036 ± 0.00003	88.8	99.9	12.6	3.7	15.1	33.4	61.7	1.6	1421 ± 32
10	675 °C	15.28867 ± 0.00755	0.29242 ± 0.00062	0.00457 ± 0.00005	0.26325 ± 0.00146	0.00112 ± 0.00004	91.5	99.9	16.2	3.0	2.7	42.9	50.9	1.8	1407 ± 20
11	675 °C	7.95922 ± 0.00576	0.15121 ± 0.00082	0.00216 ± 0.00004	0.12802 ± 0.00104	0.00064 ± 0.00003	86.0	99.9	8.9	5.5	0.0	19.4	75.4	1.7	1354 ± 33
12	728 °C	19.11776 ± 0.00914	0.37922 ± 0.00111	0.00572 ± 0.00007	0.36514 ± 0.00230	0.00126 ± 0.00004	93.4	99.9	16.7	2.3	0.0	48.9	43.4	1.9	1292 ± 17
13	728 °C	8.89516 ± 0.00596	0.17943 ± 0.00052	0.00245 ± 0.00006	0.17584 ± 0.00121	0.00068 ± 0.00004	85.7	99.9	5.0	5.5	0.0	11.7	81.5	1.9	1395 ± 34
14	780 °C	16.77201 ± 0.00845	0.33795 ± 0.00161	0.00570 ± 0.00006	0.40625 ± 0.00303	0.00143 ± 0.00005	92.0	99.9	20.0	2.5	5.1	51.7	40.8	2.4	1363 ± 20
15	780 °C	6.88234 ± 0.00557	0.14225 ± 0.00043	0.00227 ± 0.00004	0.16915 ± 0.00111	0.00058 ± 0.00003	92.5	99.9	21.0	2.4	0.0	53.3	39.0	2.3	1344 ± 22
16	831 °C	9.88459 ± 0.00676	0.20778 ± 0.00077	0.00382 ± 0.00006	0.27065 ± 0.00329	0.00094 ± 0.00004	99.9	99.9	21.1	2.5	6.3	52.5	39.9	2.6	1401 ± 8
17	831 °C	3.49613 ± 0.00324	0.07146 ± 0.00033	0.00134 ± 0.00004	0.09613 ± 0.00069	0.00044 ± 0.00003	99.8	99.9	20.2	4.3	10.3	39.9	54.3	2.6	1427 ± 8
18	882 °C	4.72738 ± 0.00430	0.09883 ± 0.00050	0.00257 ± 0.00004	0.17566 ± 0.00112	0.00077 ± 0.00003	99.7	99.9	19.3	3.9	29.8	41.4	52.6	3.5	1405 ± 8
19	883 °C	2.04634 ± 0.00259	0.04392 ± 0.00025	0.00126 ± 0.00004	0.08345 ± 0.00076	0.00043 ± 0.00003	99.6	99.9	15.8	5.4	36.0	29.8	65.0	3.7	1378 ± 9
20	933 °C	3.24650 ± 0.00354	0.07175 ± 0.00076	0.00256 ± 0.00005	0.19441 ± 0.00112	0.00087 ± 0.00003	99.5	99.8	18.0	4.9	42.7	34.5	59.6	5.3	1350 ± 12
21	933 °C	1.55099 ± 0.00198	0.03335 ± 0.00025	0.00143 ± 0.00003	0.10314 ± 0.00074	0.00054 ± 0.00003	99.3	99.8	17.2	6.1	48.1	29.3	65.7	6.1	1374 ± 10
22	984 °C	2.66170 ± 0.00346	0.06106 ± 0.00033	0.00400 ± 0.00005	0.28552 ± 0.00330	0.00137 ± 0.00003	99.0	99.7	16.9	5.2	59.2	32.2	62.3	9.2	1311 ± 8
23	984 °C	1.16674 ± 0.00168	0.02581 ± 0.00021	0.00176 ± 0.00004	0.13857 ± 0.00102	0.00073 ± 0.00003	98.7	99.6	18.7	6.7	56.7	29.1	65.9	10.6	1343 ± 11
24	1034 °C	1.87861 ± 0.00238	0.04683 ± 0.00039	0.00414 ± 0.00007	0.50168 ± 0.00483	0.00199 ± 0.00004	98.1	99.3	28.8	6.4	50.9	38.8	54.6	21.2	1232 ± 10
25	1034 °C	0.64362 ± 0.00173	0.01639 ± 0.00022	0.00161 ± 0.00004	0.22416 ± 0.00122	0.00090 ± 0.00003	97.5	99.0	33.1	7.5	46.7	38.3	55.1	27.1	1209 ± 15
26	1084 °C	2.51253 ± 0.00369	0.06403 ± 0.00043	0.00681 ± 0.00006	1.65507 ± 0.01652	0.00448 ± 0.00005	98.1	98.2	57.7	5.4	25.2	56.8	33.4	51.6	1221 ± 9
27	1083 °C	0.73961 ± 0.00176	0.01568 ± 0.00022	0.00201 ± 0.00005	0.51021 ± 0.00356	0.00158 ± 0.00004	97.2	97.7	60.4	8.0	21.8	49.7	41.7	65.3	1387 ± 17
28	CO2	0.00260 ± 0.00054	0.00003 ± 0.00003	0.00003 ± 0.00002	0.00856 ± 0.00047	0.00004 ± 0.00002	68.7	76.6	76.0	22.5	0.0	32.9	61.6	863.1	2136 ± 2010
29	CO2	0.01670 ± 0.00056	0.00053 ± 0.00004	0.00016 ± 0.00002	0.05680 ± 0.00078	0.00012 ± 0.00002	98.5	92.5	94.3	1.2	0.0	80.9	6.5	227.0	1091 ± 84
30	CO2	0.00511 ± 0.00054	0.00022 ± 0.00004	0.00019 ± 0.00002	0.05818 ± 0.00076	0.00016 ± 0.00002	79.6	81.4	94.1	4.2	0.0	70.6	19.9	644.0	811 ± 207
31	CO2	0.00818 ± 0.00058	0.00034 ± 0.00004	0.00033 ± 0.00002	0.11854 ± 0.00131	0.00030 ± 0.00002	71.2	75.8	92.9	5.4	0.0	65.6	24.1	898.4	798 ± 163
32	CO2	0.00770 ± 0.00055	0.00028 ± 0.00004	0.00028 ± 0.00002	0.11890 ± 0.00153	0.00025 ± 0.00002	83.9	70.4	95.0	3.3	0.0	71.4	15.8	1186.7	1073 ± 207
33	CO2	0.03211 ± 0.00066	0.00208 ± 0.00004	0.00233 ± 0.00004	0.98105 ± 0.00887	0.00186 ± 0.00003	86.7	67.2	97.0	1.4	0.0	78.8	7.2	1375.9	722 ± 45
34	CO2	1.31167 ± 0.00157	0.08406 ± 0.00027	0.12444 ± 0.00034	50.63871 ± 0.14683	0.09297 ± 0.00018	100.0	58.1	98.7	0.0	0.0	85.6	0.0	2031.3	917 ± 9
35	CO2	0.21997 ± 0.00066	0.01512 ± 0.00007	0.02971 ± 0.00017	10.91895 ± 0.06097	0.02233 ± 0.00008	93.2	49.8	98.6	0.4	0.0	85.0	2.1	2843.1	928 ± 27
36	CO2	0.07910 ± 0.00072	0.00217 ± 0.00007	0.00376 ± 0.00004	0.97859 ± 0.00998	0.00280 ± 0.00004	93.8	68.7	98.0	1.0	0.0	85.3	5.5	1283.3	1443 ± 56

NAK-3

olivine concentrate															
1	464 °C	0.00485 ± 0.00161	0.00008 ± 0.00004	0.00003 ± 0.00002	0.00000 ± 0.00056	0.00000 ± 0.00002	---	---	---	---	---	---	---	---	---
2	464 °C	0.01690 ± 0.00157	0.00005 ± 0.00003	0.00003 ± 0.00002	0.00023 ± 0.00057	0.00005 ± 0.00002	---	---	---	---	---	---	---	---	---
3	518 °C	0.01639 ± 0.00151	0.00020 ± 0.00004	0.00004 ± 0.00002	0.00107 ± 0.00059	0.00007 ± 0.00002	---	---	---	---	---	---	---	---	---
4	518 °C	0.00974 ± 0.00150	0.00012 ± 0.00004	0.00001 ± 0.00002	0.00073 ± 0.00056	0.00002 ± 0.00002	---	---	---	---	---	---	---	---	---
5	571 °C	0.03354 ± 0.00151	0.00034 ± 0.00005	0.00005 ± 0.00002	0.00067 ± 0.00055	0.00007 ± 0.00002	---	---	---	---	---	---	---	---	---

NAK-4

2	410 °C	0.00000 ± 0.00115	0.00006 ± 0.00006	0.00000 ± 0.00002	0.00000 ± 0.00065	0.00000 ± 0.00002	---	---	---	---	---	---	---	---	---	---	±	---
2	464 °C	0.01573 ± 0.00108	0.00008 ± 0.00005	0.00000 ± 0.00002	0.00045 ± 0.00066	0.00003 ± 0.00002	---	---	---	---	---	---	---	---	---	---	±	---
3	464 °C	0.00209 ± 0.00114	0.00008 ± 0.00005	0.00004 ± 0.00002	0.00086 ± 0.00067	0.00001 ± 0.00002	---	---	---	---	---	---	---	---	---	---	±	---
4	517 °C	0.02445 ± 0.00117	0.00040 ± 0.00005	0.00003 ± 0.00002	0.00162 ± 0.00063	0.00004 ± 0.00002	---	---	---	---	---	---	---	---	---	---	±	---
5	517 °C	0.01059 ± 0.00112	0.00021 ± 0.00005	0.00001 ± 0.00002	0.00000 ± 0.00065	0.00001 ± 0.00002	---	---	---	---	---	---	---	---	---	---	±	---
6	570 °C	0.03645 ± 0.00107	0.00054 ± 0.00005	0.00003 ± 0.00002	0.00031 ± 0.00064	0.00004 ± 0.00002	---	---	---	---	---	---	---	---	---	---	±	---
7	570 °C	0.01810 ± 0.00106	0.00038 ± 0.00006	0.00002 ± 0.00002	0.00000 ± 0.00068	0.00004 ± 0.00002	---	---	---	---	---	---	---	---	---	---	±	---
8	623 °C	0.04945 ± 0.00106	0.00083 ± 0.00006	0.00003 ± 0.00002	0.00108 ± 0.00064	0.00007 ± 0.00002	---	---	---	---	---	---	---	---	---	---	±	---
9	624 °C	0.02398 ± 0.00108	0.00039 ± 0.00006	0.00002 ± 0.00002	0.00036 ± 0.00066	0.00002 ± 0.00002	---	---	---	---	---	---	---	---	---	---	±	---
10	676 °C	0.06329 ± 0.00111	0.00115 ± 0.00007	0.00002 ± 0.00002	0.00139 ± 0.00067	0.00004 ± 0.00002	---	---	---	---	---	---	---	---	---	---	±	---
11	676 °C	0.03032 ± 0.00107	0.00050 ± 0.00007	0.00002 ± 0.00002	0.00042 ± 0.00068	0.00002 ± 0.00002	---	---	---	---	---	---	---	---	---	---	±	---
12	728 °C	0.05749 ± 0.00110	0.00100 ± 0.00007	0.00000 ± 0.00002	0.00023 ± 0.00071	0.00001 ± 0.00002	---	---	---	---	---	---	---	---	---	---	±	---
13	728 °C	0.02445 ± 0.00114	0.00043 ± 0.00006	0.00000 ± 0.00002	0.00000 ± 0.00070	0.00001 ± 0.00002	---	---	---	---	---	---	---	---	---	---	±	---
14	780 °C	0.03365 ± 0.00102	0.00067 ± 0.00004	0.00002 ± 0.00002	0.00107 ± 0.00037	0.00003 ± 0.00002	---	---	---	---	---	---	---	---	---	---	±	---
15	780 °C	0.01319 ± 0.00096	0.00013 ± 0.00003	0.00000 ± 0.00002	0.00093 ± 0.00035	0.00003 ± 0.00002	---	---	---	---	---	---	---	---	---	---	±	---
16	831 °C	0.01501 ± 0.00092	0.00021 ± 0.00003	0.00001 ± 0.00002	0.00087 ± 0.00034	0.00000 ± 0.00002	---	---	---	---	---	---	---	---	---	---	±	---
17	831 °C	0.00563 ± 0.00090	0.00011 ± 0.00003	0.00000 ± 0.00002	0.00076 ± 0.00035	0.00006 ± 0.00002	---	---	---	---	---	---	---	---	---	---	±	---
18	882 °C	0.01190 ± 0.00091	0.00006 ± 0.00003	0.00002 ± 0.00002	0.00150 ± 0.00043	0.00003 ± 0.00002	---	---	---	---	---	---	---	---	---	---	±	---
19	882 °C	0.00680 ± 0.00090	0.00006 ± 0.00003	0.00000 ± 0.00002	0.00000 ± 0.00032	0.00003 ± 0.00002	---	---	---	---	---	---	---	---	---	---	±	---
20	933 °C	0.01484 ± 0.00091	0.00021 ± 0.00003	0.00002 ± 0.00002	0.00210 ± 0.00032	0.00005 ± 0.00002	3.5	99.3	22.6	56.3	8.6	5.9	93.0	19.3	105 ± 1400			
21	933 °C	0.00736 ± 0.00089	0.00008 ± 0.00003	0.00002 ± 0.00002	0.00089 ± 0.00034	0.00002 ± 0.00002	37.5	99.2	11.7	21.9	60.6	7.6	91.0	21.6	1100 ± 2192			
22	984 °C	0.02646 ± 0.00093	0.00021 ± 0.00003	0.00003 ± 0.00002	0.00439 ± 0.00037	0.00009 ± 0.00002	7.3	98.5	29.4	60.1	2.8	7.1	91.6	42.0	376 ± 1316			
23	984 °C	0.00538 ± 0.00090	0.00006 ± 0.00003	0.00002 ± 0.00002	0.00204 ± 0.00036	0.00001 ± 0.00002	72.0	97.7	26.9	5.8	63.7	39.7	54.5	67.4	1734 ± 1834			
24	1034 °C	0.01672 ± 0.00088	0.00037 ± 0.00003	0.00006 ± 0.00002	0.01485 ± 0.00055	0.00009 ± 0.00002	2.1	97.2	68.4	22.1	1.7	31.3	64.1	80.2	42 ± 776			
25	1034 °C	0.00556 ± 0.00090	0.00014 ± 0.00003	0.00000 ± 0.00002	0.00525 ± 0.00044	0.00003 ± 0.00002	---	---	---	---	---	---	---	---	---	---	±	---
26	1084 °C	0.01646 ± 0.00091	0.00041 ± 0.00003	0.00013 ± 0.00002	0.04663 ± 0.00081	0.00011 ± 0.00002	96.3	92.2	92.4	3.5	0.0	71.8	17.1	240.0	1275 ± 104			
27	1084 °C	0.00677 ± 0.00088	0.00011 ± 0.00003	0.00003 ± 0.00002	0.01308 ± 0.00055	0.00004 ± 0.00002	92.7	91.8	82.5	12.5	0.0	45.9	44.2	250.5	1664 ± 360			
28	1134 °C	0.00865 ± 0.00088	0.00047 ± 0.00004	0.00052 ± 0.00002	0.20937 ± 0.00173	0.00040 ± 0.00002	94.7	68.8	97.8	0.7	0.0	82.5	3.6	1277.7	881 ± 139			
29	1134 °C	0.00621 ± 0.00089	0.00021 ± 0.00003	0.00012 ± 0.00002	0.05767 ± 0.00085	0.00014 ± 0.00002	68.6	80.6	85.4	12.1	0.0	47.2	42.2	679.6	884 ± 238			
30	1184 °C	0.01731 ± 0.00088	0.00276 ± 0.00005	0.00705 ± 0.00005	3.08121 ± 0.02538	0.00529 ± 0.00004	100.0	22.4	99.2	0.0	0.0	85.7	0.0	9787.0	949 ± 84			
31	1184 °C	0.00728 ± 0.00091	0.00017 ± 0.00004	0.00177 ± 0.00003	0.74620 ± 0.01311	0.00136 ± 0.00003	87.6	26.9	98.7	0.4	0.0	83.4	2.1	7665.6	1085 ± 276			
32	1233 °C	0.01906 ± 0.00089	0.00480 ± 0.00007	0.01372 ± 0.00007	5.98742 ± 0.05801	0.01065 ± 0.00005	48.7	13.3	98.5	0.5	0.0	82.2	2.9	18378.3	515 ± 216			
33	1233 °C	0.00714 ± 0.00089	0.00011 ± 0.00005	0.00280 ± 0.00004	1.24633 ± 0.01783	0.00216 ± 0.00003	83.2	14.1	98.7	0.3	0.0	83.0	1.7	17203.1	1280 ± 430			
34	1282 °C	0.01030 ± 0.00089	0.00024 ± 0.00006	0.00559 ± 0.00006	2.38080 ± 0.02797	0.00040 ± 0.00004	69.1	19.0	98.6	0.4	0.0	83.0	2.3	11991.2	672 ± 224			
35	1282 °C	0.00786 ± 0.00090	0.00038 ± 0.00003	0.00041 ± 0.00002	0.16501 ± 0.00253	0.00032 ± 0.00002	93.5	69.6	97.5	1.0	0.0	81.2	5.0	1231.1	948 ± 165			
36	1331 °C	0.00965 ± 0.00091	0.00032 ± 0.00003	0.00011 ± 0.00002	0.04243 ± 0.00083	0.00011 ± 0.00002	88.3	90.9	84.6	7.6	3.9	57.1	3.2	282.3	972 ± 139			
37	1332 °C	0.00823 ± 0.00095	0.00027 ± 0.00003	0.00004 ± 0.00002	0.06222 ± 0.00040	0.00007 ± 0.00002	80.4	98.4	57.8	33.1	0.0	21.1	76.4	45.8	863 ± 156			

NAK-5

2	410 °C	4.23586 ± 0.00323	0.11540 ± 0.00030	0.00220 ± 0.00003	0.14832 ± 0.00135	0.00075 ± 0.00004	69.9	99.9	10.7	6.2	19.1	20.4	74.4	2.5	1231 ± 78
2	410 °C	3.36797 ± 0.00341	0.09394 ± 0.00023	0.00168 ± 0.00003	0.10697 ± 0.00140	0.00050 ± 0.00003	75.6	99.9	10.4	5.2	16.3	22.6	71.6	2.3	1281 ± 63
3	464 °C	18.21425 ± 0.00715	0.52187 ± 0.00093	0.00895 ± 0.00008	0.58030 ± 0.00450	0.00192 ± 0.00007	85.3	99.9	10.3	3.2	15.3	31.2	60.8	2.2	1369 ± 34
4	464 °C	9.49100 ± 0.00478	0.28448 ± 0.00060	0.00478 ± 0.00004	0.29994 ± 0.00341	0.00093 ± 0.00005	87.0	99.9	10.0	2.8	14.6	33.3	58.1	2.1	1344 ± 30
5	517 °C	35.09782 ± 0.01502	1.07579 ± 0.00131	0.01779 ± 0.00006	1.10778 ± 0.00481	0.00283 ± 0.00008	90.9	99.9	9.9	1.9	14.3	40.4	49.2	2.0	1365 ± 20
6	517 °C	17.61711 ± 0.00478	0.55166 ± 0.00076	0.00895 ± 0.00005	0.53275 ± 0.00393	0.00147 ± 0.00006	89.9	99.9	9.5	2.1	13.1	37.3	53.1	1.9	1334 ± 22
7	570 °C	56.03170 ± 0.02205	1.81837 ± 0.00171	0.02916 ± 0.00009	1.80079 ± 0.01005	0.00458 ± 0.00010	90.8	99.9	8.8	1.9	12.1	40.5	49.1	1.9	1310 ± 19
8	570 °C	25.28665 ± 0.00981	0.83071 ± 0.00111	0.01319 ± 0.00011	0.79971 ± 0.00943	0.00219 ± 0.00008	89.6	99.9	9.6	2.1	11.3	37.6	52.7	1.9	1286 ± 23
9	623 °C	54.23756 ± 0.01905	1.81024 ± 0.00211	0.02895 ± 0.00014	1.71269 ± 0.00811	0.00528 ± 0.00010	87.1	99.9	9.4	2.6	11.6	33.4	58.0	1.9	1246 ± 26
10	624 °C	18.31642 ± 0.00734	0.61102 ± 0.00092	0.01024 ± 0.00005	0.54058 ± 0.00368	0.00201 ± 0.00007	99.8	99.9	8.4	3.1	15.6	27.7	65.1	1.7	1373 ± 5
11	676 °C	27.49829 ± 0.00980	0.92393 ± 0.00098	0.01728 ± 0.00007	0.88780 ± 0.00490	0.00404 ± 0.00007	99.7	99.9	8.2	4.1	22.5	22.6	71.5	1.9	1365 ± 5
12	676 °C	9.66760 ± 0.00510	0.31211 ± 0.00063	0.00643 ± 0.00007	0.30234 ± 0.00230	0.00151 ± 0.00006	99.6	99.9	7.5	4.3	27.3	20.6	74.1	1.8	1376 ± 6
13	728 °C	15.85257 ± 0.00763	0.57312 ± 0.00075	0.01210 ± 0.00005	0.63231 ± 0.00354	0.00247 ± 0.00006	99.7	99.9	8.3	3.3	24.1	26.4	66.8	2.3	1357 ± 5
14	728 °C	7.44894 ± 0.00463	0.25165 ± 0.00060	0.00583 ± 0.00007	0.27693 ± 0.00220	0.00117 ± 0.00005	99.7	99.9	7.6	3.4	36.3	24.5	69.3	2.2	1360 ± 6
15	780 °C	8.00154 ± 0.00491	0.27310 ± 0.00065	0.00698 ± 0.00004	0.37046 ± 0.00410	0.00131 ± 0.00005	99.7	99.9	8.4	2.9	40.8	29.2	63.3	2.7	1350 ± 6
16	780 °C	5.04868 ± 0.00434	0.17252 ± 0.00031	0.00444 ± 0.00005	0.22808 ± 0.00202	0.00088 ± 0.00005	99.6	99.9	8.2	3.2	41.1	26.6	66.6	2.6	1349 ± 6
17	831 °C	5.98891 ± 0.00369	0.26781 ± 0.00043	0.00616 ± 0.00005	0.32925 ± 0.00315	0.00097 ± 0.00005	99.7	99.9	8.5	2.1	48.1	35.1	55.8	3.1	1335 ± 5
18	831 °C	3.96560 ± 0.00378	0.13649 ± 0.00032	0.00397 ± 0.00004	0.21069 ± 0.00181	0.00069 ± 0.00005	99.7	99.9	8.4	2.5	47.0	31.6	60.2	3.0	1343 ± 6
19	882 °C	4.72083 ± 0.00305	0.16657 ± 0.00028	0.00573 ± 0.00004	0.30820 ± 0.00168	0.00104 ± 0.00003	99.6	99.9	8.6	2.7	53.2	30.6	61.5	3.6	1318 ± 5
20	882 °C	3.23299 ± 0.00246	0.11364 ± 0.00028	0.00361 ± 0.00004	0.20451 ± 0.00204	0.00053 ± 0.00004	99.7	99.9	8.0	1.9	51.6	35.5	54.3	3.5	1323 ± 6
21	933 °C	4.25691 ± 0.00305	0.15170 ± 0.00029	0.00647 ± 0.00008	0.33145 ± 0.00271	0.00107 ± 0.00003	99.5	99.9	8.2	2.5	61.5	28.4	63.3	4.3	1309 ± 5
22	933 °C	2.93789 ± 0.00297	0.10489 ± 0.00027	0.00376 ± 0.00004	0.21491 ± 0.00142	0.00076 ± 0.00003	99.4	99.9	8.1	3.3	54.5	26.0	66.5	4.0	1307 ± 6
23	984 °C	7.12668 ± 0.00453	0.26759 ± 0.00059	0.01128 ± 0.00010	0.83982 ± 0.00763	0.00210 ± 0.00006	99.5	99.8	10.5	2.4	58.0	36.6	52.8	6.2	1261 ± 5
24	984 °C	3.20209 ± 0.00314	0.11599 ± 0.00025	0.00378 ± 0.00004	0.31290 ± 0.00276	0.00081 ± 0.00004	99.6	99.8	13.2	2.6	46.6	40.0	49.8	5.3	1295 ± 6
25	1034 °C	5.13332 ± 0.00406	0.20256 ± 0.00038	0.01095 ± 0.00008	2.52059 ± 0.01068	0.00411 ± 0.00008	---	99.1	36.6	---	38.7	---	---	24.6	1222 ± 5
26	1034 °C	2.80133 ± 0.00332	0.10073 ± 0.00027	0.00443 ± 0.00004	0.92505 ± 0.00439	0.00177 ± 0.00003	---	99.4	33.2	---	35.6	53.8	---	18.1	1304 ± 6
27	1084 °C	19.46527 ± 0.00842	0.71736 ± 0.00097	0.05277 ± 0.00016	18.90203 ± 0.04878	0.02777 ± 0.00008	---	98.2	50.6	---	29.9	---	---	52.6	1298 ± 5
28	1084 °C	2.59490 ± 0.00296	0.09961 ± 0.00026	0.01288 ± 0.00010	6.00197 ± 0.03825	0.00818 ± 0.00004	---	95.8	65.9	---	22.1	67.2	---	123.3	1283 ± 6
29	1134 °C	0.98616 ± 0.00193	0.04994 ± 0.00023	0.02928 ± 0.00014	19.08094 ± 0.24001	0.02332 ± 0.00007	---	73.4	92.1	---	4.4	74.9	---	1019.6	1256 ± 10
30	1134 °C	0.08878 ± 0.00146	0.00616 ± 0.00011	0.00667 ± 0.00007	4.28688 ± 0.03060	0.00553 ± 0.00008	83.1	51.8	90.9	1.7	5.5	71.0	8.5	2628.9	1138 ± 70
31	1184 °C	0.27652 ± 0.00159	0.03708 ± 0.00018	0.05311 ± 0.00020	36.86947 ± 0.12924	0.04584 ± 0.00021	69.3	30.9	97.2	1.2	0.0	72.9	5.8	6307.7	890 ± 97
32	1184 °C	0.05558 ± 0.00145	0.00669 ± 0.00010	0.03953 ± 0.00006	6.86878 ± 0.09059	0.00801 ± 0.00006	91.4	28.6	98.0	0.4	0.0	75.4	1.9	7037.9	1261 ± 88
33	1233 °C	0.04414 ± 0.00145	0.00700 ± 0.00009	0.01064 ± 0.00007	7.59566 ± 0.04579	0.00929 ± 0.00008	56.8	24.6	97.0	1.4	0.0	71.9	6.4	8642.4	796 ± 175
34	1233 °C	0.01289 ± 0.00147	0.00040 ± 0.00006	0.00018 ± 0.00002	0.11028 ± 0.00204	0.00019 ± 0.00003	85.9	80.7	86.7	7.7	2.2	54.0	30.4	673.9	1515 ± 263
35	1282 °C	0.02150 ± 0.00147	0.00070 ± 0.00007	0.00040 ± 0.00002	0.29129 ± 0.00562	0.00041 ± 0.00003	88.3	71.0	90.9	6.1	0.0	75.9	24.4	1155.4	1566 ± 318
36	1282 °C	0.01596 ± 0.00146	0.00041 ± 0.00006	0.00044 ± 0.00003	0.26781 ± 0.00538	0.00035 ± 0.00003	99.2	54.9	97.9	0.3	0.0	58.6	1.4	2315.7	2268 ± 1343
37	1331 °C	0.01458 ± 0.00147	0.00034 ± 0.00007	0.00033 ± 0.00002	0.24205 ± 0.00342	0.00037 ± 0.00003	80.4	50.6	89.6	8.4	0.0	52.0	30.7	2757.1	2325 ± 795
38	1332 °C	0.01129 ± 0.00149	0.00018 ± 0.00006	0.00008 ± 0.00002	0.03376 ± 0.00126	0.00005 ± 0.00003	---	---	---	---	---	---	---	---	2365 ± 942

MIL-1

1	410 °C	0.00710 ± 0.00062	0.00015 ± 0.00004	0.00004 ± 0.00001	0.00014 ± 0.00029	0.00002 ± 0.00002	---	---	---	---	---	---	---	---	---	---	---
2	410 °C	0.00878 ± 0.00057	0.00015 ± 0.00005	0.00000 ± 0.00001	0.00027 ± 0.00032	0.00000 ± 0.00002	---	---	---	---	---	---	---	---	---	---	± ---
3	464 °C	0.11843 ± 0.00075	0.00210 ± 0.00007	0.00005 ± 0.00002	0.00447 ± 0.00032	0.00005 ± 0.00002	55.7	99.9	22.6	17.0	11.8	16.9	80.5	4.2	1038 ± 336		
4	464 °C	0.12457 ± 0.00117	0.00205 ± 0.00008	0.00005 ± 0.00001	0.00267 ± 0.00032	0.00003 ± 0.00002	69.3	99.9	13.9	12.8	24.3	14.3	83.5	2.6	1288 ± 311		
5	518 °C	1.02081 ± 0.00154	0.01732 ± 0.00010	0.00034 ± 0.00002	0.04383 ± 0.00060	0.00024 ± 0.00002	75.6	99.8	24.6	12.7	0.0	22.4	72.8	5.0	1339 ± 63		
6	517 °C	0.69386 ± 0.00144	0.01233 ± 0.00011	0.00029 ± 0.00002	0.03091 ± 0.00055	0.00015 ± 0.00002	82.6	99.8	28.9	7.2	11.1	36.6	57.8	4.9	1381 ± 56		
7	571 °C	2.66106 ± 0.00292	0.04976 ± 0.00024	0.00093 ± 0.00002	0.09673 ± 0.00076	0.00040 ± 0.00002	89.0	99.9	26.2	5.1	7.0	42.0	51.6	3.8	1403 ± 27		
8	571 °C	1.42543 ± 0.00164	0.02790 ± 0.00020	0.00051 ± 0.00002	0.03268 ± 0.00053	0.00018 ± 0.00002	88.1	99.9	17.1	5.7	10.2	30.7	64.6	2.3	1349 ± 32		
9	623 °C	4.32095 ± 0.00372	0.08606 ± 0.00033	0.00144 ± 0.00002	0.10078 ± 0.00087	0.00043 ± 0.00002	92.5	99.9	18.6	3.8	4.8	40.8	53.0	2.3	1381 ± 18		
10	623 °C	2.13618 ± 0.00282	0.04279 ± 0.00023	0.00076 ± 0.00002	0.04843 ± 0.00056	0.00024 ± 0.00002	90.4	99.9	17.0	4.6	9.9	34.8	59.8	2.2	1351 ± 24		
11	676 °C	4.91241 ± 0.00372	0.09408 ± 0.00016	0.00181 ± 0.00003	0.10463 ± 0.00084	0.00142 ± 0.00003	93.3	99.9	15.5	16.3	4.7	12.8	85.3	2.2	1488 ± 8		
12	676 °C	1.60525 ± 0.00193	0.03238 ± 0.00023	0.00061 ± 0.00002	0.03320 ± 0.00054	0.00021 ± 0.00002	99.7	99.9	14.5	5.8	15.2	27.1	68.7	2.0	1440 ± 10		
13	728 °C	2.46693 ± 0.00302	0.05042 ± 0.00025	0.00092 ± 0.00002	0.05526 ± 0.00082	0.00030 ± 0.00002	99.8	99.9	16.1	5.0	11.9	31.8	63.3	2.1	1427 ± 9		

14	728 °C	0.95801 ± 0.00135	0.01964 ± 0.00011	0.00041 ± 0.00002	0.02218 ± 0.00047	0.00019 ± 0.00002	99.6	99.9	14.4	8.9	18.4	19.8	77.2	2.2	1422 ± 9
15	780 °C	1.54999 ± 0.00164	0.03168 ± 0.00015	0.00078 ± 0.00002	0.04205 ± 0.00052	0.00025 ± 0.00002	99.7	99.9	14.4	5.2	30.9	29.1	66.4	2.6	1427 ± 8
16	780 °C	0.72030 ± 0.00115	0.01464 ± 0.00012	0.00042 ± 0.00002	0.02033 ± 0.00050	0.00012 ± 0.00002	99.7	99.9	12.8	4.4	40.7	30.2	65.1	2.7	1432 ± 11
17	831 °C	1.29311 ± 0.00183	0.02617 ± 0.00016	0.00092 ± 0.00002	0.04490 ± 0.00061	0.00025 ± 0.00002	99.7	99.9	13.0	4.2	48.0	31.2	64.0	3.4	1436 ± 9
18	831 °C	0.62944 ± 0.00115	0.01262 ± 0.00011	0.00042 ± 0.00002	0.01873 ± 0.00041	0.00018 ± 0.00002	99.4	99.9	12.0	8.2	43.0	18.2	79.0	2.9	1443 ± 11
19	883 °C	1.26884 ± 0.00144	0.02535 ± 0.00016	0.00142 ± 0.00002	0.06123 ± 0.00073	0.00035 ± 0.00002	99.5	99.8	11.5	4.0	62.7	29.9	65.5	4.7	1448 ± 10
20	882 °C	0.46702 ± 0.00095	0.01011 ± 0.00010	0.00038 ± 0.00001	0.03332 ± 0.00059	0.00015 ± 0.00002	99.4	99.8	18.6	6.1	43.0	30.7	63.4	6.5	1370 ± 12
21	933 °C	0.93417 ± 0.00164	0.01940 ± 0.00018	0.00084 ± 0.00002	0.08178 ± 0.00075	0.00029 ± 0.00002	99.5	99.7	20.7	4.5	46.6	39.1	53.4	8.3	1411 ± 12
22	933 °C	0.35835 ± 0.00097	0.00708 ± 0.00009	0.00033 ± 0.00002	0.03620 ± 0.00056	0.00015 ± 0.00002	99.3	99.6	23.2	6.8	44.1	32.8	60.9	10.1	1459 ± 15
23	984 °C	0.33807 ± 0.00094	0.00833 ± 0.00010	0.00086 ± 0.00002	0.20705 ± 0.00109	0.00046 ± 0.00002	99.0	98.3	51.3	3.4	33.3	62.3	25.8	49.6	1259 ± 14
24	984 °C	0.10028 ± 0.00066	0.00201 ± 0.00007	0.00021 ± 0.00002	0.05666 ± 0.00075	0.00010 ± 0.00002	99.8	98.0	58.0	0.9	29.1	77.8	7.3	56.3	1465 ± 38
25	1034 °C	0.92671 ± 0.00155	0.02152 ± 0.00017	0.00364 ± 0.00003	1.32651 ± 0.00798	0.00264 ± 0.00004	98.6	95.7	77.8	3.0	11.5	69.7	17.0	126.2	1334 ± 11
26	1034 °C	0.04710 ± 0.00059	0.00086 ± 0.00005	0.00021 ± 0.00001	0.07722 ± 0.00090	0.00018 ± 0.00002	96.7	93.7	80.5	6.6	7.3	58.5	30.4	188.2	1577 ± 75
27	CO2	0.01449 ± 0.00035	0.00135 ± 0.00007	0.00333 ± 0.00003	1.57327 ± 0.01206	0.00271 ± 0.00004	64.0	19.1	97.6	1.4	0.0	77.7	6.9	11929.9	1144 ± 300
28	CO2	0.00295 ± 0.00031	0.00022 ± 0.00005	0.00047 ± 0.00001	0.20548 ± 0.00224	0.00035 ± 0.00002	85.6	34.1	92.5	0.8	5.7	80.3	4.3	5443.0	1102 ± 570
29	CO2	0.00959 ± 0.00038	0.00052 ± 0.00005	0.00114 ± 0.00002	0.51989 ± 0.01016	0.00093 ± 0.00002	79.7	30.9	97.1	1.5	0.3	77.6	7.5	6306.4	1395 ± 354
30	CO2	0.19571 ± 0.00055	0.00619 ± 0.00022	0.01345 ± 0.00006	6.30487 ± 0.04117	0.01086 ± 0.00006	90.2	29.2	97.7	1.2	0.0	78.3	6.3	6846.2	2214 ± 169
31	CO2	0.00882 ± 0.00032	0.00090 ± 0.00006	0.00229 ± 0.00003	1.02613 ± 0.01126	0.00184 ± 0.00002	53.8	20.7	95.6	1.5	1.9	77.3	7.9	10793.1	880 ± 314
32	CO2	0.07273 ± 0.00031	0.00763 ± 0.00006	0.01978 ± 0.00008	9.44827 ± 0.07968	0.01568 ± 0.00008	77.4	13.9	98.3	0.7	0.0	80.3	3.7	17434.9	1509 ± 154
33	CO2	0.00864 ± 0.00032	0.00063 ± 0.00005	0.00163 ± 0.00002	0.68742 ± 0.00715	0.00122 ± 0.00002	73.2	24.5	90.1	1.2	7.7	78.2	6.8	8690.1	1257 ± 342
34	CO2	0.02147 ± 0.00045	0.00003 ± 0.00004	0.00004 ± 0.00001	0.02067 ± 0.00061	0.00004 ± 0.00002	98.1	45.4	89.7	9.0	0.0	53.5	33.8	3396.3	6845 ± 6512
35	CO2	0.07195 ± 0.00042	0.00155 ± 0.00006	0.00387 ± 0.00003	1.80567 ± 0.01925	0.00317 ± 0.00004	90.3	19.0	97.4	1.6	0.0	77.0	7.9	12047.6	3364 ± 318

Isotope abundances given in nanoamps (spectrometer sensitivity is 1.4×10^{-10} mols/nA),

and corrected for ^{37}Ar and ^{39}Ar decay, half lives of 35.2 days and 269 years, respectively.

Isotope sources calculated using the reactor constants in Renne et al. (1998),

assuming $(^{39}\text{Ar}/^{39}\text{Ar})_{\text{cos}} = 1.54$ and $(^{39}\text{Ar}/^{39}\text{Ar})_{\text{lim}} = 0.244$,

and the following trapped $^{40}\text{Ar}/^{39}\text{Ar}$: [ALH: OPX/CPX = 5 ± 5 ; Mask. = 632 ± 90], [Nakhla: CPX/OPX = 32 ± 9 ; Olivine = 213 ± 120 ; Plag. = 2287 ± 430], [MIL: CPX = 28 ± 8 ; Mesostasis Glass = 1425 ± 230].

Ages calculated using the decay constants and standard calibration of Renne et al. (2010) and isotope abundances of Steiger and Jäger (1977)

and calculated relative to Hb3gr fluence monitor (1080.4 Ma).

Average analytical blanks are: $^{40}\text{Ar} = 0.015$; $^{39}\text{Ar} = 0.0001$; $^{38}\text{Ar} = 0.00002$; $^{37}\text{Ar} = 0.0001$; $^{36}\text{Ar} = 0.00007$.

Temperature was controlled with approximately $\pm 5^\circ\text{C}$ precision and $\pm 10^\circ\text{C}$ accuracy.

--- Data marked with dashes are indeterminate or negligibly above the detection limit.